Nucleon isovector axial form factors

Yong-Chull Jang,[1,2,3,*] Rajan Gupta,[4,†] Tanmoy Bhattacharya,[4,‡] Boram Yoon,[5,§] and Huey-Wen Lin[6,‖]

(Precision Neutron Decay Matrix Elements (PNDME) Collaboration)

[1]*Electron-Ion Collider, Brookhaven National Laboratory, Upton, New York 11973, USA*
[2]*Physics Department, Brookhaven National Laboratory, Upton, New York 11973, USA*
[3]*Department of Physics, Columbia University, 538 West 120th Street, New York, New York 10027, USA*
[4]*Los Alamos National Laboratory, Theoretical Division T-2, Los Alamos, New Mexico 87545, USA*
[5]*NVIDIA Corporation, Santa Clara, California 95051, USA*
[6]*Department of Physics and Astronomy, Michigan State University, East Lansing, Michigan 48824, USA*

(Received 29 June 2023; accepted 5 December 2023; published 5 January 2024)

We present results for the isovector axial vector form factors obtained using thirteen $2+1+1$-flavor highly improved staggered quark (HISQ) ensembles generated by the MILC collaboration. The calculation of nucleon two- and three-point correlation functions has been done using Wilson-clover fermions. In the analysis of these data, we quantify the sensitivity of the results to strategies used for removing excited state contamination and invoke the partially conserved axial current relation between the form factors to choose between them. Our data driven analysis includes removing contributions from multihadron $N\pi$ states that make significant contributions. Our final results are $g_A = 1.292(53)_{\text{stat}}(24)_{\text{sys}}$ for the axial charge; $g_S = 1.085(50)_{\text{stat}}(103)_{\text{sys}}$ and $g_T = 0.991(21)_{\text{stat}}(10)_{\text{sys}}$ for the scalar and tensor charges; $\langle r_A^2 \rangle = 0.439(56)_{\text{stat}}(34)_{\text{sys}}$ fm^2 for the mean squared axial charge radius, $g_P^* = 9.03(47)_{\text{stat}}(42)_{\text{sys}}$ for the induced pseudoscalar charge; and $g_{\pi NN} = 14.14(81)_{\text{stat}}(85)_{\text{sys}}$ for the pion-nucleon coupling. We also provide a parametrization of the axial form factor $G_A(Q^2)$ over the range $0 \le Q^2 \le 1$ GeV^2 for use in phenomenology and a comparison with other lattice determinations. We find that the various lattice data agree within 10% but are significantly different from the extraction of $G_A(Q^2)$ from the ν-deuterium scattering data.

DOI: 10.1103/PhysRevD.109.014503

I. INTRODUCTION

In ongoing neutrino scattering experiments (T2K, NOvA, MINERνA, MicroBooNE, SBN), the lack of precise reconstruction of the final state of the struck nucleus gives rise to uncertainty in the cross section. Theoretical calculations of the cross section for targets, such as ^{12}C, ^{16}O, and ^{40}Ar, being used in experiments take as input axial-vector form factor of the nucleon and build in nuclear effects using nuclear many body theory [1–3]. Both of these steps, calculating nucleon axial form factors using lattice QCD and including nuclear effects using many-body theory, have uncertainties. Incorporating nuclear effects involves modeling of the complex physical phenomena (quasi-elastic, resonance, deep inelastic scattering) that contribute when considering incoming neutrino energies up to 5 GeV relevant for ongoing and future (DUNE) experiments. These complex phenomena make it hard to reconstruct the incident neutrino energy or the cross-section from the imprecise knowledge of the final state of the struck nucleus. On the other hand, the cleanest experimental measurements of the nucleon axial-vector form factor from scattering neutrinos off liquid hydrogen targets are not being carried out due to safety concerns.

The MINERνA experiment [4] has recently shown that the axial-vector form factor of the nucleon can be extracted from the charged current elastic scattering process $\bar{\nu}_\mu H \to \mu^+ n$ in which the free proton in hydrogen (H) gets converted into a neutron. This opens the door to direct measurements of the nucleon axial-vector form factor without the need for extraction from scattering off nuclei, whose analysis involves

*integration.field@gmail.com
†rajan@lanl.gov
‡tanmoy@lanl.gov
§byoon@nvidia.com
‖hwlin@pa.msu.edu

nuclear corrections which have unresolved systematics, and making detailed comparisons with predictions from lattice QCD. For example, our result for the axial charge radius, $\langle r_A^2 \rangle = 0.439(56)_{\text{stat}}(34)_{\text{sys}}$ fm^2, given in Eq. (36), is consistent, within one combined sigma, with the MINERνA result, $\sqrt{\langle r_A^2 \rangle} = 0.73 \pm 0.17$ fm.

Similarly, recent advances in simulations of lattice QCD have enabled robust results for the nucleon charges that have been reviewed by the Flavor Lattice Averaging Group (FLAG) in their 2019 and 2021 reports [5,6]). Results for axial-vector form factors [7] are now available with $\lesssim$10% uncertainty as we show in this work. At the same time, there continues to be progress in nuclear many-body theory for the calculation of the neutrino-nucleus cross section [1].

In this work, we present lattice QCD results for the isovector axial, $G_A(Q^2)$, induced pseudoscalar, $\tilde{G}_P(Q^2)$, and pesudoscalar $G_P(Q^2)$ form factors, the axial, scalar and tensor isovector charges g_A^{u-d}, g_S^{u-d} and g_T^{u-d}, the axial charge radius squared $\langle r_A^2 \rangle$, the induced pseudoscalar coupling g_P^*, and the pion-nucleon coupling $g_{\pi NN}$.

The calculation has been done using thirteen ensembles generated with $2+1+1$-flavors of highly improved staggered quarks (HISQ) by the MILC collaboration [8]. The construction of nucleon two- and three-point correlation functions has been done using Wilson-clover fermions as described in [9]. The analysis of the data generated using this clover-on-HISQ formulation includes a study of excited state contributions (ESC) in the extraction of ground state matrix elements (GSME) and a simultaneous chiral-continuum-finite-volume (CCFV) fit to obtain results at the physical point, which throughout the paper will be defined as taking the continuum ($a = 0$) and infinite volume ($M_\pi L \to \infty$) limits at physical light quark masses in the isospin symmetric limit, $m_u = m_d$, which are set using the neutral pion mass ($M_{\pi^0} = 135$ MeV). The masses of the strange and charm quarks in the lattice generation have been tuned to be close to their physical values in each of the thirteen ensembles [8].

The three form factors $G_A(Q^2)$, $\tilde{G}_P(Q^2)$ and $G_P(Q^2)$ must, up to discretization errors, satisfy the constraint in Eq. (16) imposed by the partially conserved axial current (PCAC) relation $\partial_\mu A_\mu = 2mP$ between the axial and pseudoscalar currents. The decomposition of the matrix elements (ME) into form factors, given in Eqs. (1) and (2), assumes that they are GSME. Post-facto, deviations from the PCAC relation larger than those expected due to lattice discretization artifacts are indicative of residual ESC in the extraction of ME from the spectral decomposition of the three-point correlation functions. They point to the need for reevaluation of the key inputs in this analysis—the number and energies of the excited states that contribute significantly to the three-point functions. The strategies used to remove ESC are described in Secs. II B and V, and the use of the PCAC relation to evaluate how well ESC have been controlled is discussed in Sec. II C.

In Ref. [10], we showed that the standard method of taking the excited-state spectrum from fits to the nucleon two-point correlation function to analyze the three-point functions lead to form factors that fail the PCAC test by almost a factor of two on the physical pion mass ensemble $a09m130W$, and identified the cause as enhanced contributions to ME from multihadron, $N\pi$, excited states that have mass gaps smaller than of radial excitations [11,12]. These contributions had been missed in all prior lattice calculations. Including $N\pi$ excited states in the analysis reduces the disagreement to within 10%, an amount that can be attributed to discretization effects. In this paper, we include $N\pi$ states in the analysis of all thirteen ensembles described in Table I. Data from various analyses discussed in Secs. III A, III B, and IV B are then extrapolated to the physical point using simultaneous CCFV fits and results compared to understand systematics.

In order to extract g_A and $\langle r_A^2 \rangle$, we parametrize the Q^2 behavior of $G_A(Q^2)$ using the dipole and the model independent z-expansion. We find that the dipole ansatz does not provide a good fit and our final results are obtained using the model independent z-expansion. We show that the pion-pole dominance (PPD) hypothesis, Eq. (20), tracks the improvement observed in satisfying the PCAC relation when $N\pi$ states are included in the analysis. We, therefore, use it to parametrize $\tilde{G}_P(Q^2)$ and extract g_P^* and $g_{\pi NN}$ in Sec. IV. Similarly, the analysis of the ESC in isovector charges extracted from the forward matrix elements is carried out using information from both the 2- and 3-point correlation functions and the noninteracting energy of the lowest $N\pi$ state.

Our final result for the axial form factor, parametrized using the z^2 truncation, is given in Eq. (34); the axial charge obtained from extrapolating it to $Q^2 = 0$ in Eq. (30), and the charge radius in Eq. (31). The results for the induced pseudoscalar charge g_P^* and $g_{\pi NN}$ are given in Eqs. (44) and (45). Lastly, the results for the three isovector charges $g_{A,S,T}^{u-d}$ from the forward matrix elements are given in Eq. (50).

This paper is organized as follows. In Sec. II, we briefly review the notation and the methodology for the extraction of the three form factors: the axial, G_A, the induced pseudoscalar $\tilde{G}_P$, and the pseudoscalar, G_P, from matrix elements of the axial and pseudoscalar currents within ground state nucleons. In Sec. II B, we explain the three strategies used to remove the ESC to the three-point functions. The analysis of the form factors with respect to how well they satisfy the relations imposed between them by PCAC relation and the PPD hypothesis is presented in Sec. II C. Based on this analysis, we present our understanding of the excited states that contribute in Sec. II D. The parametrization of the axial form factors as a function of Q^2 and the extraction of the axial charge g_A and the charge radius squared $\langle r_A^2 \rangle$ is carried out in Sec. III. Parametrization of the induced pseudoscalar form factor, $\tilde{G}_P$, and the extraction of the induced pseudoscalar

TABLE I. The parameters of the $2+1+1$-flavor HISQ ensembles generated by the MILC collaboration and analyzed in this study are quoted from Ref. [8]. On two ensembles, $a06m310$ and $a06m220$, a second set of calculations labeled $a06m310W$ and $a06m220W$, have been done with a larger smearing size σ as described in Ref. [13]. In this clover-on-HISQ study, all fits are made versus $M_\pi^{\rm val}$, which is tuned to be close to the Goldstone pion mass $M_\pi^{\rm sea}$. The finite-size effects are analyzed in terms of $M_\pi^{\rm val}L$. Columns 7–10 give the values of the source-sink separation τ used in the calculation of the three-point functions, the number of configurations analyzed, and the number of measurements made using the high precision (HP) and the low precision (LP) truncation of the inversion of the Wilson-clover operator [14]. The last column gives the value of $Q^2|_{\rm max}$ for two cuts, $n^2 \le 6$ ($n^2 \le 5$ for the four $a06m310$ and $a06m220$ ensembles) and $n^2 \le 10$ used in the analysis. The full set of Q^2 values simulated on each ensemble are given in Tables X–XXII.

Ensemble ID	a (fm)	$M_\pi^{\rm sea}$ (MeV)	$M_\pi^{\rm val}$ (MeV)	$L^3 \times T$	$M_\pi^{\rm val}L$	τ/a	$N_{\rm conf}$	$N_{\rm meas}^{\rm HP}$	$N_{\rm meas}^{\rm LP}$	$Q^2\vert_{\rm max}^{n^2=6}$ (GeV)^2	$Q^2\vert_{\rm max}^{n^2=10}$
$a15m310$	0.1510(20)	306.9(5)	320.6(4.3)	$16^3 \times 48$	3.93	$\{5,6,7,8,9\}$	1917	7668	122,688	1.297	1.92
$a12m310$	0.1207(11)	305.3(4)	310.2(2.8)	$24^3 \times 64$	4.55	$\{8,10,12\}$	1013	8104	64,832	0.920	1.435
$a12m220S$	0.1202(12)	218.1(4)	225.0(2.3)	$24^3 \times 64$	3.29	$\{8,10,12\}$	946	3784	60,544	0.909	1.358
$a12m220$	0.1184(10)	216.9(2)	227.9(1.9)	$32^3 \times 64$	4.38	$\{8,10,12\}$	744	2976	47,616	0.568	0.884
$a12m220L$	0.1189(09)	217.0(2)	227.6(1.7)	$40^3 \times 64$	5.49	$\{8,10,12,14\}$	1000	4000	128,000	0.374	0.595
$a09m310$	0.0888(08)	312.7(6)	313.0(2.8)	$32^3 \times 96$	4.51	$\{10,12,14,16\}$	2263	9052	114,832	0.961	1.421
$a09m220$	0.0872(07)	220.3(2)	225.9(1.8)	$48^3 \times 96$	4.79	$\{10,12,14,16\}$	964	7712	123,392	0.470	0.736
$a09m130W$	0.0871(06)	128.2(1)	138.1(1.0)	$64^3 \times 96$	3.90	$\{8,10,12,14,16\}$	1290	5160	165,120	0.277	0.443
$a06m310$	0.0582(04)	319.3(5)	319.6(2.2)	$48^3 \times 144$	4.52	$\{16,20,22,24\}$	1000	8000	64,000	0.840	
$a06m310W$						$\{18,20,22,24\}$	500	2000	64,000	0.846	
$a06m220$	0.0578(04)	229.2(4)	235.2(1.7)	$64^3 \times 144$	4.41	$\{16,20,22,24\}$	650	2600	41,600	0.504	
$a06m220W$						$\{18,20,22,24\}$	649	2596	41,546	0.509	
$a06m135$	0.0570(01)	135.5(2)	135.6(1.4)	$96^3 \times 192$	3.7	$\{16,18,20,22\}$	675	2700	43,200	0.294	0.475

coupling g_P^* and the pion-nucleon coupling $g_{\pi NN}$ is carried out in Sec. IV. The calculation of the isovector charges $g_{A,S,T}^{u-d}$ from forward matrix elements is described in Sec. V. A summary of our results and a comparison with previous lattice calculations is presented in the concluding Sec. VI. Six Appendices give further details of the analysis and the data.

II. METHODOLOGY FOR EXTRACTING THE FORM FACTORS

The matrix elements of the axial $A_\mu = \bar{u}\gamma_\mu\gamma_5 d$ and pseudoscalar $P = \bar{u}\gamma_5 d$ currents between the ground state of the nucleon can be decomposed, in the isospin symmetric limit, into the axial G_A, induced pseudoscalar $\tilde{G}_P$, and pseudoscalar G_P form factors as

$$\langle N(\vec{p}_f)|A_\mu(\vec{Q})|N(\vec{p}_i)\rangle = \bar{u}(\vec{p}_f)\left[G_A(Q^2)\gamma_\mu\gamma_5 + q_\mu\gamma_5\frac{\tilde{G}_P(Q^2)}{2M}\right]u(\vec{p}_i), \quad (1)$$

$$\langle N(\vec{p}_f)|P(\vec{q})|N(\vec{p}_i)\rangle = \bar{u}(\vec{p}_f)[G_P(Q^2)\gamma_5]u(\vec{p}_i), \quad (2)$$

where $u(\vec{p}_i)$ is the nucleon spinor with momentum $\vec{p}_i$, $q = p_f - p_i$ is the momentum transferred by the current, $Q^2 = -q^2 = \vec{p}_f^{\,2} - (E(\boldsymbol{p}_f) - E(\boldsymbol{p}_i))^2$ is the spacelike four momentum squared transferred. The spinor normalization used is

$$\sum_s u(\boldsymbol{p},s)\bar{u}(\boldsymbol{p},s) = \frac{E(\boldsymbol{p})\gamma_4 - i\gamma\cdot\boldsymbol{p} + M}{2E(\boldsymbol{p})}. \quad (3)$$

The process of obtaining the GSME needed in Eqs. (1) and (2) from fits to 2- and 3-point correlation functions is described next.

A. Two- and three-point correlation functions

The lattice calculation starts with the measurement and analysis of the two- and three-point correlation functions $C^{\rm 2pt}(\boldsymbol{p};\tau)$ and $C_J(\boldsymbol{q},t;\tau)$ constructed using the nucleon interpolating operator $\mathcal{N}$,

$$\mathcal{N}(x) = \epsilon^{abc}\left[q_1^{aT}(x)C\gamma_5\frac{1\pm\gamma_4}{2}q_2^b(x)\right]q_1^c(x), \quad (4)$$

where the $\pm$ sign give positive parity states propagating forward/backward in time. The spectral decompositions of the two time-ordered correlation functions are

$$C^{\rm 2pt}(\boldsymbol{p};\tau) \equiv \langle\Omega|\mathcal{T}(\mathcal{N}(\tau)\bar{\mathcal{N}}(0))|\Omega\rangle = \sum_{i=0}|A_i'|^2 e^{-E_i\tau}, \quad (5)$$

and

$$C_J(\boldsymbol{q};t,\tau) \equiv \langle\Omega|\mathcal{T}(\mathcal{N}(\tau)J_\Gamma(t)\bar{\mathcal{N}}(0))|\Omega\rangle, = \sum_{i,j=0}A_i'^* A_j\langle i'|J_\Gamma|j\rangle e^{-E_i t - M_j(\tau-t)}, \quad (6)$$

where $J_\Gamma = A_\mu$ or P is the quark bilinear current inserted at time t with momentum $\boldsymbol{q}$, and $|\Omega\rangle$ is the vacuum state.

In our set up, the nucleon state $|j\rangle$ is, by construction, projected to zero momentum, i.e., $p_j = (M, \mathbf{0})$, whereas $\langle i'|$ is projected onto definite momentum $p_i = (E, \boldsymbol{p})$ with $\boldsymbol{p} = -\boldsymbol{q}$ by momentum conservation. Consequently, the states on the two sides of the inserted operator J are different for all $\mathbf{q} \neq 0$. The prime in $\langle i'|$ indicates that this state can have nonzero momentum.

For large time separations, τ and $\tau - t$, only the ground state contributes and the GSME, $\langle 0'|J|0\rangle$, whose Lorentz covariant decomposition is given in Eqs. (1) and (2), can be extracted reliably. Assuming this is the case, and choosing the nucleon spin projection to be in the "3" direction, the decompositions become

$$C_{A_i}(\boldsymbol{q}) \to K^{-1}\left[-q_i q_3 \frac{\tilde{G}_P}{2M} + \delta_{i3}(M+E)G_A\right], \quad (7)$$

$$C_{A_4}(\boldsymbol{q}) \to K^{-1} q_3 \left[(M-E)\frac{\tilde{G}_P}{2M} + G_A\right], \quad (8)$$

$$C_P(\boldsymbol{q}) \to K^{-1} q_3 G_P, \quad (9)$$

where $i \in 1, 2, 3$ and the kinematic factor $K \equiv \sqrt{2E(E+M)}$. These correlation functions are complex valued, and the signal, for the CP symmetric theory, is in $\mathrm{Im}C_{A_i}$, $\mathrm{Re}C_{A_4}$, and $\mathrm{Re}C_P$.

For a given $\boldsymbol{q}^2 \neq 0$, the correlators with momentum combinations $\mathbf{q} = (2\pi/L)\mathbf{n} \equiv (2\pi/L)(n_1, n_2, n_3)$ related by cubic symmetry can be averaged to increase the statistics before making fits. We construct the following averages $\bar{A}_\mu$ and $\bar{P}$:

$$\overline{A}_i(\boldsymbol{q}^2) \equiv \frac{1}{\alpha_1 \boldsymbol{q}^2}\sum_{\boldsymbol{q}} \mathrm{sgn}(q_i q_3) C_{A_i}(\boldsymbol{q}) \to K^{-1}\frac{\tilde{G}_P}{2M}, \qquad (i = 1, 2), \quad (10)$$

$$\overline{A}_{3,L}(\boldsymbol{q}^2) \equiv \frac{1}{\alpha_3 \boldsymbol{q}^2}\sum_{q_3 \neq 0} C_{A_3}(\boldsymbol{q}) \to K^{-1}\left[-\frac{\tilde{G}_P}{2M} + \frac{(N-\beta)}{\alpha_3 \boldsymbol{q}^2}(M+E)G_A\right], \quad (11)$$

$$\overline{A}_{3,T}(\boldsymbol{q}^2) \equiv \frac{1}{\beta}\sum_{q_3=0} C_{A_3}(\boldsymbol{q}) \to K^{-1}(M+E)G_A, \quad (12)$$

$$\bar{A}_4(\boldsymbol{q}^2) \equiv \frac{1}{\alpha_3 \boldsymbol{q}^2}\sum_{\boldsymbol{q}} q_3 C_{A_4}(\boldsymbol{q}) \to K^{-1}\left[(M-E)\frac{\tilde{G}_P}{2M} + G_A\right], \quad (13)$$

$$\bar{P}(\boldsymbol{q}^2) \equiv \frac{1}{\alpha_3 \boldsymbol{q}^2}\sum_{\boldsymbol{q}} q_3 C_P(\boldsymbol{q}) \to K^{-1} G_P, \quad (14)$$

where $\mathrm{sgn}(x) = x/|x|$ is a sign function with $\mathrm{sgn}(0) = 0$, $\alpha_1 \equiv \sum |n_1 n_3|/\boldsymbol{n}^2$, $\alpha_3 \equiv \sum_{q_3} n_3^2/\boldsymbol{n}^2 = N/3$, $\boldsymbol{q} = (2\pi/L)\boldsymbol{n}$, $\beta \equiv \sum_{q_3=0} 1$, and $N \equiv \sum_{\boldsymbol{q}} 1$ is the number of equivalent (under the cubic group) momenta averaged.

The pseudoscalar form factor, G_P, is given uniquely by Eq. (14). For a subset of momenta, G_A and $\tilde{G}_P$ are determined uniquely from Eqs. (10) and (12). In general, we solve the over-determined system of equations, Eqs. (10)–(13). Of these, correlators $\bar{A}_{3,L}$ and $\bar{A}_4$ are nonvanishing for all $\boldsymbol{q}$, and are thus sufficient to solve for G_A and $\tilde{G}_P$. In practice, the A_4 correlator has a poor signal and is dominated by excited states contributions, which we exploit to determine the relevant low-lying excited states. These turn out to be towers of multihadron $N\pi$ and $N\pi\pi$ states. We find that including these states in fits to the spectral decompositions given in Eqs. (5) and (6) is essential for extracting the GSME. With the GSME in hand, the form factors G_A and $\tilde{G}_P$ are determined using Eqs. (10)–(12).

B. Strategies to extract ground state matrix elements

Calculations of nucleon correlation functions face two key challenges. First, the statistical signal-to-noise ratio decays exponentially with the source-sink separation τ as $e^{-(M_N - 1.5M_\pi)\tau}$ [15,16]. This limits current measurements of two-point (three-point) functions to $\lesssim 2$ ($\lesssim 1.5$) fm. Second, at these τ, the residual contribution of many theoretically allowed radial and multihadron excited states can be significant. These states arise because the standard nucleon interpolating operator $\mathcal{N}$, defined in Eq. (4), used to construct the correlation functions in Eqs. (5) and (6), couples to nucleons and all its excitations with positive parity including multihadron states, the lowest of which are $N(\mathbf{p})\pi(-\mathbf{p})$ and $N(\mathbf{0})\pi(\mathbf{0})\pi(\mathbf{0})$. The goal is to remove the contributions of all these excited states to three-point functions to obtain the GSME, $\langle 0'|J|0\rangle$, which we do by fitting the averaged correlators $\bar{A}_\mu$ and $\bar{P}$ using Eq. (6).

An important note applicable to all fits used to remove excited states. For all our ensembles, the energy of the two lowest in these towers of positive parity states, $N(\mathbf{p} = 1) \times \pi(\mathbf{p} = -1)$ and $N(\mathbf{0})\pi(\mathbf{0})\pi(\mathbf{0})$, are approximately the same. Since fits to Eqs. (5) and (6) depend only on E_i and not on the nature of the states, the contribution of both states is taken into account using the E_1 calculated for either state. Thus, the reader should understand that the contribution of both states are being included when, for brevity, we say $N\pi$ state.

To extract the GSME, we need to address two questions: (i) which excited states make large contributions and (ii) how large is this contribution to various observables. The most direct (and statistically the best motivated assuming that a common set of states dominate the ESC in all correlators) way to get the ground-state matrix element that addresses these questions is to simultaneously

fit, with the full covariance matrix, all five nucleon three-point functions including two or more excited states, and then solve the linear set of Eqs. (10)–(14).

In general, simultaneous fits to the current data (3-point or a combination of 2- and 3-point) do not resolve the excited states, i.e., there are large regions of parameter space where fits give similar χ^2/d.o.f. The one exception is fits to the correlation functions $\langle NA_4N\rangle$ that, as discussed below, play a central role in our analysis as they expose the large contribution of $N\pi$ states. Unfortunately, even 2-state simultaneous fits to all five nucleon three-point functions are not stable for all momentum channels and ensembles. We, therefore, resort to taking the energies and amplitudes, especially those of the ground state, from separate, but within a single overall jackknife process, fits to the 2-point function.

The analysis of the nucleon two-point functions and the extraction of the spectrum is presented in Appendix A and the extrapolation of the data for the nucleon mass, M_N, to the continuum limit in Appendix B. Results for the excited state parameters, i.e., the energies $E_i(\boldsymbol{q})$, the masses M_i, and the amplitudes A_i, have large uncertainty. For example, in a four state fit, there is a large region of parameter space where fits have similar χ^2/d.o.f.

In short, statistical precision of current data does not allow simultaneous fits to all five nucleon three-point functions using a 3-state (or higher) fit with the full covariance matrix. Even a robust determination of the energies, E_i, and amplitudes, A_i, of excited states that make significant contributions from fits to 2-point functions is lacking. Our best approach is a hybrid of using information from fits to 2- and 3-point functions. To this end, we construct three strategies with different estimates of excited-state parameters to fit the three-point data using Eq. (6). These are described next.

In the standard approach, labeled $S_{2\text{pt}}$, we take E_i, M_j, A_0' and A_0 from 4-state fits to $C^{2\text{pt}}$, and input them into an m-state truncation ($m \le n$) of Eq. (6) to extract the matrix element $\langle 0'|J|0\rangle$. In this paper, we truncate the spectral decompositions given in Eqs. (5) and (6) at $m = 3$ and $n = 4$, respectively.

The second strategy, labeled $\mathcal{S}_{A4}$, was proposed in Ref. [10]. Again E_0, M_0, A_0' and A_0 are taken from 4-state fits to $C^{2\text{pt}}$, however, E_1 and M_1 are determined from two-state fits to the three-point correlator $\bar{A}_4$. The output E_1 and M_1 are then fed into the fits to the other four correlation functions defined in Eqs. (10)–(12), and (14). This strategy assumes that the same [first] excited state parameters apply to all five correlation functions, and these are given by fits to $\bar{A}_4$.

The third strategy $\mathcal{S}_{\text{sim}}$ is similar to $\mathcal{S}_{A4}$ except that E_1 and M_1 are outputs of simultaneous two-state fits to all five three-point correlators defined in Eqs. (10)–(14). It is, from a statistical point of view, better motivated than $\mathcal{S}_{A4}$ because the underlying assumption in both cases is that the same excited states contribute to all five correlators. It avoids the two-step procedure used in $\mathcal{S}_{A4}$, i.e., first obtain E_1 and M_1 from fits to $\bar{A}_4$ and then use them in fits to the other four correlators. In $\mathcal{S}_{\text{sim}}$, we used the averaged correlator $\bar{A}_{xy} = (\bar{A}_1 + \bar{A}_2)/2$, since these two correlators are equivalent under cubic rotational symmetry, thus reducing the number of correlators fit simultaneously to four.

We used the full covariance matrix for all fits to the 2-point and 3-point functions with the $\mathcal{S}_{2\text{pt}}$ and $\mathcal{S}_{A4}$ strategies. In the $\mathcal{S}_{\text{sim}}$ strategy, the covariance matrix was restricted to be block diagonal in each correlation function. In the $O(1000)$ fits made to remove ESC (ensembles $\otimes$ Q^2 values $\otimes$ correlation functions $\otimes$ strategies) the selection of parameters was done individually due to the large differences in ESC behavior versus ensembles, Q^2 values, and correlation functions.

We emphasize from the very outset that in all fits with each of the three strategies, the excited state amplitudes, $A_i^{(\prime)}$ and A_j, are not needed since these arise only in the combinations $|A_i'||A_j|\langle i'|J|j\rangle$, which are fit parameters but are not used thereafter in the analysis. Second, the ground state parameters, M_0, E_0, A_0' and A_0 are common for all three strategies and are taken from four-state fits to the two-point correlators.

The unrenormalized values of the three form factors at various values of Q^2 simulated, for each of the three strategies and for the 13 ensembles are given in Tables X–XXII in Appendix C. The size of the effect of $N\pi$ state can already be inferred from the difference between the $\mathcal{S}_{2\text{pt}}$ and $\mathcal{S}_{\text{sim}}$ data even though $\mathcal{S}_{\text{sim}}$ includes only the lowest $N(-1)\pi(1)$ state in the fit. Overall, this comparison shows that the contribution of the $N\pi$ state to $\tilde{G}_P$ and G_P is enhanced, reaching ~45% at the physical pion mass. The roughly 5% effect observed in G_A is important phenomenologically and needs to be made more precise. Later, in Sec. II C, we choose the $\mathcal{S}_{\text{sim}}$ strategy to present the final results based on the three form factors satisfying the PCAC relation.

A comparison of $G_A(Q^2)$ and the combination $\tilde{G}_P(Q^2) \times (Q^2 + M_\pi^2)/(4M_N^2)$, which should be proportional to G_A according to the PPD hypothesis, obtained using the three strategies $\mathcal{S}_{2\text{pt}}$, $\mathcal{S}_{A4}$, and $\mathcal{S}_{\text{sim}}$, is shown in Fig. 1. Results for both form factors are consistent between $\mathcal{S}_{A4}$ and $\mathcal{S}_{\text{sim}}$ for each of thirteen ensembles with errors from $\mathcal{S}_{\text{sim}}$ being slightly larger. On the other hand $\tilde{G}_P$ (and G_P) from strategy $\mathcal{S}_{2\text{pt}}$ show noticeable differences that increase as $Q^2 \to 0$ and $M_\pi \to 135$ MeV (see also the data in X–XXII in Appendix C). This effect is correlated with the increase in the difference between $\Delta E_1^{2\text{pt}}$ (used in $\mathcal{S}_{2\text{pt}}$ fits) compared to ΔE_1^{A4} and ΔM_1^{A4} (output of $\mathcal{S}_{\text{sim}}$ fits) in the same two limits as shown later in Fig. 6. Also, from Eq. (6) it is obvious that a smaller ΔE_1 implies a larger ESC.

The same data for $G_A(Q^2)$ and $\tilde{G}_P(Q^2) \times (Q^2 + M_\pi^2)/(4M_N^2)$ from the 13 ensembles with the $\mathcal{S}_{\text{sim}}$ strategy are

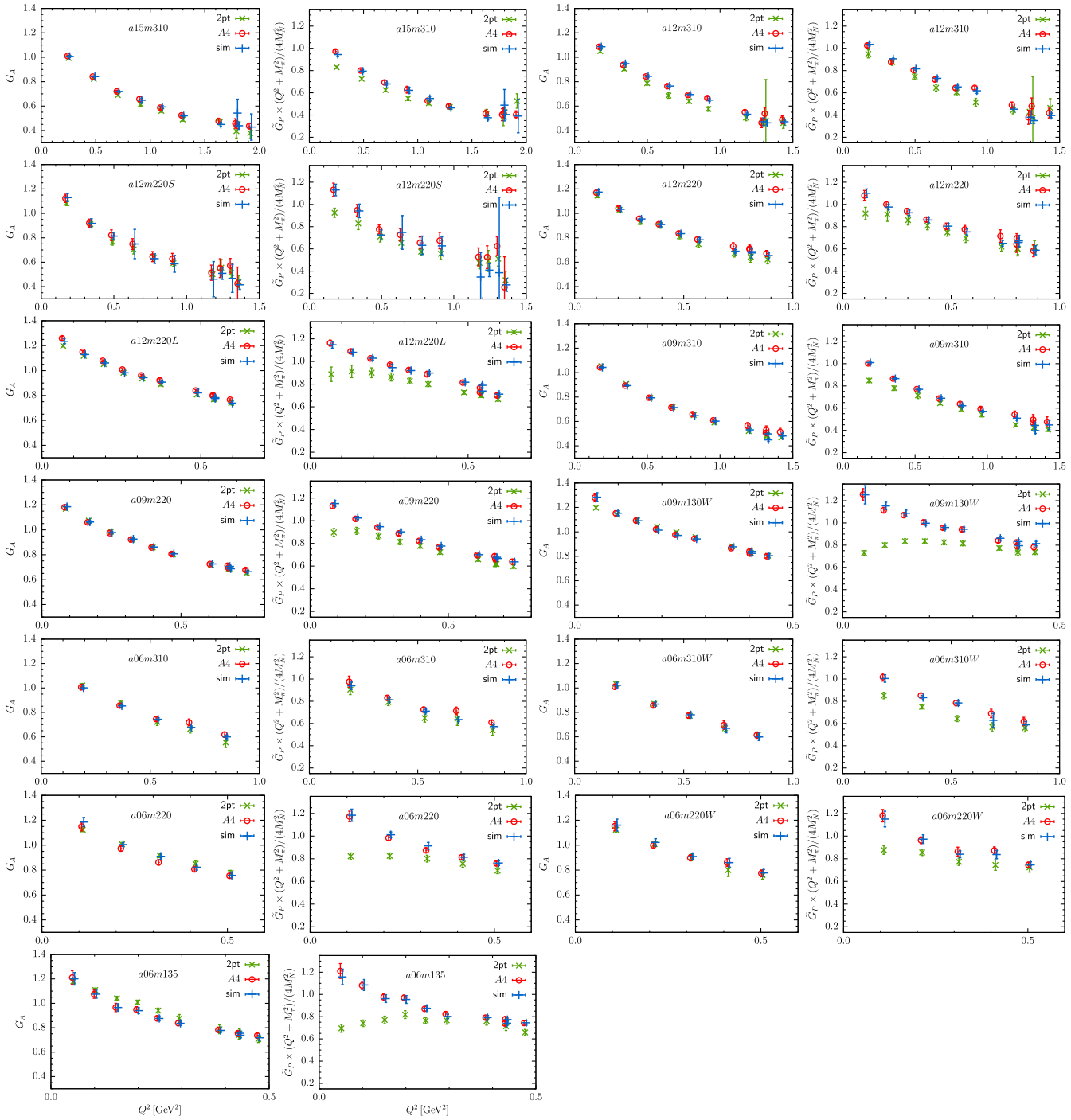

FIG. 1. Data from the 13 ensembles with $a \approx 0.15$, 0.12, 0.09, and 0.06 fm for the unrenormalized axial form factor $G_A(Q^2)$ (first and third columns) and $(Q^2 + M_\pi^2)\tilde{G}_P(Q^2)/(4M_N^2)$ (second and fourth columns) plotted versus Q^2. Each panel compares the data obtained using the three strategies $\mathcal{S}_{\rm 2pt}$, $\mathcal{S}_{A4}$, and $\mathcal{S}_{\rm sim}$ for controlling ESC.

plotted in Fig. 2. Remarkably, they show no significant variation with respect to the lattice spacing a or M_π except for a 1σ lower values on the $a06m135$ ensemble, which we identify to be statistics limited.

In Appendix C we summarize why, with the methodology for momentum insertion through the operator used in this work, improving the lattice calculations ($M_\pi \to 135$ MeV, increasing $M_\pi L > 4$, and reducing a) will increasingly give data at $Q^2 < 0.5$ GeV^2. Even in this work, most of the data for $Q^2 > 0.7$ GeV^2 comes from the $M_\pi \approx 310$ MeV ensembles. If the optimistic scenario presented by the current data, mild dependence on $\{a, M_\pi\}$ as shown in Fig. 2 and in Ref. [7], holds then one will have confidence in the final result for G_A also for

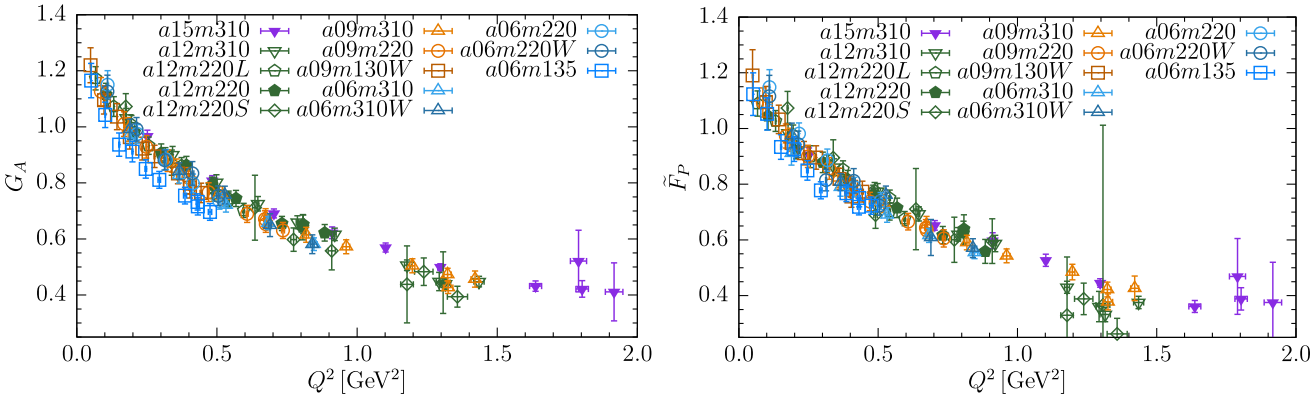

FIG. 2. The data for renormalized $G_A(Q^2)$ (left) and $\tilde{F}_P(Q^2) \equiv \tilde{G}_P(Q^2) \times (Q^2 + M_\pi^2)/(4M_N^2)$ (right) from the 13 HISQ ensembles analyzed. No significant variation with respect to the lattice spacing a or M_π is observed except for the $a06m135$ ensemble, which we consider statistics limited.

$0.5 \lesssim Q^2 \lesssim 1.5$ GeV^2 even though its extraction in that region will be from data on $M_\pi > 200$ MeV ensembles. To push precision to $Q^2 \sim 5$ GeV^2 to meet the needs of the DUNE experiment will need further algorithmic developments and much higher statistics data.

A detailed analysis of the extrapolation of these G_A to $Q^2 \to 0$ to get the axial charge g_A is presented in Sec. III. The marked improvement in satisfying the PCAC relation and the PPD hypothesis shown by the G_A, $\tilde{G}_P$, and G_P obtained with the $\mathcal{S}_{A4}$ and $\mathcal{S}_{\rm sim}$ strategies (which include the $N\pi$ state) is discussed next in Sec. II C.

C. The PCAC relation and pion-pole dominance

In this section, we evaluate how well the form factors from the three strategies, tabulated in Appendix C, satisfy the PCAC relation, which in terms of the bare axial, $A_\mu(x)$, and pseudoscalar, $P(x)$, currents is

$$\partial_\mu A_\mu = 2\hat{m} P, \tag{15}$$

where the quark mass parameter $\hat{m} \equiv Z_m m_{ud} Z_P Z_A^{-1}$ includes all the renormalization factors, and $m_{ud} = (m_u + m_d)/2 = m_l$ is the light quark mass in the isospin symmetric limit. Using the decomposition in Eqs. (1) and (2) of GSME, the PCAC relation requires that the three form factors G_A, $\tilde{G}_P$, and G_P satisfy, up to discretization errors, the relation

$$2M_N G_A(Q^2) - \frac{Q^2}{2M_N}\tilde{G}_P(Q^2) = 2\hat{m} G_P(Q^2), \tag{16}$$

which we rewrite as

$$R_1 + R_2 = 1, \tag{17}$$

with

$$R_1 = \frac{Q^2}{4M_N^2}\frac{\tilde{G}_P(Q^2)}{G_A(Q^2)}, \tag{18}$$

$$R_2 = \frac{\hat{m}}{M_N}\frac{G_P(Q^2)}{G_A(Q^2)}. \tag{19}$$

The PPD hypothesis relates $\tilde{G}_P$ to G_A as

$$R_3 \equiv \frac{Q^2 + M_\pi^2}{4M_N^2}\frac{\tilde{G}_P(Q^2)}{G_A(Q^2)} = 1. \tag{20}$$

Tests of whether the form factors satisfy the PCAC ($R_1 + R_2 = 1$) and PPD ($R_3 = 1$) relations are presented in Figs. 3 and 4, respectively. Data with the $\mathcal{S}_{\rm 2pt}$ strategy show about 10% deviation for both the PPD and PCAC relations for $Q^2 > 0.3$ GeV^2. Below it, the deviation grows to about 40% at the lowest Q^2 point on the two physical pion mass ensembles. See also the discussion in Appendix C on the differences in data for the form factors obtained using the three ESC strategies.

There is a very significant reduction in the deviations for both the $\mathcal{S}_{A4}$ and $\mathcal{S}_{\rm sim}$ strategies for $Q^2 < 0.3$ GeV^2. In fact, except for three $M_\pi \approx 220$ MeV ensembles, data below $Q^2 = 1$ GeV^2 is essentially independent of Q^2 and the deviations from unity and the variations between ensembles is in most cases within about 5%, which can be due to possible discretization errors. The differences between data with $\mathcal{S}_{\rm sim}$ and $\mathcal{S}_{A4}$ are much smaller. Also, the improvement in the PPD relation, Eq. (20), tracks that in PCAC, Eq. (17).

We point out a caveat in our clover-on-HISQ calculation of the quark mass $\hat{m}$ used in Eq. (16). For four ensembles, $a12m310$, $a09m130W$, $a06m220$, and $a06m135$ we have calculated $\hat{m}^{\rm 2pt}$ using the following ratio of pion two-point correlators,

$$2\hat{m}^{\rm 2pt} = \frac{\langle\Omega|\partial_\mu A_\mu(t)P(0)|\Omega\rangle}{\langle\Omega|P(t)P(0)|\Omega\rangle}. \tag{21}$$

For the other ensembles, the data for these two-point functions were not collected, so we use the HISQ sea

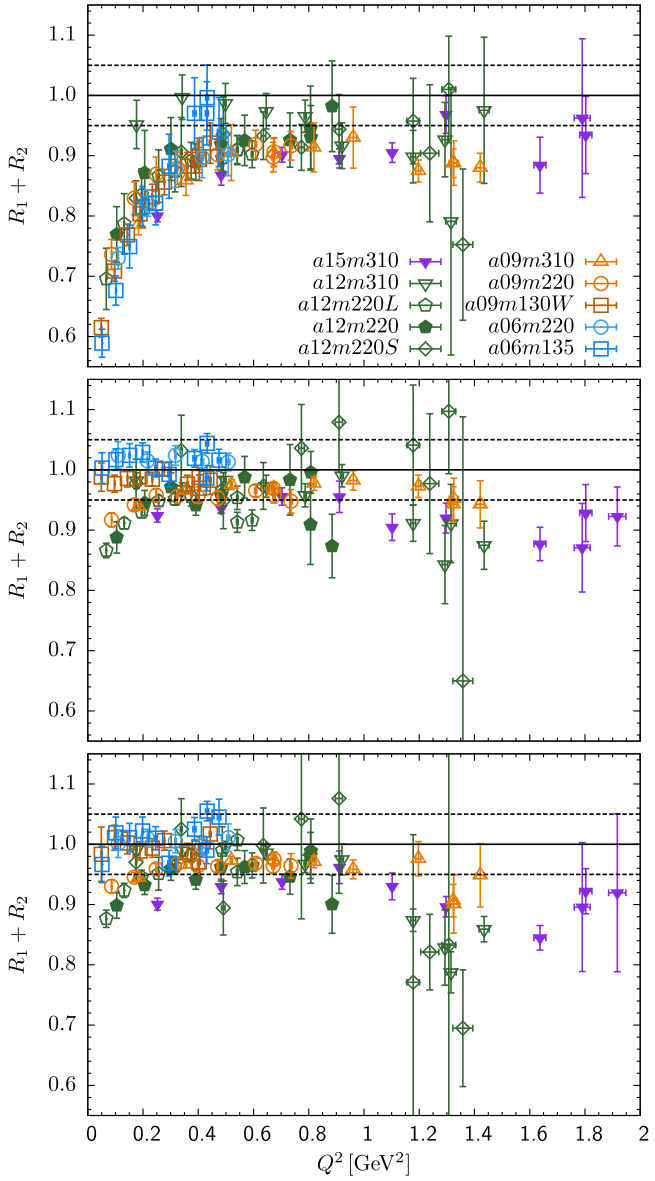

FIG. 3. The data for $R_1 + R_2$, which should equal unity to satisfy PCAC relation, is plotted versus Q^2 for analysis strategies $\mathcal{S}_{2\text{pt}}$ (top), $\mathcal{S}_{A4}$ (middle), and $\mathcal{S}_{\text{sim}}$ (bottom). The PCAC relation, Eqs. (15) and (16), requires $R_1 + R_2 = 1$ up to discretization errors. The dashed lines give the $\pm 5\%$ deviation band.

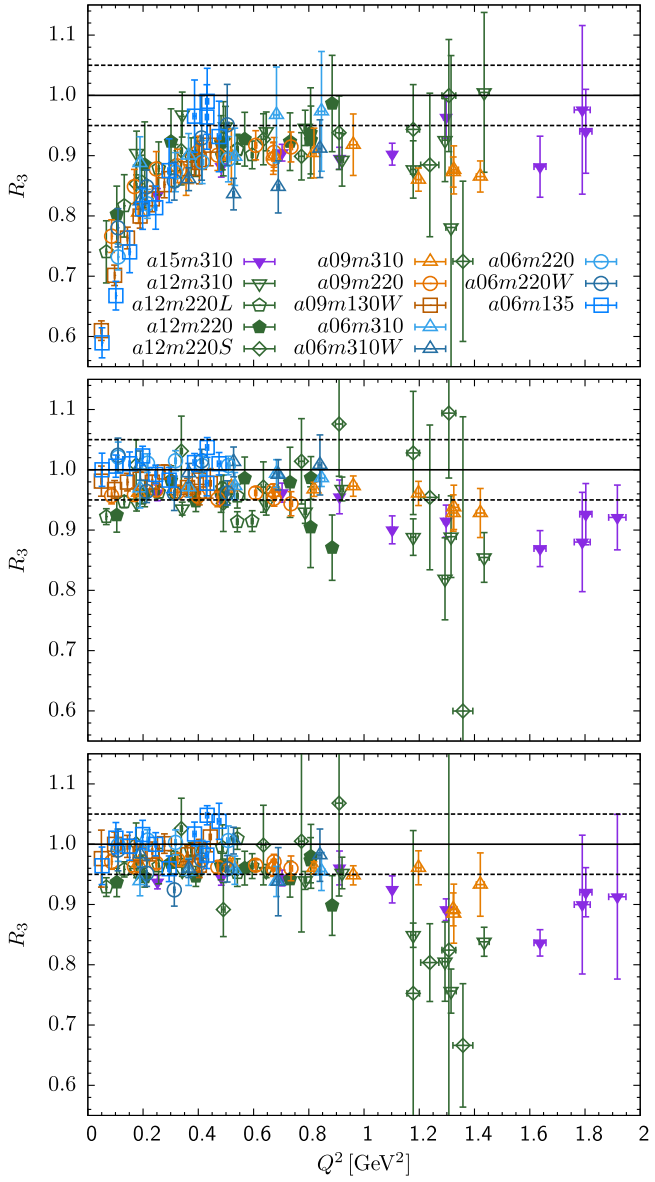

FIG. 4. The ratio R_3, which should be unity for the pion-pole dominance hypothesis to be satisfied, is plotted versus Q^2 for analysis strategies $\mathcal{S}_{2\text{pt}}$ (top), $\mathcal{S}_{A4}$ (middle), and $\mathcal{S}_{\text{sim}}$ (bottom). The dashed lines mark the $\pm 5\%$ deviation band.

quark mass am_{ud}^{sea} for $\hat{m}$ since for staggered fermions, in fact all lattice fermions with chiral symmetry, $Z_m Z_P Z_A^{-1} = 1$. These quark masses are given in Table II and we find that $\hat{m}^{2\text{pt}}$ is 5–20% larger than am_{ud}^{sea}, which is not unexpected for our clover-on-HISQ calculation. Noting that $R_2 \approx 0.5 R_1$ (see Fig. 15 in Ref. [9]), such a 20% systematic error would increase $R_1 + R_2$ by about 7%. This would bring the data from the physical mass ensembles, $a09m130W$ and $a06m135$, in better agreement but would not alter our conclusion that form factors obtained with $\mathcal{S}_{A4}$ and $\mathcal{S}_{\text{sim}}$ strategies show better agreement with the PCAC relation compared to $\mathcal{S}_{2\text{pt}}$. Also, $\hat{m}$ does not enter in the PPD relation, Eq. (20), and the deviation from unity of the PPD relation with $\mathcal{S}_{A4}$ and $\mathcal{S}_{\text{sim}}$ data is observed to be smaller than seen in the PCAC relation as shown in Fig. 4. Equally important, this caveat does not impact the extraction of individual form factors or their subsequent analysis since $\hat{m}$ only enters in the test of how well the three form factors satisfy the PCAC relation, Eq. (16).

We further examine whether the deviation from unity in Fig. 3 at small Q^2 is a discretization error. The $\mathcal{O}(a)$ improvement affects only the axial current, $A_\mu \to A_\mu + c_A a \partial_\mu P$, and adds to the left hand side in Eq. (16) the term $-Q^2 a c_A G_P$, i.e., under improvement, Eq. (16) can be written as

TABLE II. The HISQ sea quark mass is given in the second column. The quark mass $\hat{m}$ is calculated from Eq. (21).

ID	am_{ud}^{sea}	$a\hat{m}^{\mathrm{2pt}}$
$a15m310$	0.013	...
$a12m310$	0.0102	0.0121
$a12m220L$	0.00507	...
$a12m220$	0.00507	...
$a12m220S$	0.00507	...
$a09m310$	0.0074	...
$a09m220$	0.00363	...
$a09m130W$	0.0012	0.0015
$a06m220$	0.0024	0.0028
$a06m135$	0.00084	0.00088

$$M_N \frac{G_A}{G_P} - \frac{Q^2}{4M_N}\frac{\tilde{G}_P}{G_P} = \hat{m} + \frac{1}{2} a c_A Q^2, \tag{22}$$

where the improvement coefficient, c_A, is typically $\mathcal{O}(10^{-2})$ and negative. Thus, this effect is expected to be small for $Q^2 < 1$ GeV^2, and will not change our conclusions. On the other hand, effects due to possible mistuning of the clover coefficient, c_{SW}, and c_A, and $O(a^2)$ corrections are likely to increase with Q^2. Similarly, artifacts are expected to increase with the quark mass since the improvement coefficient b_m is not included.

The PPD relation [Eq. (20)] can be derived from PCAC [Eq. (16)] provided

$$R_4 \equiv \frac{4\hat{m}M_N}{M_\pi^2}\frac{G_P}{\tilde{G}_P} = 1. \tag{23}$$

In this case, $R_1 + R_2 = 1$ would also imply $R_3 = 1$. In Fig. 5, we compare R_4 from the three strategies for all ensembles except $a06m220W$, $a06m310$, and $a06m310W$ where G_P is not available. We note a roughly linear increase in R_4 with Q^2, which is consistent with the behavior observed in Ref. [7] and with the analysis of the Goldberger-Trieman discrepancy using χPT in Ref. [17]. Lastly, we note that the data for R_4 from all three strategies, $\mathcal{S}_{\mathrm{2pt}}$, $\mathcal{S}_{A4}$ and $\mathcal{S}_{\mathrm{sim}}$, overlap implying that the changes in $\tilde{G}_P$ and G_P, both of which have a pion pole, between different treatments of ESC ($\mathcal{S}_{\mathrm{2pt}}$ versus $\mathcal{S}_{A4}$ or $\mathcal{S}_{\mathrm{sim}}$) cancel in the ratio R_4 within our statistics. This observation supports our hypothesis that the same excited states contribute to all five correlation functions.

D. Excited states spectrum

In Fig. 6 we show data for the energy gaps, ΔE_1 and ΔM_1 on the two sides of the operator insertion for the various ensembles, including the two physical pion mass ones, $a09m130W$ and $a06m135$. The results for ΔE_1^A and ΔM_1^A, outputs of the simultaneous fits to all five correlators (insertions of A_μ and P) at a given momentum transfer

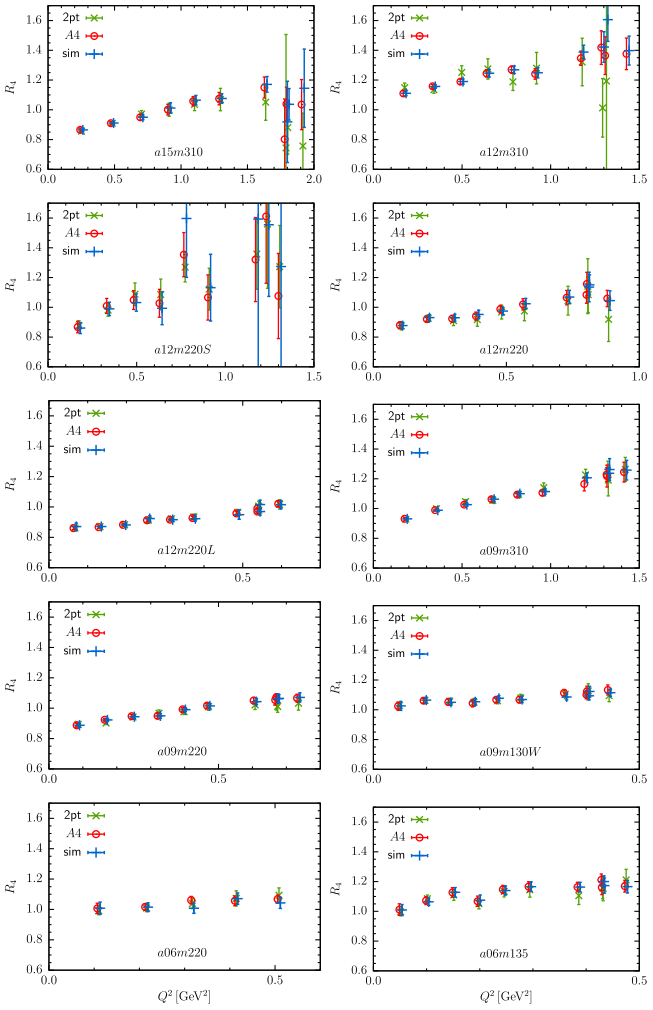

FIG. 5. Results for the ratio $R_4 = (G_P/\tilde{G}_P) \times (4\hat{m}M_N/M_\pi^2)$. For the pion-pole dominance hypothesis to be exact (derivable from the PCAC relation), R_4 should be unity independent of Q^2. The data show an approximate linear increase with Q^2, which is consistent with the Goldberger-Trieman discrepancy as discussed in Refs. [7,17].

$\boldsymbol{p} = 2\pi\boldsymbol{n}/L$ overlap with the results ΔE_1^{A4} and ΔM_1^{A4} obtained from fits to just C_{A_4}. This indicates that the energy gaps in the $\mathcal{S}_{\mathrm{sim}}$ fits are essentially controlled by C_{A_4}. The momentum dependence of the data is consistent with the expectation that the relevant excited states on the two sides are $N(\boldsymbol{n}) + \pi(-\boldsymbol{n})$ and $N(\boldsymbol{0}) + \pi(-\boldsymbol{n})$. This is based on the rough agreement between the data and the corresponding noninteracting energies of these states, ΔM_1 and ΔE_1, shown by the dashed red and blue lines, respectively, and consistent with the PPD hypothesis that the currents inject a pion with momentum $\vec{q}$.

The data with open circles in Fig. 6 are the energy gaps $\Delta E_1^{\mathrm{2pt}}$ obtained from the nucleon two-point correlators. These are roughly independent of momentum and larger than those from $\mathcal{S}_{A4}$ or $\mathcal{S}_{\mathrm{sim}}$ fits, especially for the smaller Q^2 points. The difference increases as $Q^2 \to 0$

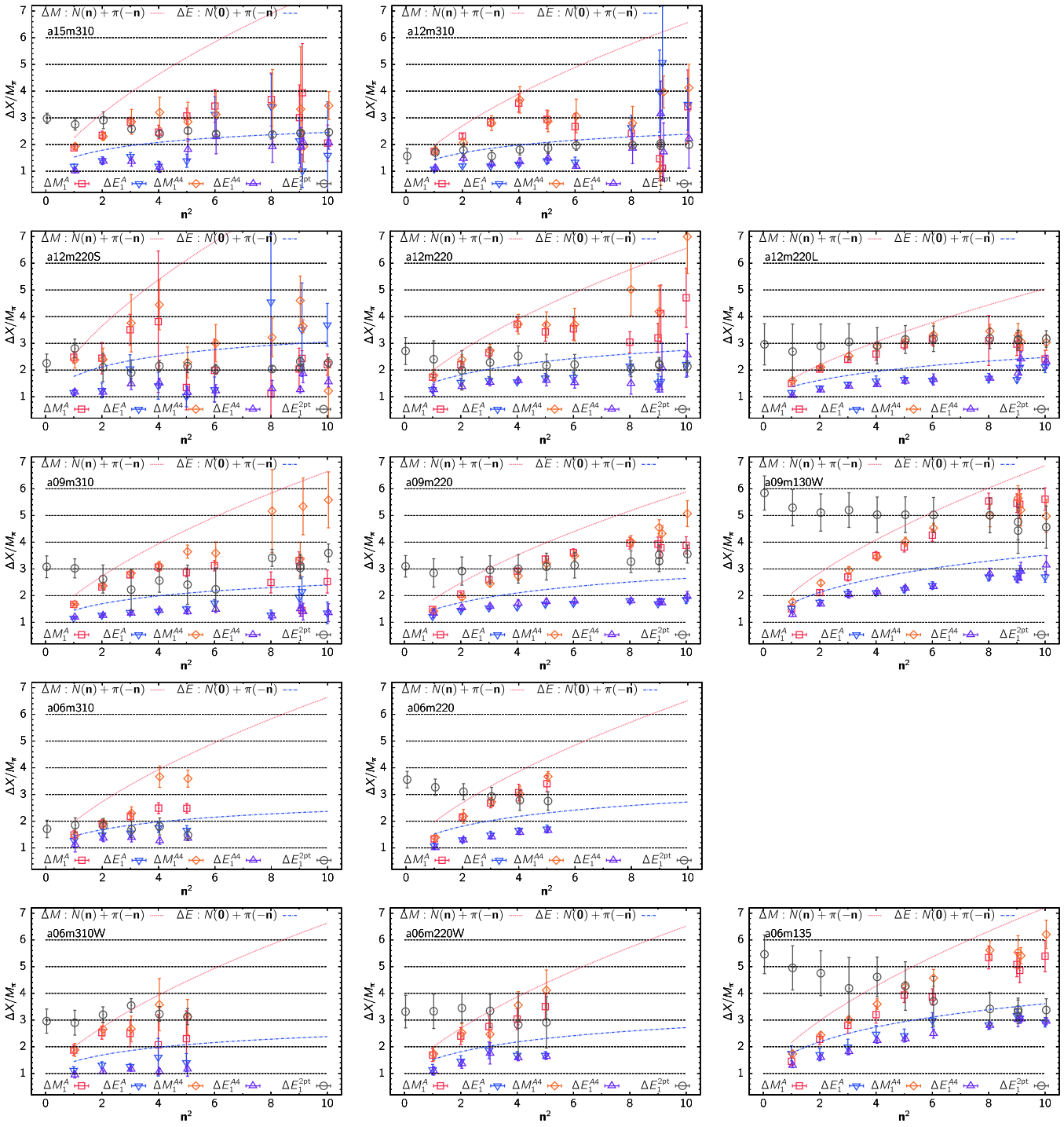

FIG. 6. Results for the energy (mass) gaps ΔE_1 (ΔM_1) for the first excited state extracted from (i) simultaneous fits to axial three-point correlators $C[A_\mu]$ and the pseudoscalar correlator C_P ($\mathcal{S}_{\rm sim}$ strategy and labeled ΔE_1^A and ΔM_1^A), and (ii) from fits to the $C[A_4]$ correlator ($\mathcal{S}_{A4}$ strategy and labeled ΔE_1^{A4} and ΔM_1^{A4}). These mass gaps are compared with the first excited state energy $\Delta E_1^{2\rm pt}$ from four-state fits to the nucleon two-point correlator. Note that the difference between them (black circles versus blue triangles), and consequently the difference between the form factors extracted, increases as $M_\pi \to 135$ MeV and $\mathbf{n}^2 \to 0$ (equivalently $Q^2 \to 0$).

and $M_\pi \to 0$. This behavior is consistent with $\Delta E_1^{2\rm pt}$ corresponding to a mixture of radial and higher multiparticle excitation whereas the energy of the intermediate excited states identified by the $\mathcal{S}_{A4}$ and $\mathcal{S}_{\rm sim}$ fits, $N(\boldsymbol{n}) + \pi(-\boldsymbol{n})$ and $N(\mathbf{0}) + \pi(-\boldsymbol{n})$, decreases with decreasing $\boldsymbol{n}$ and M_π. A word of caution when making these identifications: it is very important to qualify that the ΔE_1 and ΔM_1 from the two-state fits in $\mathcal{S}_{A4}$ and $\mathcal{S}_{\rm sim}$ strategies

are effectively trying to account for all the intermediate states that make significant contributions and not just the lowest or the most intuitive ones. Given the size of the effect, identifying and improving control over all the excited states that make significant contribution to these correlation functions will be key to obtaining, in the future, higher precision results for the form factors.

E. Renormalization constant Z_A

The renormalization constant Z_A for the axial current needed for the form factors G_A and $\tilde{G}_P$ and the charges g_A, g_P^* and $g_{\pi NN}$ was determined nonperturbatively using the RI-sMOM intermediate scheme in Ref. [13]. We use the results given in Table V there.

III. PARAMETERIZATION OF $G_A(Q^2)$, AND THE EXTRACTION OF g_A AND $\langle r_A^2 \rangle$

In this section, we present the analysis of $G_A(Q^2)$ without including the values of the axial charge g_A obtained from the forward matrix element. Its extraction is discussed separately in Sec. V. This is done to keep the two extractions of g_A—from the forward matrix element (50) and by extrapolating $G_A(Q^2)$ to $Q^2 \to 0$ [Eq. (36)]—separate. The final result, given in Table VI, is taken to be the average of the two.

The axial-vector form factor $G_A(Q^2)$ can be parametrized, near $Q^2 = 0$, by the axial charge g_A and the axial charge radius squared $\langle r_A^2 \rangle$:

$$G_A(Q^2) = g_A\left(1 - \frac{\langle r_A^2\rangle}{6}Q^2 + \cdots\right), \tag{24}$$

where $g_A \equiv G_A(0)$ and

$$\langle r_A^2\rangle \equiv -\frac{6}{g_A}\frac{dG_A(Q^2)}{dQ^2}\bigg|_{Q^2=0}. \tag{25}$$

To extract these from lattice data obtained at $Q^2 \gtrsim 0.1$ GeV^2, one parametrizes the Q^2 dependence of $G_A(Q^2)$. Among the various parametrizations, we study the dipole ansatz and the model-independent z-expansion. The dipole ansatz

$$G_A(Q^2) = \frac{g_A}{(1 + Q^2/\mathcal{M}_A^2)^2}. \tag{26}$$

has two free parameters, the axial charge g_A and the axial mass $\mathcal{M}_A$. The z-expansion is the series

$$G_A(Q^2) = \sum_{k=0}^{\infty} a_k z^k, \tag{27}$$

in terms of the variable

$$z = \frac{\sqrt{t_c + Q^2} - \sqrt{t_c + t_0}}{\sqrt{t_c + Q^2} + \sqrt{t_c + t_0}} \quad \text{with} \quad t_c \equiv 9M_\pi^2 \tag{28}$$

that maps the kinematically allowed analytical region $Q^2 \geq 0$ to that within a unit circle, $|z| < 1$ [18]. The parameter t_0 is discussed later. For sufficiently small z, fits with the first few terms should suffice. In practice, to stabilize the fits we impose the condition $|a_k| \leq 5$ for all $z^{k\geq 1}$ truncations [18]. With increasingly precise data over a sufficiently large range of Q^2, our goal is to demonstrate that a data-driven choice can be made between the various parametrizations.

In the data presented here, the statistical signal is good for momentum transfer with $\boldsymbol{n}^2 \leq 6$ but often poor in the four points with $8 \leq \boldsymbol{n}^2 \leq 10$. To test the stability of the dipole and z^k fits with such few points, we compare the output of the fits to the lowest six versus all ten Q^2 points on nine ensembles where data on all ten Q^2 values exist. Observing consistency, the final results are taken from fits to six (five in 4 cases) points, i.e., to data up to the $Q^2|^{n^2\leq 6}_{\rm max}$ given in Table I. This implies that results for form factors presented for $Q^2 \gtrsim 0.5$ GeV^2 come mainly from the $M_\pi \sim 310$ MeV ensembles, and, *a priori*, could have an large systematic uncertainty. In practice, however, the observed weak dependence of form factors on M_π (see Fig. 2 and similar results from a clover-on-clover calculation presented in Ref. [7]) suggests that the uncertainty is likely within the quoted errors. Readers should, nevertheless, keep in mind that results at $Q^2 \gtrsim 0.5$ GeV^2 are based mainly on data from the $M_\pi \approx 310$ MeV ensembles.

Estimates of G_A from the dipole fit to data from the three ESC strategies are consistent, however, on six ensembles these dipole fits to $\mathcal{S}_{\rm sim}$ and $\mathcal{S}_{A4}$ data have poor p-values. Our evaluation of the failure is that the dipole ansatz does not have enough parameters to capture the change in the curvature over the range of Q^2 studied. A consequence is that estimates for g_A and $\langle r_A^2\rangle$ are smaller than those from z^2 fits to the same $\mathcal{S}_{\rm sim}$ and $\mathcal{S}_{A4}$ data. Since agreement with PCAC is essential and $\mathcal{S}_{\rm sim}$ data do the best job, while the dipole fits are poor, we rule out the dipole ansatz. Henceforth, our final results are obtained using the z-expansion, and the dipole results are given only for comparison.

In the z-expansion fits, the free parameter t_0 in Eq. (28) is used to adjust the maximum value of z within the unit circle $|z| \leq 1$. We take $t_0 = 0.4$, 0.2, 0.12 for $M_\pi \approx 310$, 220, 130 MeV ensembles, which gives $|z| \lesssim 0.2$. We have checked that using $t_0 = 0$ does not change the fits or the values significantly.

To ensure that the form factors satisfy the expected $1/Q^4$ perturbative behavior in the limit $Q^2 \to \infty$, sum rules can be imposed as was done in Ref. [9]. However, to obtain the behavior near $Q^2 = 0$ from six or ten data points with $Q^2_{\rm max} \approx 1$ GeV^2, we choose to make fits without the sum rules [19], i.e., to not increase the weight of the larger error high Q^2 points by imposing the sum rules. The z^1 and z^2 fits to $G_A(Q^2)$ from the $\mathcal{S}_{\rm sim}$ strategy are shown in Fig. 13. The resulting bare axial charge $g_A \equiv G_A(0)$ and the charge radius squared $\langle r_A^2\rangle$ from the z^2 fits are shown in Fig. 7,

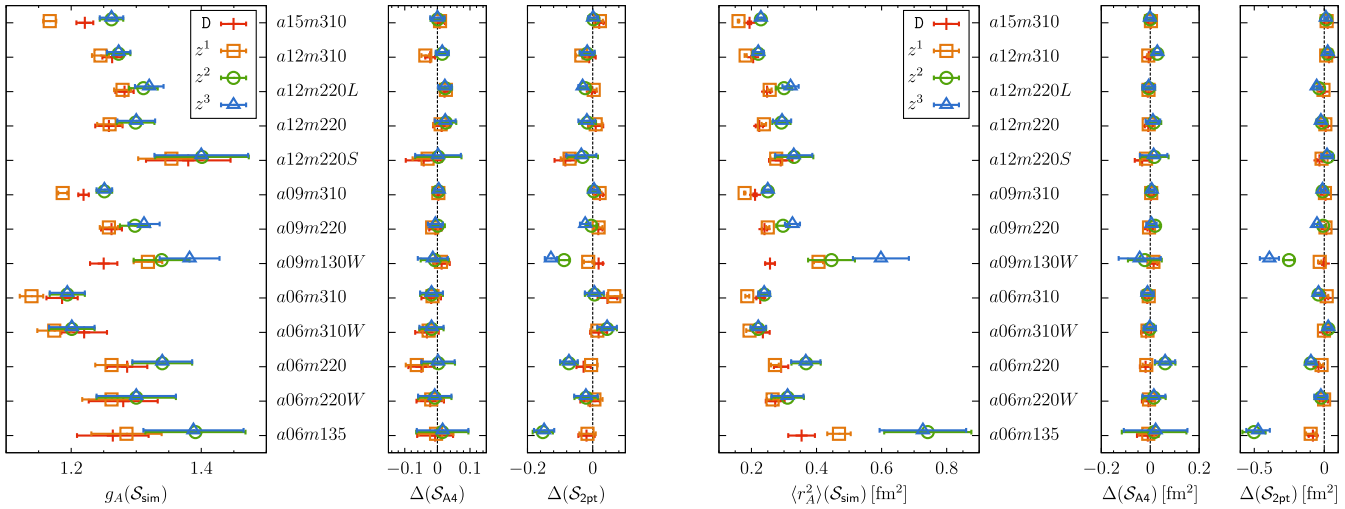

FIG. 7. Left: results for bare g_A from the strategy $\mathcal{S}_{\rm sim}$ and the differences $\Delta(S_{A4}) = g_A|_{\mathcal{S}_{A4}} - g_A|_{\mathcal{S}_{\rm sim}}$ and $\Delta(\mathcal{S}_{2pt}) = g_A|_{\mathcal{S}_{2pt}} - g_A|_{\mathcal{S}_{\rm sim}}$. To facilitate visualization of the spread, the errors plotted for $\Delta(X)$ are those in $g_A(X)$. Results are shown for the dipole fit labeled "D" and $z^{1,2,3}$-truncations. Right: analogous results for $\langle r_A^2\rangle$.

and the data are summarized in Table XXIII in Appendix D. From these data and the z-expansion fits, we conclude the following:

(i) There is agreement in results between z^2 and z^3 fits in all cases. To account for the small curvature observed in the data shown in Fig. 13 and yet avoid overparametrization, evaluated using the Akaika information criteria (AIC) [20], we will present final results with the z^2 truncation.

(ii) The errors in the data from the two physical mass ensembles $a09m130W$ and especially $a06m135$ are large and underscore the need for higher statistics.

(iii) Results for both g_A and $\langle r_A^2\rangle$ from the $\mathcal{S}_{A4}$ and $\mathcal{S}_{\rm sim}$ analyses overlap and increase in value as $M_\pi \to 135$ MeV. This increase is correlated with the increasing ESC of the $N\pi$ state.

We take the final results from the $\mathcal{S}_{\rm sim}$ strategy in which a simultaneous fit is made to all five correlators and the form factors come closest to satisfying the PCAC relation as shown in Fig. 3. This is a 2-state fit and we find that stable 3-state fits require higher statistics. Thus, with the current data, we do not have a reliable way of estimating the systematic uncertainty associated with possible residual ESC.

The analysis of g_A obtained from the forward matrix elements is postponed to Sec. V.

A. Extrapolation of g_A and $\langle r_A^2\rangle$ to the physical point

Extrapolation of the renormalized axial charge g_A and the axial charge radius squared $\langle r_A^2\rangle$ to the physical point ($a \to 0$, $M_\pi \to 135$ MeV, $L \to \infty$) is performed using a simultaneous CCFV fit keeping only the lowest order corrections in the ansatz

$$Y = b_0^Y + b_1^Y a + b_2^Y M_\pi^2 + b_3^Y M_\pi^2 \exp(-M_\pi L), \qquad (29)$$

where $Y = \langle r_A^2\rangle$ or g_A and $\{b_i^Y\}$ denote the corresponding set of fit parameters. The discretization artifacts are taken to start at $O(a)$ since the clover action used is only tadpole improved and the axial and pseudoscalar currents are unimproved [21]. Similarly, only the lowest order term in the chiral expansion is kept to avoid over-parametrization as data at only three values of the pion mass have been simulated.

We have performed four CCFV fits to (i) the full set of thirteen ensembles (13-pt); and three "12-pt" fits that exclude (ii) the coarsest lattice point $a15m310$, (iii) the smallest volume point $a12m220S$ that also has large errors, and (iv) the point $a06m135$ that has large statistical errors and shows the largest difference from the other 12 points. The three 12-pt fits are used to estimate systematics due to discretization and finite volume effects, and the impact of the $a06m135$ point. Results of the 13-point CCFV extrapolation for g_A and $\langle r_A^2\rangle$ are summarized in Table III for six

TABLE III. g_A and $\langle r_A^2\rangle$ from the 13-point CCFV fit. Results are given for the z^2 and dipole fits to $G_A(Q^2 \neq 0)$, and for the three strategies used to control ESC. In each case, in addition to the central value and the total analysis error, the two systematic errors are the difference between the z^2 and z^3 estimates, and the difference from the 12-pt CCFV fits explained in the Sec. III A.

g_A	z^2	Dipole
$\mathcal{S}_{\rm sim}$	1.296(50)(13)(11)	1.239(43)(···)(39)
$\mathcal{S}_{A4}$	1.281(51)(11)(21)	1.204(44)(···)(21)
$\mathcal{S}_{2pt}$	1.213(39)(02)(···)	1.228(37)(···)(···)

$\langle r_A^2\rangle$	z^2	Dipole
$\mathcal{S}_{\rm sim}$	0.418(33)(29)(18)	0.305(13)(···)(06)
$\mathcal{S}_{A4}$	0.428(31)(21)(19)	0.305(15)(···)(06)
$\mathcal{S}_{2pt}$	0.282(27)(16)(···)	0.275(14)(···)(···)

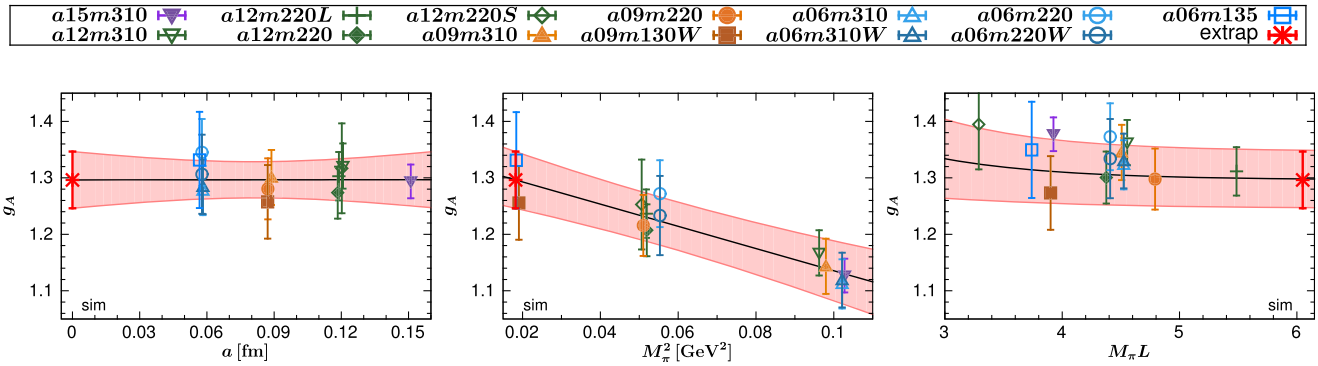

FIG. 8. The axial charge g_A given by the 13-pt CCFV fit to $\mathcal{S}_{\rm sim}$ data using the z^2 fit to $G_A(Q^2 \neq 0)$. The pink band in each panel gives the result of the CCFV fit [Eq. (29)] versus the x-axis variable with the other two variables set to their physical values. The data points in each panel have been shifted in the other two variables using the same CCFV fit, however, the size of errors are not changed. The final result at the physical point is shown by the red cross.

cases: the three strategies used for removing ESC, $\mathcal{S}_{\rm sim}$, $\mathcal{S}_{A4}$, and $\mathcal{S}_{2\rm pt}$, and the two Q^2 parametrizations, z^2 and dipole. The parameters of the 13-point CCFV extrapolation of the z^2 fit to the $\mathcal{S}_{\rm sim}$ data, used to get the final central values, are given in Table XXVI in Appendix E for both g_A and $\langle r_A^2 \rangle$. Results for all the other cases can be constructed using the data for the form factors given in Tables X–XXII in Appendix C.

1. g_A

The result for g_A, taken from the 13-point CCFV extrapolation of z^2 fits to the $\mathcal{S}_{\rm sim}$ data, shown in Fig. 8, is

$$g_A = 1.296(50)_{\rm stat}(13)(11) = 1.296(50)_{\rm stat}(17)_{\rm sys}, \quad [z^2]. \tag{30}$$

The first error is the total analysis uncertainty given by the overall bootstrap process, and the next two are additional systematic uncertainties: (i) the difference between using z^2 and z^3 fits and (ii) the difference of this central value from the average of the three 12-point CCFV fits. The two systematics are added in quadrature to get the total systematic error given in the second line in Eq. (30). In Sec. V, this result is compared with an independent analysis of g_A obtained from the forward matrix element, i.e., from the zero momentum correlator, $C_{A_3}(\boldsymbol{p} = \boldsymbol{0})$, as defined in Eq. (7).

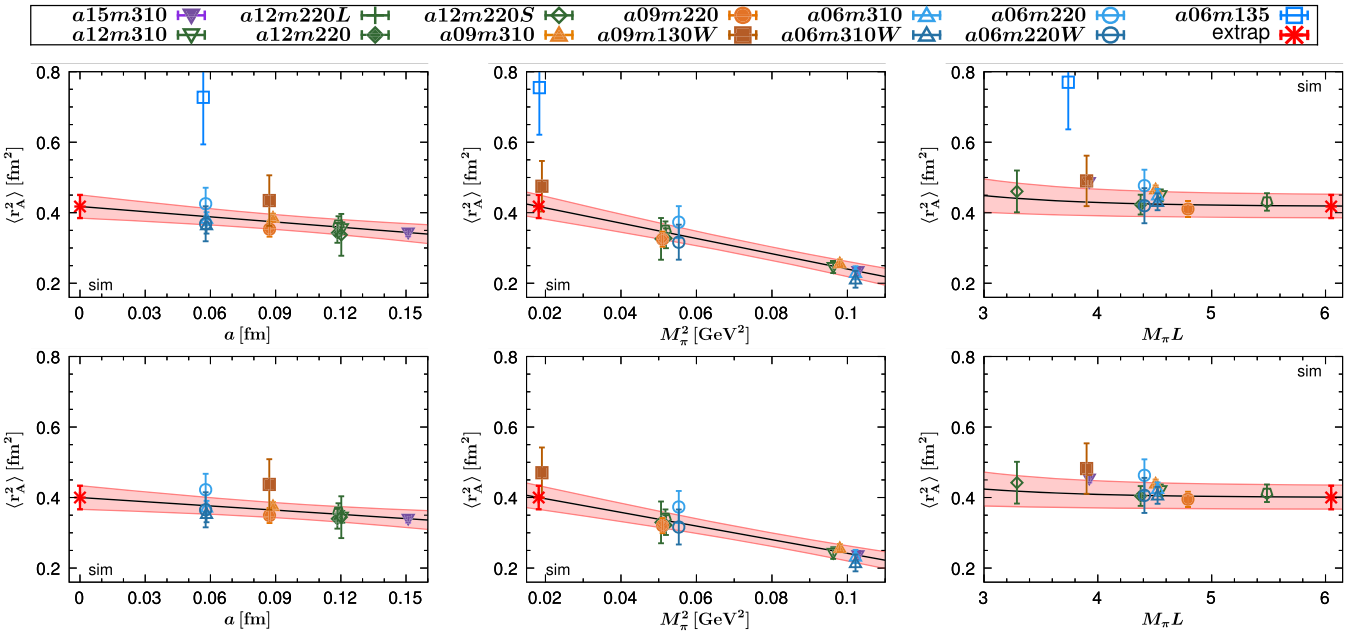

FIG. 9. Top: the axial charge radius squared $\langle r_A^2 \rangle$ given by the 13-pt CCFV fit to data obtained using the z^2 fit to $G_A(Q^2 \neq 0)$ with the $\mathcal{S}_{\rm sim}$ strategy. Bottom: the 12-pt fit without the $a06m135$ point (open blue square in the three panels on the top) that has large errors. The pink band in each panel gives the result of the CCFV fit [Eq. (29)] versus the x-axis variable with the other two variables set to their physical values. The data points in each panel have been shifted using the same CCFV fit, however, the size of errors are not changed. The final result at the physical point is shown by the red cross.

2. $\langle r_A^2 \rangle$

The CCFV fit to $\langle r_A^2 \rangle$, obtained from the $\mathcal{S}_{\rm sim}$ data with z^2 fit, is shown in Fig. 9 (top panels). It gives

$$\begin{aligned}\langle r_A^2 \rangle &= 0.418(33)_{\rm stat}(29)(18)\ {\rm fm}^2 \\ &= 0.418(33)_{\rm stat}(34)_{\rm sys}{\rm fm}^2, \qquad [z^2] \qquad (31)\end{aligned}$$

with the errors derived in the same way as for g_A.

For both g_A and $\langle r_A^2 \rangle$, the largest dependence in the CCFV fit is on M_π^2 for the $\mathcal{S}_{\rm sim}$ and $\mathcal{S}_{A4}$ strategies. This is a consequence of the increasing influence of the $N\pi$ state as its mass gap decreases well below the N(1440) as $M_\pi \to 135$ MeV. In contrast, the $\mathcal{S}_{\rm 2pt}$ data, which do not include the $N\pi$ state in the analysis, show mild dependence on all three variables $\{a, M_\pi, M_\pi L\}$.

Estimates from the 12-pt CCFV fit excluding the $a06m135$ point, shown in the bottom panels of Fig. 9, are consistent with the 13-point results. This is expected since the errors in the $a06m135$ point are large. Clearly, to further improve the estimates of both g_A and $\langle r_A^2 \rangle$ requires much higher statistics data at small Q^2 on the physical pion-mass ensembles.

B. $G_A(Q^2)$ at the physical point

The Q^2 dependence of the axial form factor up to 1 GeV^2, obtained at the physical point, is shown in Fig. 10 for the three strategies $\mathcal{S}_{\rm 2pt}$, $\mathcal{S}_{A4}$, and $\mathcal{S}_{\rm sim}$. The pink band in these figures was obtained using the following three step process starting with the renormalized lattice data for $G_A(Q^2)/g_A$, which on each of the thirteen ensembles are at different discrete values of Q^2. First the data on each ensemble were fit using the z^2-ansatz [see Eq. (27)] and the result is taken to specify $G_A(Q^2)/g_A$ for $0 < Q^2 \le 1$ GeV^2. Second, we chose a set of eleven Q^2 values evenly distributed over this range, and for the thirteen data points at each of these Q^2 values carry out a 13-point CCFV extrapolation using Eq. (29). The result was taken to be the physical point value of G_A/g_A at that Q^2. In each of these CCFV fits, the thirteen points from the thirteen ensembles are uncorrelated as these are independent calculations. Lastly, these eleven extrapolated points were fit by the z^2 ansatz to obtain the final parametrization valid in the interval $0 \le Q^2 \le 1.0$ GeV^2 and shown by the pink band in Fig. 10. The errors in the original lattice data were fully propagated through this three step process carried out within a single bootstrap setup. This gives the central value and error. Possible uncertainty due to incomplete removal of ESC or due to using only the leading order CCFV fit ansatz is to be estimated separately.

Figure 10 also shows the experimental bubble chamber data and the dipole ansatz with $M_A = 1.026(21)$ GeV extracted from it (green band) [17]. A recent z-expansion analysis of the ν-deuterium data [22] finds a ≈10X larger uncertainty. In our analysis, only the $\mathcal{S}_{\rm 2pt}$ data are roughly consistent with a dipole ansatz with $M_A \approx 1.30$ GeV,

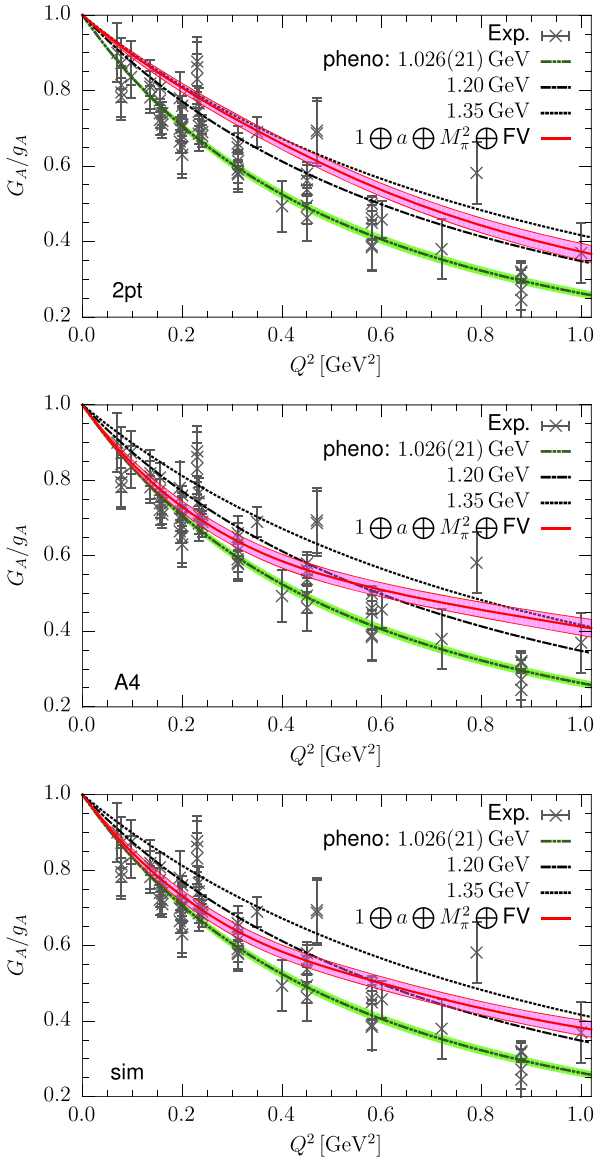

FIG. 10. Results for G_A/g_A at the physical point for the three strategies $\mathcal{S}_{\rm 2pt}$, $\mathcal{S}_{A4}$ and $\mathcal{S}_{\rm sim}$ (labeled "2pt," "A4," and "sim," respectively) used to control the excited-state contamination. The three step process used to get these results shown by the pink band is described in the text. In each case, the error band represents the full analysis error for that strategy but with the value at $Q^2 = 0$ fixed to unity. The label $1 \oplus a \oplus M_\pi^2 \oplus FV$ specifies that all 4 terms in the CCFV ansatz, Eq. (29), were kept. The experimental ν-deuterium data (gray crosses labeled Exp.) were provided by Ulf Meissner and the dipole result $M_A = 1.026(21)$ GeV is taken from Ref. [17]. This and the two other dipole fit with $M_A = 1.20$ and 1.35 GeV are shown only for comparison.

however, the three form factors extracted using $\mathcal{S}_{\rm 2pt}$ fail to satisfy the PCAC relation. We, therefore, reemphasize that the dipole curves with $M_A = 1.026$, 1.2 and 1.35 GeV are shown only for comparison.

The data from the $\mathcal{S}_{A4}$ and $\mathcal{S}_{\rm sim}$ strategies are consistent, and show a more rapid fall until $Q^2 \approx 0.3$ GeV^2, and give

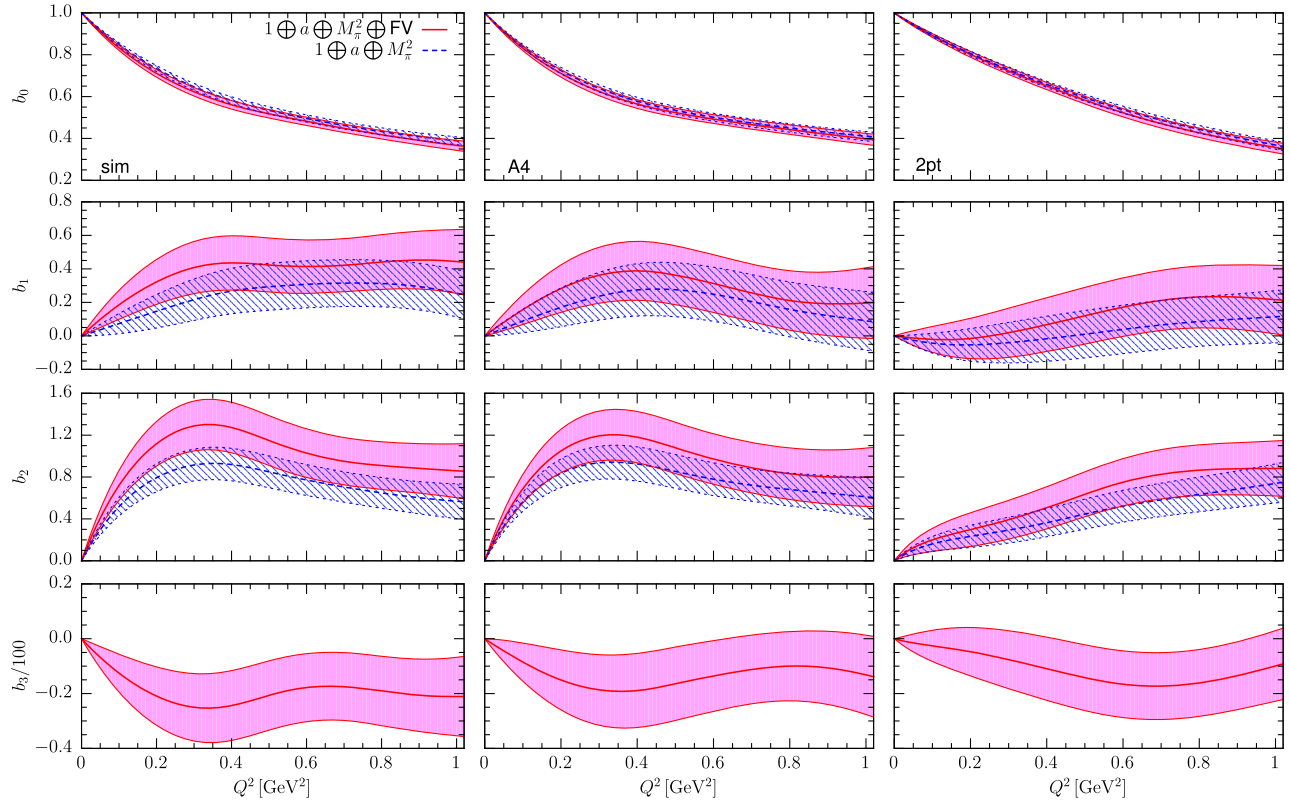

FIG. 11. The fit coefficients b_i, $i = 0, 1, 2, 3$, defined in Eq. (29), for the CCFV extrapolation of the axial form factor $G_A(Q^2)/g_A$ obtained with strategy $\mathcal{S}_{\rm sim}$ (left), $\mathcal{S}_{A4}$ (middle) and $\mathcal{S}_{\rm 2pt}$ (right) and fit with the z^2 truncation. The extrapolated $G_A(Q^2)/g_A$ with $\mathcal{S}_{\rm sim}$ is shown in Fig. 10. The hatched blue curves correspond to $b_{0,1,2}$ obtained neglecting the finite-volume term in the analysis.

results roughly consistent with the dipole values $M_A = 1.026(21)$ GeV [and $\langle r_A^2 \rangle = 0.444(28)$ fm^2)] in Ref. [17]. They then level out falling more slowly, however, note that for $Q^2 > 0.5$ GeV^2 our results are mainly from the heavier $M_\pi \approx 310$ MeV ensembles. On the heavier M_π ensembles, the mass gaps in the $N\pi$ analyses (blue triangles and red squares in Fig. 6) increase rapidly towards those from the $\mathcal{S}_{\rm 2pt}$ fit (black circles). Consequently, as shown in Fig. 10, the G_A/g_A from the $\mathcal{S}_{\rm sim}$ analysis moves towards the $\mathcal{S}_{\rm 2pt}$ result for $Q^2 \gtrsim 0{:}5$ GeV^2.

To obtain data for $Q^2 > 0.5$ GeV^2 on physical pion mass ensembles with $M_\pi L > 4$ requires simulations at much larger values of $\mathbf{q}$ where statistical and discretization errors are large with the methodology used in this work. A more promising method for generating data at large Q^2 is momentum smearing [23]. Also, when including points with larger Q^2, the z-expansion fits with and without sum-rules should be compared since it is not known, *a priori*, when the expected $1/Q^4$ asymptotic behavior becomes significant. Alternately, as shown in Ref. [7], one can analyze the data using a Padé parametrization. Our fits to the final G_A using the Padé ansatz $g_A/(1 + b_1 Q^2 + b_2 Q^4)$, which has the $1/Q^4$ behavior built in, gave estimates consistent with Eqs. (30) and (31).

The coefficients b_i in the CCFV fit using Eq. (29) are shown in Fig. 11 for the three strategies $\mathcal{S}_{\rm 2pt}$, $\mathcal{S}_{A4}$, and $\mathcal{S}_{\rm sim}$. The coefficients $b_1(Q^2)$ and $b_2(Q^2)$ are similar within errors for $\mathcal{S}_{\rm sim}$ and $\mathcal{S}_{A4}$, significantly different from zero, and qualitatively different from the case $\mathcal{S}_{\rm 2pt}$. The b_i for $\mathcal{S}_{\rm sim}$ and $\mathcal{S}_{A4}$ show a change in behavior at $Q^2 \approx 0.3$ GeV^2, coincident with the region where the curvature in G_A changes as shown in Fig. 10. This could be due to the fact that most of the raw data controlling the parametrization at $Q^2 \gtrsim 0.3$ GeV^2 comes from the $M_\pi \approx 220$ and 310 MeV ensembles. On the other hand, support for the parametrization comes from the observation that the data, plotted in Fig. 2, do not show a significant variation versus $\{a, M_\pi\}$. Cutting out the data with $Q^2 > 0.3$ GeV^2 to see if fits change, unfortunately eliminates most of the $M_\pi \approx 220$ and 310 MeV ensembles—they do not have enough points to perform even a z^2 fit. We are, therefore, not able to resolve the reason for the change in parametrization around $Q^2 \approx 0.3$ GeV^2.

To provide our best parametrization of $G_A(Q^2)$ for phenomenology, we repeated the above 3-step procedure using the $\mathcal{S}_{\rm sim}$ strategy data. Again, the data after extrapolation to the continuum limit (at $Q^2 = 0, 0.1, 0.2, \ldots, 1.0$ GeV^2) were fit with a z^2 ansatz, $t_c = 9M_\pi^2$ with $M_\pi = 135$ MeV, and $t_0 = 0.25$ GeV^2. The result, shown in Fig. 12, has the parametrization

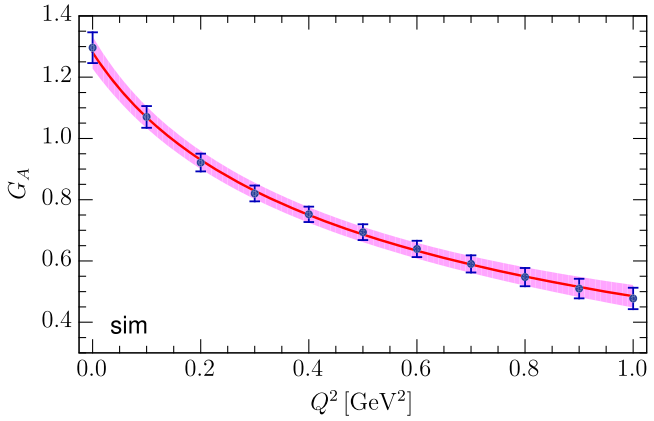

FIG. 12. The final estimate of $G_A(Q^2)$ at the physical point. The eleven fiducial points used to make the fit are shown in blue and their errors are obtained from the one overall bootstrap analysis covering the three step process described in the text. The parametrization versus z is given in Eq. (32).

$$G_A(Q^2) = a_0 + a_1 z + a_2 z^2 = 0.876(28) - 1.669(99)z + 0.483(498)z^2, \quad (32)$$

with the correlation matrix:

$$\begin{array}{c} \\ a_0 \\ a_1 \\ a_2 \end{array} \begin{array}{c} \begin{array}{ccc} a_0 & a_1 & a_2 \end{array} \\ \begin{pmatrix} 1.0 & -0.45170 & -0.02966 \\ -0.45170 & 1.0 & -0.24394 \\ -0.02966 & -0.24394 & 1.0 \end{pmatrix} \end{array} \quad (33)$$

This fit gives

$$g_A = 1.281(53), \quad \langle r_A^2 \rangle = 0.498(56)\ \text{fm}^2, \quad (34)$$

which are consistent with the estimates in Eqs. (30) and (31), *albeit* with a $\langle r_A^2 \rangle$ larger by roughly 1σ.

We also carried out this final z^2 fit setting $t_0 = 0$ in the definition of z. The results are

$$g_A = 1.282(54), \quad \langle r_A^2 \rangle = 0.505(66)\ \text{fm}^2. \quad (35)$$

While consistent, the coefficient c_2 in this fit is essentially undetermined. We, therefore, choose the results given in Eq. (34).

For our final results from the analysis of G_A, we take the average weighted by the "stat" errors of values given in Eqs. (30), (31), and (34) to get

$$g_A = 1.289(53)_{\text{stat}}(17)_{\text{sys}}, \quad \langle r_A^2 \rangle = 0.439(56)_{\text{stat}}(34)_{\text{sys}}\ \text{fm}^2. \quad (36)$$

For errors, we take the larger of the "stat" error and keep the "sys" errors given in Eqs. (30) and (31).

We now return to two related issues that arise because the majority of the data used to get the parametrization in Eq. (32) are at $Q^2 \lesssim 0.5$ GeV^2 as shown in Fig. 1. The first is whether this parametrization is compatible with $G_A(Q^2 = \infty) = 0$ since the sum rule constraints needed to build in the perturbative $1/Q^4$ behavior have not been imposed? And the second is—how reliable is this G_A for $Q^2 > 0.5$ GeV^2 since most of the data in this region are from the $M_\pi \approx 310$ MeV ensembles? Regarding the first issue, the parametrization in Eq. (32) at $z = 1$ ($\Rightarrow Q^2 = \infty$) gives

$$G_A = -0.31(48), \quad \frac{dG_A(z)}{dz} = -0.70(98). \quad (37)$$

These are consistent with zero within one sigma. For the second issue, data in Fig. 2 show that $G_A(Q^2)$ extracted on 12 ensembles show little dependence on $\{a, M_\pi\}$. The one exception, $a06m135$, where the data lie about one sigma lower, has already been identified as statistics limited. As stated before, if future data continue to show little dependence on a and M_π, then even data from the $M_\pi \approx 310$ MeV ensembles would provide a good approximation to the continuum G_A and increase confidence in the result for $Q^2 > 0.5$ GeV^2.

Lastly, we made a z^2 fit to the same continuum extrapolated data but imposed a prior, $G_A(Q^2 = \infty) = 0$ with width 0.3 based on the value in Eq. (37). The result is

$$G_A(Q^2) = 0.872(28) - 1.705(109)z + 0.767(102)z^2, \quad (38)$$

with $G_A = -0.07(10)$ and $dG_A/dz = -0.17(17)$ at $z = 1$. The main difference from the result in Eq. (32) is the tightening of the estimate of the z^2 term. Overall, in all these fits, the coefficients a_0 and a_1, defined in Eq. (32) are stable, whereas higher precision data are needed to improve a_2.

IV. COUPLINGS g_P^* AND $g_{\pi NN}$ FROM THE INDUCED PSEUDOSCALAR FORM FACTOR

The induced pseudoscalar coupling g_P^* is defined as

$$g_P^* \equiv \frac{m_\mu}{2M_N} \tilde{G}_P(Q^{*2}), \quad (39)$$

where m_μ is the muon mass and $Q^{*2} = 0.88 m_\mu^2$ is the energy scale of muon capture. Similarly, the pion-nucleon coupling $g_{\pi NN}$ is obtained from the residue of $\tilde{G}_P(Q^2)$ at the pion pole, i.e., through the relation

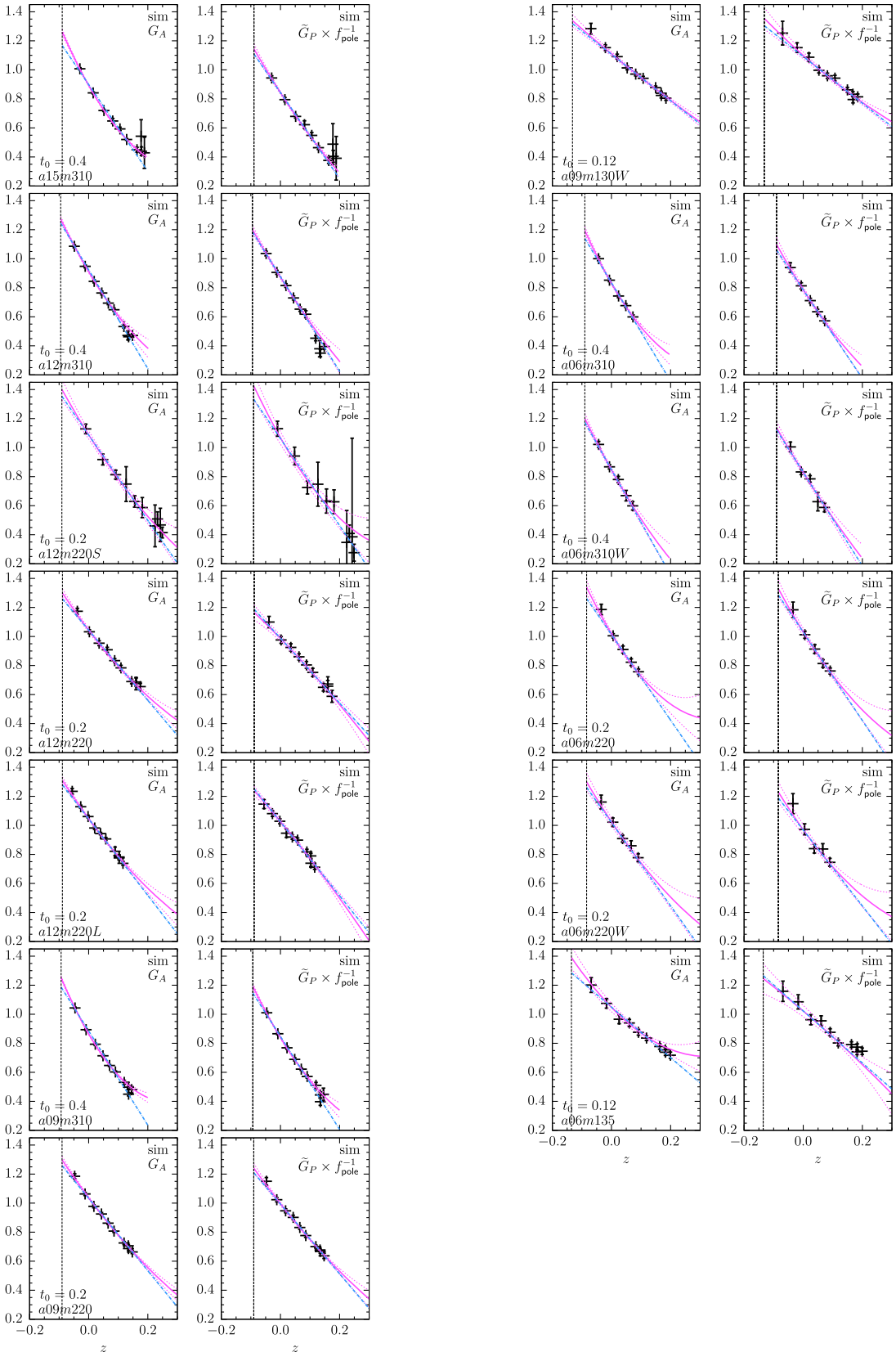

FIG. 13. Comparison of G_A and $\tilde{F}_P \equiv \tilde{G}_P \times f_{\text{pole}}^{-1}$ from strategy $\mathcal{S}_{\text{sim}}$ for $a \approx 0.15, 0.120.09, 0.06$ fm lattices. The z^2 (magenta lines with error band) is compared to the z^1 fit (blue dash dot). The four largest z points are excluded from the fits to the $M_\pi \approx 310$ MeV and $a12m220S$ data. The vertical black dotted line corresponds to $Q^2 = 0$. The value of t_0 and ensemble name are given in the labels.

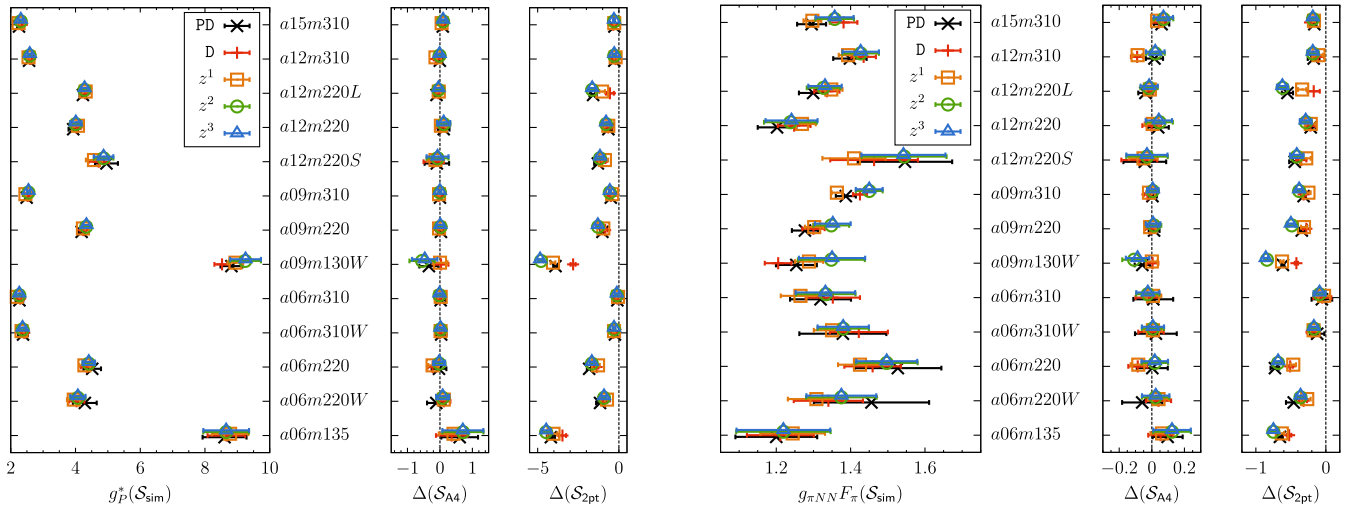

FIG. 14. Left: results for the bare g_P^* from the strategy $\mathcal{S}_{\rm sim}$ and the differences $\Delta(X) = g_P^*(X) - g_P^*(\mathcal{S}_{\rm sim})$. To facilitate visualization of the spread, the errors plotted for $\Delta(X)$ are those in $g_P^*(X)$. The fits used to parametrize the Q^2 behavior are labeled "PD" defined in Eq. (42); "D" for the dipole fit, and z^k for various truncations of the z-expansion. Right: results for bare values of $g_{\pi NN}F_\pi$ obtained with the strategy $\mathcal{S}_{\rm sim}$ and the differences $\Delta(X) = g_{\pi NN}F_\pi(X) - g_{\pi NN}F_\pi(\mathcal{S}_{\rm sim})$.

$$g_{\pi NN} \equiv \lim_{Q^2\to -M_\pi^2} \frac{M_\pi^2+Q^2}{4M_N F_\pi}\tilde{G}_P(Q^2) = \frac{\tilde{F}_P(-M_\pi^2)M_N}{F_\pi}, \tag{40}$$

where $F_\pi = 92.9$ MeV is the pion decay constant. The function $\tilde{F}_P$ defined as

$$\tilde{F}_P(Q^2) \equiv \frac{Q^2+M_\pi^2}{4M_N^2}\tilde{G}_P(Q^2). \tag{41}$$

is $\tilde{G}_P$ without the pion pole and should equal G_A if PPD were exact. This requires $R_3 \equiv \tilde{F}_P/G_A$, plotted in Fig. 4, to be unity. Deviations for $\mathcal{S}_{2pt}$ are significant, while those for $\mathcal{S}_{\rm sim}$ and $\mathcal{S}_{A4}$ are one within the size of discretization errors and/or violations of PPD expected.

To extract g_P^* and $g_{\pi NN}$ from the lattice data, a parametrization of the Q^2 behavior of $\tilde{G}_P$ and $\tilde{F}_P$ was carried out. A comparison of the z^1 and z^2 fits to G_A and $\tilde{F}_P$ from the $\mathcal{S}_{\rm sim}$ strategy is shown in Fig. 13 for the thirteen ensembles. Results from z^2 and z^3 fits are consistent, indicating convergence, while z^1 fits miss the small curvature seen. To avoid over parametrization, we again take the z^2 results as the central values.

A. Parametrization of $\tilde{G}_P(Q^2)$ and $\tilde{F}_P$

Based on the analysis of PCAC (see Fig. 3), we focus on the $\tilde{G}_P(Q^2)$ data from the $\mathcal{S}_{\rm sim}$ and $\mathcal{S}_{A4}$ strategies and again give the $\mathcal{S}_{2pt}$ results only for comparison.

We consider two ways to parametrize $\tilde{G}_P(Q^2)$, both of which build in the pion-pole dominance hypothesis. The first is the expansion

$$\tilde{G}_P(Q^2) = \frac{c_0}{Q^2+M_\pi^2} + c_1 + c_2 Q^2, \tag{42}$$

where the c_i $(i = 0, 1, 2)$ are fit parameters, and we have kept as many terms in the polynomial as can be resolved by the data. Results for g_P^*, $g_{\pi NN}F_\pi$ and $g_{\pi NN}F_\pi/M_N$ using this fit (labeled PD) to the $\mathcal{S}_{\rm sim}$ data are given in Table XXIV along with the χ^2/d.o.f. and p-value for the fits.

In the second way, we treat $\tilde{F}_P(Q^2)$ as an analytic function that can be fit using either the dipole ansatz (with free parameters $\tilde{F}_P(0)$ and $\tilde{\mathcal{M}}_P$) or the z-expansion, Eq. (27), with z again defined by Eq. (28). Results for g_P^*, $g_{\pi NN}F_\pi$ and $g_{\pi NN}F_\pi/M_N$, from z^2 fits to $\tilde{F}_P(Q^2)$ obtained with the $\mathcal{S}_{\rm sim}$ strategy are given in Table XXV and agree with those in Table XXIV.

Results for the bare g_P^* from the $\mathcal{S}_{\rm sim}$ strategy for five Q^2 parametrizations of $\tilde{G}_P$ are shown in Fig. 14 (left) along with their differences from results obtained using the $\mathcal{S}_{A4}$ and $\mathcal{S}_{2pt}$ strategies. The analogous results for unrenormalized $g_{\pi NN}F_\pi$ are shown in Fig. 14 (right).

B. Extrapolation of g_P^* and $g_{\pi NN}$ to the physical point

1. g_P^*

Renormalized g_P^* is extrapolated to the physical point in two ways. In the first method $2m_\mu M_N \tilde{F}_P(Q^{*2})$ is extrapolated using the CCFV fit function given in Eq. (29) and multiplied by the pion-pole factor at the physical point:

$$g_P^* = 2m_\mu M_N \tilde{F}_P(Q^{*2})|_{\rm extrap} \times \left.\frac{1}{Q^{*2}+M_\pi^2}\right|_{\rm phys}. \tag{43}$$

TABLE IV. g_P^* from the z^2-expansion, dipole, and pion-pole dominance (PD) fits. The first column gives the strategy used for extracting the matrix elements. In each value, the first error is the total analysis error and the rest are systematic errors explained in the text.

g_P^*	z^2	Dipole	PD
$\mathcal{S}_{\rm sim}$	9.03(47)(01)(32)(27)	8.61(39)(···)(19)(23)	8.92(45)(···)(38)(33)
$\mathcal{S}_{A4}$	8.92(44)(04)(20)(23)	8.70(37)(···)(17)(15)	8.94(43)(···)(28)(33)
$\mathcal{S}_{\rm 2pt}$	4.50(26)(02)(···)(22)	5.36(25)(···)(···)(12)	4.73(27)(···)(···)(10)

In the second method, extrapolation of g_P^* is carried out by adding a pion-pole term, $b_4^{g_P^*}/(Q^{*2}+M_\pi^2)$, to the CCFV fit function in Eq. (29). The two methods give consistent estimates and their unweighted average is used to get the final results summarized in Table IV for each of the three strategies, $\mathcal{S}_{\rm sim}$, $\mathcal{S}_{A4}$, and $\mathcal{S}_{\rm 2pt}$.

The error obtained from the overall analysis is quoted as the first "stat" uncertainty. The systematical errors associated with truncation of the z-expansion, and the largest difference of the central value from the three 12-pt CCFV fits are quoted as the second and third errors. The difference between the two extrapolation methods described above is quoted as the fourth error. For the final result, we take the $\mathcal{S}_{\rm sim}$ with z^2 fits value:

$$\begin{aligned} g_P^* &= 9.03(47)_{\rm stat}(01)(32)(27), \qquad [z^2], \\ &= 9.03(47)_{\rm stat}(42)_{\rm sys}. \end{aligned} \tag{44}$$

In the second line, the three systematic errors are combined in quadrature. The 13-pt CCFV fit to the $\mathcal{S}_{\rm sim}$ data on each ensemble fit with z^2, is shown in Fig. 15.

2. $g_{\pi NN}$

The CCFV extrapolation to obtain $g_{\pi NN}$ is carried out using Eq. (29) for (i) the product $g_{\pi NN}F_\pi = M_N\tilde{F}_P(-M_\pi^2)$, and the result, in the continuum, divided by $F_\pi = 92.9$ MeV; and (ii) $\tilde{F}_P(-M_\pi^2)$ and the result multiplied by $M_N(=939\ \text{MeV})/F_\pi(=92.9\ \text{MeV})$. It turns out that these two extrapolations have different systematics: the slopes with respect to M_π^2 of $g_{\pi NN}F_\pi$ and $\tilde{F}_P(-M_\pi^2)$ are different as shown in Fig. 15. The two estimates are,

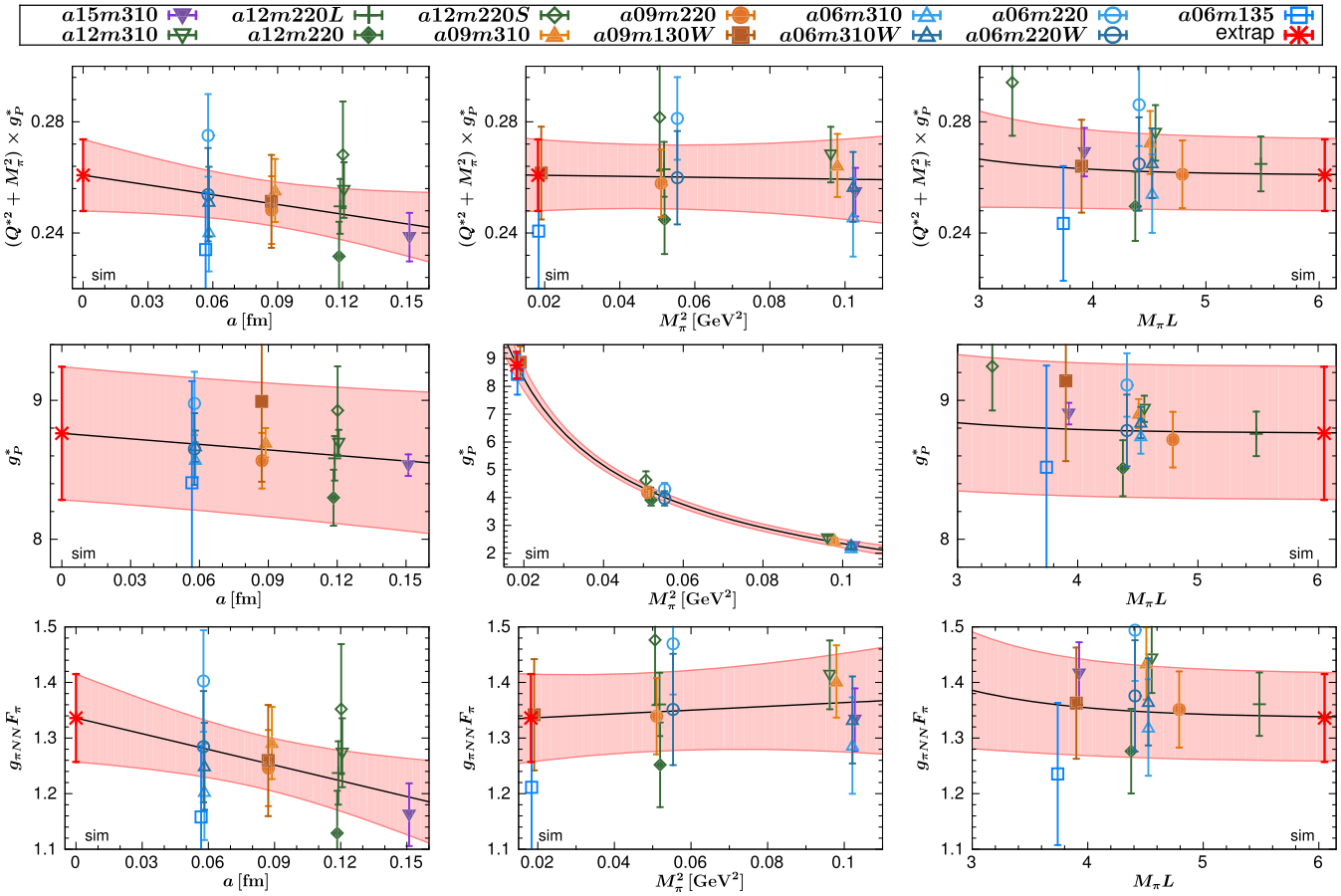

FIG. 15. The chiral-continuum-finite-volume extrapolation of the $(Q^{*2}+M_\pi^2)\times g_P^*$ (top row), g_P^* (middle row), and $g_{\pi NN}F_\pi$ (bottom row) data using the 13-point fit. In each case the data were obtained using the z^2 parametrization of $\tilde{F}_P(Q^2\neq 0)$ with strategy $\mathcal{S}_{\rm sim}$. The black solid line with the pink error band represents a hyperplane obtained by taking the physical limit of all CCFV fit variables except the one shown on the x-axis. The plotted data points have been shifted by using the fit coefficients, while the errors are unchanged.

TABLE V. Results for $g_{\pi NN}$ from the z^2, dipole, and pion-pole dominance (PD) fits. The first column gives the ESC strategy used to extract the matrix elements. The first error is statistical and the rest are systematic as explained in the text.

	z^2	Dipole	PD
$\mathcal{S}_{\rm sim}$	14.14(81)(01)(77)(35)	13.03(67)(···)(41)(28)	13.80(81)(···)(99)(33)
$\mathcal{S}_{A4}$	13.77(79)(07)(33)(29)	13.06(64)(···)(38)(26)	13.90(79)(···)(57)(31)
$\mathcal{S}_{\rm 2pt}$	05.76(57)(00)(···)(10)	07.57(46)(···)(···)(09)	06.24(57)(···)(···)(05)

however, consistent and we take their average to get the $g_{\pi NN}$ for the nine cases summarized in Table V: the three strategies and the three types of Q^2 fits.

The central value

$$\begin{aligned} g_{\pi NN} &= 14.14(81)_{\rm stat}(1)(77)(35) \\ &= 14.14(81)_{\rm stat}(85)_{\rm sys}. \qquad [z^2] \end{aligned} \tag{45}$$

is taken from the $\mathcal{S}_{\rm sim}$ data with z^2 fits and the errors are estimated as for g_P^*.

C. $\tilde{F}_P(Q^2)$ at the physical point

The $\tilde{F}_P(Q^2)$ at the physical point was obtained following the same three step procedure used for extrapolating $G_A(Q^2)$ that is described in Sec. III B. This $\tilde{F}_P(Q^2)$ is compared with the $G_A(Q^2)$ already shown in Fig. 12 in Fig. 16. If PPD were exact, then $\tilde{F}_P$ should equal G_A. The overlap of the two bands turns out to be surprisingly good over the whole Q^2 interval. Results for the four fit parameters, $b_i(Q^2)$, versus Q^2 obtained in the CCFV extrapolation process are shown up to 1 GeV^2 in Fig. 17 for data obtained with the $\mathcal{S}_{\rm sim}$ strategy.

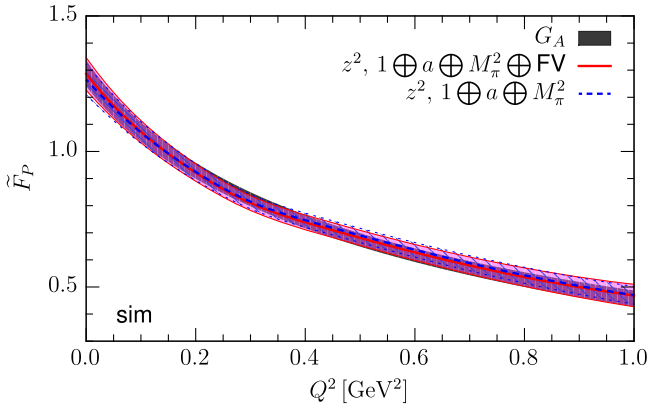

FIG. 16. The close overlap in the physical point results for $\tilde{F}_P(Q^2)$, defined in Eq. (41), with $G_A(Q^2)$ (black lines) reproduced from Fig. 12. Both were obtained using the three step process described in Sec. III B and the $\mathcal{S}_{\rm sim}$ strategy data. The full CCFV fits to the $\tilde{F}_P$ data are shown with the solid red line and pink error band and the fit without the FV term with dashed blue line and hatched error band. These error bands show only the central analysis uncertainty.

Similar to $G_A(Q^2)$, the two physical mass ensembles impact the coefficients $b_i(Q^2)$ shown in Fig. 17 only for $Q^2 \lesssim 0.4$ GeV^2. The plots show some pion mass dependence for $Q^2 < 0.2$ GeV^2, i.e., $b_2(Q^2) \neq 0$. The coefficients for the lattice spacing dependence, $b_1(Q^2)$, and for finite volume, $b_3(Q^2)$, have large uncertainty. Also, neglecting the finite volume term does not change $b_1(Q^2)$ and $b_2(Q^2)$ significantly. Overall, the shape of these coefficients versus Q^2 is somewhat different from those for G_A shown in Fig. 11.

The z^2 fit to the physical point $\tilde{F}_P$, shown in Fig. 16, with $t_c = 9M_\pi^2$ and $t_0 = 0.25$ GeV^2 has the parametrization

$$\begin{aligned} \tilde{F}_P(Q^2) &= a_0 + a_1 z + a_2 z^2 \\ &= 0.868(30) - 1.702(136) z + 0.587(601) z^2, \end{aligned} \tag{46}$$

with the correlation matrix:

$$\begin{array}{c} \\ a_0 \\ a_1 \\ a_2 \end{array} \begin{array}{c} \begin{array}{ccc} a_0 & a_1 & a_2 \end{array} \\ \begin{pmatrix} 1.0 & -0.45085 & -0.05106 \\ -0.45085 & 1.0 & -0.23890 \\ -0.05106 & -0.23890 & 1.0 \end{pmatrix} \end{array} \tag{47}$$

The agreement, within errors, with the parametrization of $G_A(Q^2)$ given in Eqs. (32) and (33) is very good. This is not unexpected based on the overlap between the two shown in Fig. 16, nevertheless, one should keep in mind the Q^2 dependence shown in Fig. 5, and the Goldberger-Trieman discrepancy [7,17].

V. NUCLEON CHARGES FROM FORWARD MATRIX ELEMENTS

The spectral decomposition of the forward, $\boldsymbol{q} = 0$, three-point function truncated at three states, $|i\rangle$ with $i = 0, 1, 2$, can be written as

$$\begin{aligned} &C_\Gamma^{\rm 3pt}(t;\tau) \\ &= \sum_{i,j=0} |A_j||A_i| \langle j|\mathcal{O}_\Gamma|i\rangle e^{-M_i t - M_j(\tau - t)} \\ &= |A_0|^2 g_\Gamma e^{-M_0 \tau} \times [1 + r_1^2 b_{11} e^{-\Delta M_1 \tau} \\ &\quad + r_2^2 b_{22} e^{-(\Delta M_1 + \Delta M_2)\tau} + 2 r_1 b_{01} e^{-\Delta M_1 \tau/2} \cosh(\Delta M_1 t_s) \\ &\quad + 2 r_2 b_{02} e^{-(\Delta M_1 + \Delta M_2)\tau/2} \cosh\{(\Delta M_1 + \Delta M_2) t_s\} \\ &\quad + 2 r_1 r_2 b_{12} e^{-(2\Delta M_1 + \Delta M_2)\tau/2} \cosh(\Delta M_2 t_s)] + \cdots, \end{aligned} \tag{48}$$

where $t_s \equiv t - \tau/2$, $\langle 0|\mathcal{O}_\Gamma|0\rangle$ is the bare charge g_Γ, the transition matrix elements are $b_{ij} \equiv \langle i|\mathcal{O}_\Gamma|j\rangle / \langle 0|\mathcal{O}_\Gamma|0\rangle$, the ratios of amplitudes are $r_i = |A_i|/|A_0|$, and the successive mass gaps are $\Delta M_i \equiv M_i - M_{i-1}$. The prefactors in terms involving the excited states are products such as $r_2^2 b_{22}$. These products are simply parameters in the fits and are not

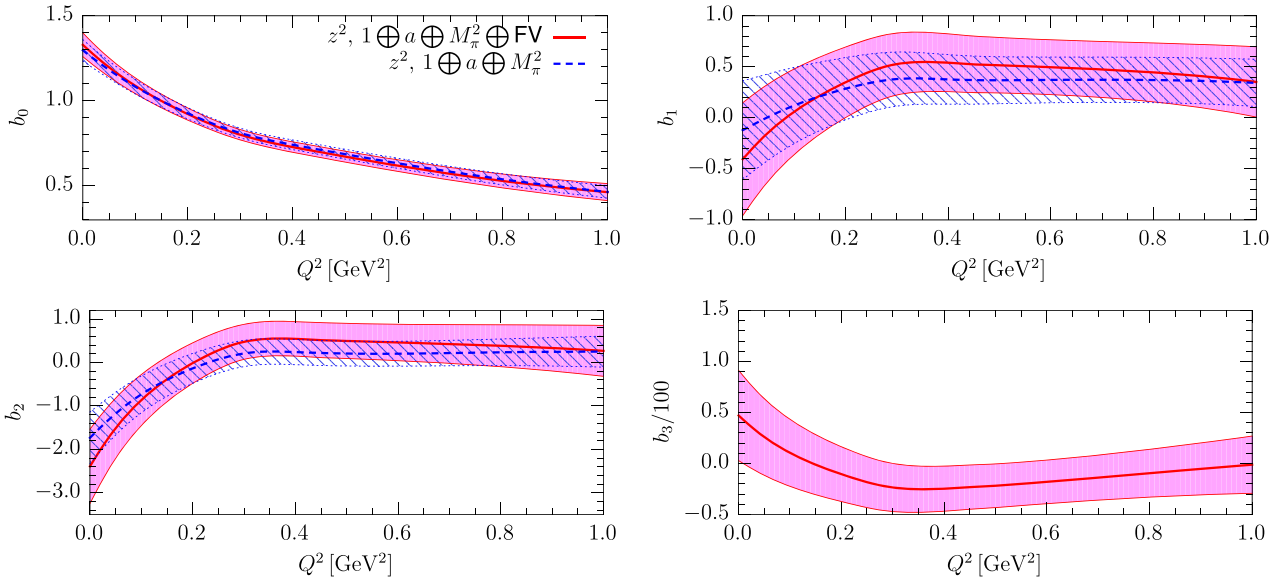

FIG. 17. The behavior of the four CCFV fit coefficients, b_0, b_1, b_2, and b_3 defined in Eq. (29) versus Q^2 obtained in the extrapolation of $\tilde{F}_P(Q^2)$ to the physical point. The rest is the same as in Fig. 16.

used subsequently. Thus the ratios r_i for the excited states are, by themselves, not needed.

To remove excited states contributions, we made three kinds of fits to the 3-point functions using Eq. (48):

(i) 3^*: This is a 3-state fit with b_{22} set to zero. The four parameters A_0, M_0, M_1, M_2 are taken from four-state fits to the two-point function, leaving only $\langle 0|\mathcal{O}_\Gamma|0\rangle$, and products such as $r_1^2 b_{11}$ as free parameters. This strategy (along with its two-state version) was used to get the results presented in Ref. [13] that are reproduced in Eq. (49).

(ii) 3-RD: This is a 3-state fit with b_{01}, b_{11} and b_{22} set to zero, otherwise the fits become unstable. The three parameters A_0, M_0, M_1 are again taken from four-state fits to the two-point function. The value of the second mass gap, ΔM_2, is left as a free parameter in the fit. The sign of ΔM_2 for a given charge determines whether $|1\rangle$ lies above or below $|2\rangle$ as shown pictorially in Fig. 18.

(iii) 3-RD-$N\pi$: In this fit, M_1 is fixed to the non-interacting energy of the $N(\boldsymbol{n})\pi(-\boldsymbol{n})$ state with $\boldsymbol{n} = (1,0,0)$. For the value of M_2, we use a Bayesian prior with a narrow width centered about the first excited state mass determined from the two-point correlator as given in Table XXX in Appendix F.

We also tried two-state fits with ΔM_1 left as a free parameter. For the axial charge, we found large fluctuations in ΔM_1 between the jackknife samples leading to unreliable values. So we do not present these estimates.

Results for unrenormalized isovector nucleon charges, g_A, g_T, and g_S, using the 3^*, 3-RD, and 3-RD-$N\pi$ fits are given in Table XXXI, and the other parameters of the 3-RD fits are given in Table XXXII in Appendix F.

The final renormalized charges are presented in the $\overline{\text{MS}}$ scheme at 2 GeV. We carry out the renormalization using the RI-sMOM intermediate scheme as described in Ref. [13]. To understand systematics, we use three methods: (i) $g_X = Z_X g_X^{(\text{bare})}$, where $X = A$, T, S; and (ii) $g_X = Z_X/Z_V \times g_X^{(\text{bare})}/g_V^{(\text{bare})}$ with the relation $Z_A g_V = 1$. Empirically, some of the systematics cancel in each ratio in the second method, giving slightly smaller overall errors. In method three, we take the average of the first two within the jackknife process, and use it to get the final estimates. The renormalization factors Z_X and Z_X/Z_V used in this study are given in Table V in Ref. [13].

We use the same leading order CCFV ansatz, given in Eq. (29), for extrapolating results to the physical point for all three strategies: 3^*, 3-RD, and 3-RD-$N\pi$.

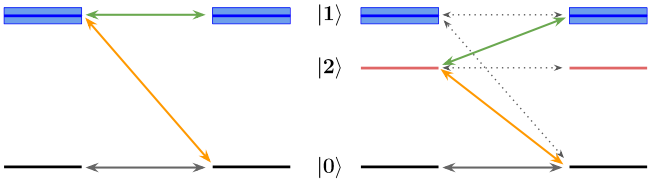

FIG. 18. A pictorial representation of the standard 2-state fit (left) and the 3-RD fit (right). In the 3-RD fit, the M_0 and M_1 are taken from the nucleon two-point correlator fit but ΔM_2 is determined from the fit to the three-point correlator. Negative values for ΔM_2 in Table XXXII indicate that $|2\rangle$ lies below $|1\rangle$. Both fits include only two transitions, $|0\rangle \to |1\rangle$ (yellow) and $|1\rangle \to |1\rangle$ (green) in the 2-state fit and $|0\rangle \to |2\rangle$ (yellow) and $|1\rangle \to |2\rangle$ (green) in the 3-RD fit. The transitions turned off with respect to the full 3-state ansatz given in Eq. (48) are represented by dashed lines.

Results from the 3^* (or 2-state for g_S) analysis, have already been published in Ref. [13], and reproduced here to facilitate comparison.[1] These are:

$$\begin{aligned} g_A &= 1.218(25)_{\text{stat}}(30)_{\text{sys}} \quad (3^*\text{-state}) \\ g_T &= 0.989(32)_{\text{stat}}(10)_{\text{sys}} \quad (3^*\text{-state}) \\ g_S &= 1.022(80)_{\text{stat}}(60)_{\text{sys}} \quad (2\text{-state}). \end{aligned} \tag{49}$$

We now focus on the 3-RD analysis and make three CCFV extrapolation with the following cuts on the data

(i) "13-point" CCFV fit uses all thirteen points.

(ii) "11-point" CCFV fit: This fit excludes the $a06m310W$ and $a06m220W$ points obtained with larger smearing radius for sources used to calculate the quark propagators [13]. Larger smearing radius reduces the ESC at smaller values of τ but gives larger statistical errors at the values of τ used in our excited-state fits to get the $\tau \to \infty$ values as discussed in Ref. [14]. Also, we expect significant correlations between the two pairs, ($a06m310$, $a06m310W$) and ($a06m220$, $a06m220W$), since they use the same gauge configurations. Comparing the pairs, the results for the three charges agree except for g_S between $a06m220$ and $a06m220W$, which can be accounted for by the larger statistical errors, especially in the $a06m220W$ data. Consequently, the "11-point" CCFV fit is used to get the central value for g_S, which is shown in Fig. 19.

(iii) "10-point" CCFV fit excludes $a15m310$, $a06m310W$ and $a06m220W$ points. Since the variation with the lattice spacing is the dominant systematic, removing the $a15m310$ point (coarsest lattice with $a \sim 0.15$ fm) aims to provide a handle on higher order, $\mathcal{O}(a^2)$, corrections neglected in Eq. (29).

Results from these three CCFV extrapolations, different truncations of the CCFV ansatz, and the three renormalization methods are given in Tables XXXIII–XXXV in Appendix F and used to assess the various systematics.

The central values are taken from the "13-point fit" for g_A and g_T and the "11-pt fit" for g_S with the 3-RD data renormalized using the third (average of the first two) method. Note that we find a systematic shift of ≈0.03, 0.02 and 0.03 between the first two renormalization methods for the three charges, g_A, g_T, and g_S, respectively.

These CCFV fits are shown in Fig. 19. Each panel in a given row shows the fit result versus one of the three variables with the other two set to their physical point values. In the left two panels, we show two fits: (i) using the full ansatz given in Eq. (29) (pink band), and (ii) assuming there is dependence only on the x-axis variable (gray band). For example, in the left panels the gray band corresponds to a fit with $b_2^{g_x} = b_3^{g_x} = 0$. The data show that the discretization errors are the dominant systematic, i.e., there is an almost complete overlap of the two fits (pink and gray bands) for g_A and a significant overlap for g_S and g_T. The variation with a over the range $0 < a \le 0.15$ fm is about 10%, 5%, and 30% for g_A, g_T, and g_S, respectively. The large variation with a in g_S is similar to that found in the clover-on-clover calculation [7].

The final results of the 3-RD analysis are

$$\begin{aligned} g_A &= 1.294(42)_{\text{stat}}(18)_{\text{CCFV}}(16)_{\text{Z}} \quad (3\text{-RD}) \\ g_T &= 0.991(21)_{\text{stat}}(04)_{\text{CCFV}}(09)_{\text{Z}} \quad (3\text{-RD}) \\ g_S &= 1.085(50)_{\text{stat}}(102)_{\text{CCFV}}(13)_{\text{Z}} \quad (3\text{-RD}). \end{aligned} \tag{50}$$

The first error quoted (labeled stat) is the total uncertainty from the central analysis. The second error is an estimate of the uncertainty in the CCFV extrapolation. For g_A and g_T, this is taken to be the average of the differences |11-pt − 13-pt| and |10-pt − 13-pt|. For g_S, it is the difference |10-pt − 11-pt|. The third error is half the difference in estimates between the first two renormalization methods.

The g_A from the 3-RD fit is in good agreement with the result obtained from the extrapolation of the axial form factor $G_A(Q^2)$ to $Q^2 = 0$ given in Eq. (30). It is also consistent with the experimental value $g_A = 1.2766(20)$ but has much larger errors. The difference between the 3^* (PNDME [13]) value reproduced in Eq. (49), and the 3-RD is due to different excited state energies used in the fits to the spectral decomposition in Eq. (48). The data in Table XXXII show that the fit parameter M_2 when left free satisfies $M_\pi \lesssim M_2 - M_0 \lesssim 3M_\pi$ for all but the $a \approx 0.12$ fm lattices. In [10], we showed evidence that the $N(\boldsymbol{p}_1) + \pi(-\boldsymbol{p}_1)$ with $\boldsymbol{p}_1 = (1,0,0)2\pi/La$ state makes a significant contribution on the zero momentum side of the operator insertion in the calculation of the form factors, and the noninteracting energy of this state is $M_{N\pi} - M_0 \approx 2M_\pi$. In short, the M_2 output by the 3-RD fit has a mass lower than M_1 obtained from the two-point correlator and broadly consistent with the hypothesis that the $N\pi$ states contribute. We again caution the reader that these excited state masses should only be regarded as effective fit parameters that encapsulate the effect of the full tower of $N(\boldsymbol{p}) + \pi(-\boldsymbol{p})$ states with momenta $\boldsymbol{p} = (2\pi/L)\boldsymbol{n}$ as well as other multihadron and radial excitations that can contribute.

For g_S and g_T, the 3-RD fit reduces to a 2-state fit if $\Delta M_2 (= M_2 - M_1) = 0$, i.e., $M_2 \simeq M_1$. This is the case for many of the ensembles as shown in Table XXXII. Results given in Eq. (50) are consistent with those in Eq. (49) indicating that sensitivity to excited state energies input into the analysis is small.

Based on the 3-RD fits, which indicate that the data for g_A prefer a low-mass excited state with $\Delta M \approx 2M_\pi$, the 3-RD-$N\pi$ fit defined above, with the mass gaps summarized in Table XXX, were performed. Charges from this fit are compared with the 3-RD and the 3^*-state fits (or the

[1]The statistics in the a06m135 and a12m310 ensembles have been increased, however, the changes in the estimates are insignificant, so we continue to quote the results from Ref. [13].

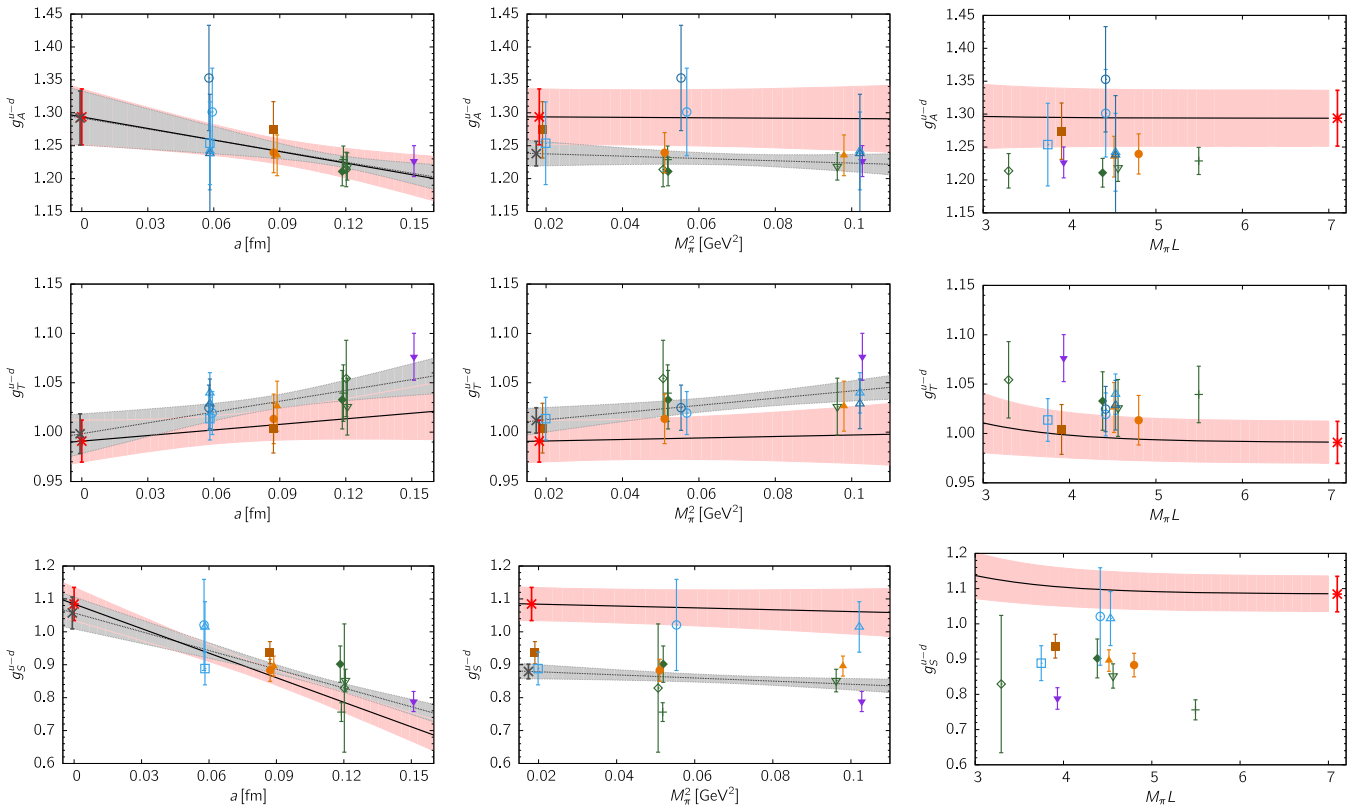

FIG. 19. The simultaneous chiral-continuum-finite-volume (CCFV) fit to the axial g_A (top, 13-point), tensor g_T (middle, 13-point), and scalar g_S (bottom, 11-point) charges. The data are extracted using the 3-RD fit described in the text and are the average over the two renormalization methods $Z_X \times g_X^{(\text{bare})}$ and $Z_X/Z_V \times g_X^{(\text{bare})}/g_V^{(\text{bare})}$ where the g_V is the vector charge. In each panel, the pink bend with black solid line represents the full CCFV fit. In the left (middle) panels, the gray band shows the fit to the date keeping only the a (M_π^2) dependent term in Eq. (29). The value at the physical point is marked by the red star. The data in each panel have not been shifted to the physical point in the other two fit variables.

2-state fit for the g_S) in Table XXXI for the thirteen ensembles. The p-value for many of the 3-RD-$N\pi$ fits are low. To stabilize the 3-RD-$N\pi$ fits, we increased the width of the priors for M_2, however, this still did not lead to stable fits for several ensembles. The 3-RD-$N\pi$ results are, therefore, not included in the final analysis.

Results for $g_{A,S,T}$ in Eq. (50) are compared with those from other collaborations in Table VI. This comparison complements the latest FLAG review that considered results published prior to 2021 [5,6]. Overall, results for g_A and g_T from all calculations are consistent within five percent and for g_S at ten percent. Their precision will continue to improve steadily as higher statistics data are generated at additional $\{a, M_\pi\}$ points with $M_\pi L \gtrsim 4$.

Our conclusion is that, with current statistics, fits for the axial charge are more stable with input of M_0 and M_1 from

TABLE VI. Comparison of $g_{A,S,T}$, $\langle r_A^2 \rangle$, g_P^* and $g_{\pi NN}$ from recent calculations labeled as: PNDME 23 is this work, RQCD [24] (here we list values obtained with the $!z^{4+3}$ fit, and take $g_{A,S,T}$ from their recent work [25]), ETMC [26,27], NME [7], Mainz [28], and PACS [29]. All results for $g_{A,S,T}$ are in the $\overline{\text{MS}}$ scheme at scale 2 GeV. For completeness, we also give results for $g_{S,T}$ from the Mainz collaboration [30] and from the ETMC collaboration [27,31]. These and earlier results are reviewed by the FLAG [5,6].

Collaboration	g_A	g_S	g_T	$\langle r_A^2 \rangle$ fm^2	g_P^*	$g_{\pi NN}$
PNDME 23	1.292(53)(24)	1.085(50)(103)	0.991(21)(10)	0.439(56)(34)	9.03(47)(42)	14.14(81)(85)
RQCD 19/23	1.284^{28}_{27}	1.11^{14}_{16}	0.984^{19}_{29}	0.449(88)	8.68(45)	12.93(80)
ETMC 20/22	1.283(22)	1.35(17)	0.924(54)	0.343(42)(16)		
NME 21	1.32(6)(5)	1.06(9)(7)	0.97(3)(2)	0.428(53)(30)	7.9(7)(9)	12.4.(1.2)
Mainz 22	1.225(39)(25)	$1.13(11)(^{7}_{6})$	$0.965(38)(^{13}_{41})$	0.370(63)(16)		
PACS 22	1.288(14)(9)	0.927(83)(22)	1.036(6)(20)			

the 4-state fit to the 2-point function and letting the 3-point function determine M_2 (corresponding roughly to the $N\pi$ state), i.e., the 3-RD fit. In future works with higher statistics, we expect results from 3-RD and 3-RD-$N\pi$ fits to come together as the same three states provide the dominant contributions. Only the details of their inclusion are different.

VI. CONCLUSIONS AND COMPARISON WITH PREVIOUS CALCULATIONS

We have presented results for the axial, $G_A(Q^2)$, the induced pseudoscalar, $\tilde{G}_P(Q^2)$, and the pseudoscalar, $G_P(Q^2)$, form factors of nucleons using thirteen ensembles of $2+1+1$-flavors of HISQ ensembles generated by the MILC collaboration [8]. A large part of the focus of this work is on understanding the nature of the excited states that contribute significantly to the relevant correlation functions and removing their contributions. The analysis presented here strengthens the case for including multihadron excited states, such as $N\pi$, made in Ref. [10]. Our data driven analysis strategy, labeled $\mathcal{S}_{\rm sim}$, identifies the contributions from $N\pi$ state in the extraction of the GSME. The three form factors obtained including $N\pi$ state satisfy the PCAC relation to within 10% as opposed to a ∼50% deviation without them. For the final results, we therefore choose the data obtained with the $\mathcal{S}_{\rm sim}$ strategy for removing ESC, parametrize the Q^2 behavior using the model-independent z^2 fit; and extrapolate the data to the physical point using a simultaneous chiral-continuum-finite-volume (CCFV) ansatz including the leading order corrections given in Eq. (29). For errors, we quote two estimates: the first labeled "stat" is the total error obtained from the analysis used to produce the central value, and the second, labeled "sys," includes the various systematic uncertainties combined in quadrature as discussed in the appropriate sections.

Our final results are

(i) The axial charge is $g_A = 1.292(53)_{\rm stat}(24)_{\rm sys}$. This is the unweighted average of the value from the extrapolation of $G_A(Q^2)$ to $Q^2 = 0$ [Eq. (36)] and from the forward matrix element [Eq. (50)]. The "stat" and "sys" errors quoted are the larger of those from the two determinations. This result is consistent with the experimental value but has much larger errors.

(ii) The scalar charge $g_S = 1.085(50)_{\rm stat}(103)_{\rm sys}$ and the tensor $g_T = 0.991(21)_{\rm stat}(10)_{\rm sys}$ are given in Eq. (50).

(iii) The extraction of the axial charge radius squared is discussed in Sec. III B, and the result from Eq. (36) is $\langle r_A^2\rangle = 0.439(56)_{\rm stat}(34)_{\rm sys}$ fm^2.

(iv) The extraction of the induced pseudoscalar charge is discussed in Sec. IV B 1 with the result $g_P^* = 9.03(47)_{\rm stat}(42)_{\rm sys}$ given in Eq. (44).

(v) The pion-nucleon coupling is discussed in Sec. IV B 2 with the result $g_{\pi NN} = 14.14(81)_{\rm stat}(85)_{\rm sys}$ given in Eq. (45).

(vi) Our procedure for obtaining the axial form factor, $G_A(Q^2)$, in the continuum limit is discussed in Sec. III B. The final parametrization is given in Eq. (32), the covariance matrix of the fit in Eq. (33), and the corresponding values of $g_A = 1.281(53)$ and $\langle r_A^2\rangle = 0.498(56)$ fm^2 in Eq. (34). The overall final values from the analysis of G_A are given in Eq. (36).

A comparison of lattice results from various collaborations for all the above quantities was presented recently in Ref. [7]. The charges $g_{A,S,T}$ have also been reviewed by FLAG [5,6]. Since then, new results have been presented in Refs. [27–29,32]. The full list of relevant publications that have included $N\pi$ states in the analysis of ESC and checked whether form-factors satisfy the PCAC relation are [7,10,24,26,28,29]. We first summarize the results and the important features in each of these calculations, and then show a comparison of $G_A(Q^2)$ obtained by the various collaborations in Fig. 20. Results for the charges are compared in Table VI.

The observation that the form factors extracted using the spectrum from the nucleon 2-point function fail to satisfy the PCAC relation Eq. (17) was made in Ref. [9]. The possible cause, enhanced contributions of multihadron ($N\pi$) excited states in the axial channel was proposed by Bär [12] using a χPT analysis. This was confirmed using the data for the three-point function with the insertion of the A_4 current in Ref. [10]. This data-driven analysis, including only the lowest $N\pi$ excited state, found that the ESC to the $\tilde{G}_P(Q^2)$ and $G_P(Q^2)$ form factors were about 35%, while that in $G_A(Q^2)$ could be $O(5\%)$ as the latter is affected only at one-loop in χPT [11,12]. The smallest Q^2 data in Tables XVII and XXII in Appendix C for the two physical mass ensembles $a09m130W$ and $a06m135$ show ∼5%, ∼45% and ∼45% difference between the $\mathcal{S}_{\rm 2pt}$ and $\mathcal{S}_{\rm sim}$ values. A ∼ 5% level of effect in $G_A(Q^2)$ is also consistent with what is observed in the axial charge g_A extracted from the forward matrix element as shown in Table XXXI in Appendix F.

A brief comparison of our results with other lattice calculations published in [7,24,26–29] is as follows.

The RQCD collaboration [24] has extracted $G_A(Q^2)$ from a two-state fit to thirty-six $2+1$-flavor Wilson-clover ensembles generated by the coordinated lattice simulations (CLS) collaboration. The $\tilde{G}_P(Q^2)$ and $G_P(Q^2)$ are, on the other hand, extracted using a 3-state fit in which the first excited state energies are fixed to be the noninteracting energies of the lowest $N\pi$ state and the second excited state energies are taken to be the first excited state (values higher than $N(1440)$) given by fits to the 2-point nucleon correlators. While their form factors satisfy the PCAC relation, they are equally well fit by the dipole ansatz and z^{4+3} (i.e., z^3 with sum rule constraints). The axial charge $g_A = 1.302(86)$ from z-expansion (fit labeled $!z^{4+3}$) is larger than $g_A = 1.229(30)$ from dipole (labeled $!2P$) with the latter agreeing with that from the forward matrix

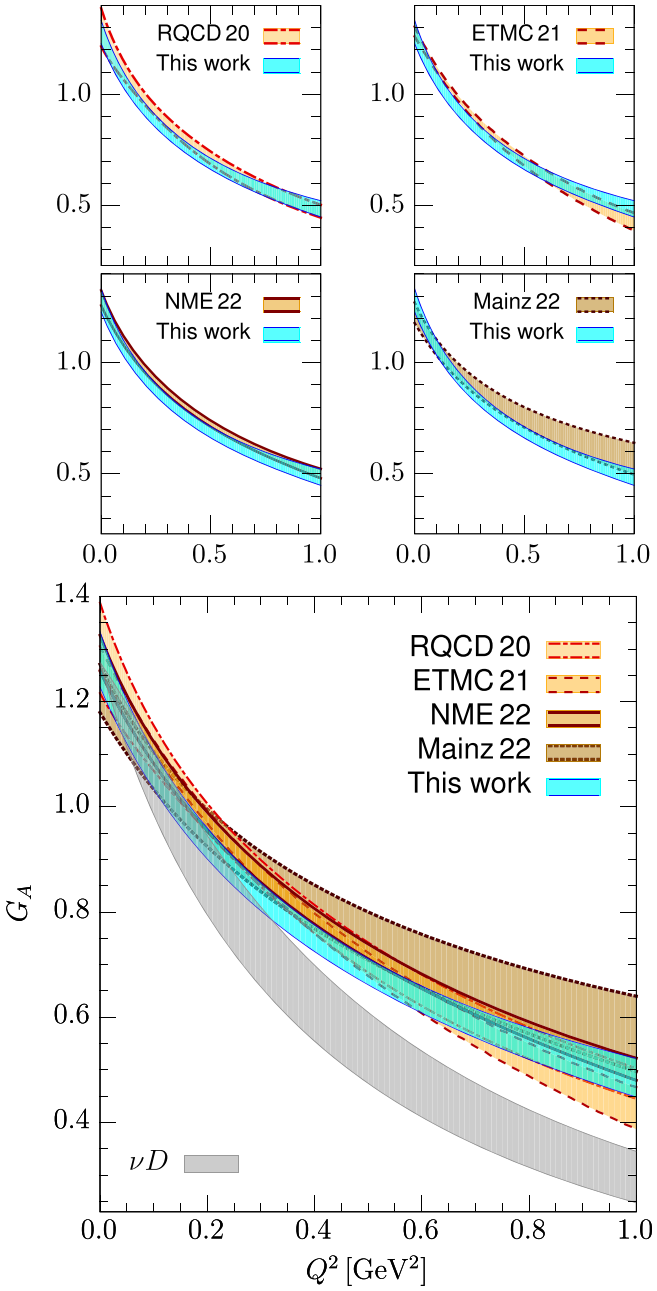

FIG. 20. A comparison of the isovector axial form factor $G_A(Q^2)$ at the physical point obtained using a z-expansion fit by the RQCD [24] (light faun band), ETMC [26] (light tan band), NME [7] (tan band), Mainz [28] (brown band) collaborations and this work (turquoise band). The G_A extracted using the ν-deuterium bubble chamber scattering experiments data [22] is shown by the gray band and labeled νD in the lower panel.

element. The corresponding difference in $\langle r_A^2 \rangle$ is 0.449(88) versus 0.272(33) fm^2. Results for g_P^* [8.68(45) versus 8.30 (24)] and for $g_{\pi NN}$ [12.93(80) versus 14.78(1.81)] are consistent. They have recently [25] updated their results for $g_{A,S,T}$ based on the analysis of 47 ensembles. We quote these new values in Table VI.

The preferred estimates from the ETM collaboration [26] are from a single $2+1+1$-flavor physical mass $64^3 \times 128$ ensemble at $a \approx 0.8$ fm. For the analysis of $G_A(Q^2)$, they take excited-state energies from the 2-point function and find $\langle r_A^2 \rangle = 0.343(42)(16)$ fm^2. Their result for $g_A = 1.283(22)$ is obtained from the forward matrix element extracted without including possible contamination from $N\pi$ states. When results from the direct calculations of $\tilde{G}_P(Q^2)$ and $G_P(Q^2)$ are used, the three form factors show large deviations from the PCAC relation which they attribute partially to large discretization errors in their twisted mass formulation [33]. Consequently, they quote final estimates of $\tilde{G}_P(Q^2)$ derived from $G_A(Q^2)$ using the pion-pole dominance hypothesis, i.e., the quoted $\tilde{G}_P$ is not independently determined.

The NME collaboration [7] analyzed seven ensembles generated with $2+1$-flavors of Wilson-clover fermions. They make a simultaneous fit to all five correlation functions with insertion of the axial, A_μ, and pseudoscalar, P, currents, i.e., same as the $\mathcal{S}_{\rm sim}$ strategy used in this work. The A_4 correlator provides the dominant contribution to fixing the excited-state energies which turn out to be close to the lowest $N\pi$ states as also discussed in this paper and in Ref. [10]. The resulting form factors satisfy the PCAC relation to within ten percent. Observing only a small dependence of $G_A(Q^2)$ on a and M_π, they provide a continuum parametrization of $G_A(Q^2)$ neglecting these effects, and thus underestimate the uncertainty. This $G_A(Q^2)$ is reproduced in Fig. 20. The value of the axial charge without including $N\pi$ state is $g_A = 1.242(46)(42)$ and including it gives 1.32(6)(5). Their other results are $\langle r_A^2 \rangle = 0.428(53)(30)$ fm^2, $g_P^* = 7.9(7)(9)$ and $g_{\pi NN} = 12.4.(1.2)$.

The Mainz Collaboration [28] analyze fourteen $2+1$-flavor Wilson-clover ensembles also generated by the coordinated lattice simulations (CLS) collaboration. They obtain a parametrization of $G_A(Q^2)$ in the continuum from a single combined fit—summation method for dealing with ESC and the z^2 fit for the Q^2 behavior. This result is shown in Fig. 20 and from it they get $g_A = 1.225(39)(25)$ and $\langle r_A^2 \rangle = 0.370(63)(16)$ fm^2.

The PACS collaboration [29] has analyzed one physical pion mass ensemble with a large volume (128^4, i.e., (10.9 fm)^4) at $a = 0.085$ fm and get $g_A = 1.288(14)(9)$. Remarkably, they find that sources with exponential smearing for the generation of quark propagators, in contrast to Gaussian smearing used by all other calculations, leads to essentially no excited-state effects. The limitation of this calculation is only 20 configurations, each separated by 10 molecular dynamics trajectories, were analyzed. Most likely, this total of 200 trajectories represents less than one unit of autocorrelation time. Consequently, the errors are likely underestimated.

Since no parametrization of $G_A(Q^2)$ was presented, we do not include their results in the comparison.

Phenomenologically, the most important quantity needed for the analysis of neutrino oscillation experiments is $G_A(Q^2)$, and we show a comparison of results from various lattice collaborations in Fig. 20 along with the extraction from the ν-deuterium bubble chamber scattering experiments [22]. In all cases, except ETM, the data are extrapolated to the physical point and then fit using a truncated z-expansion. The bands in Fig. 20 overlap indicating that the lattice results are consistent within one sigma and the envelope of the bands suggests a roughly 10% uncertainty throughout the range $0 < Q^2 < 1.0$ GeV^2. The other significant observation is that the lattice results fall slower than the phenomenological extraction (the νN band) for $Q^2 \gtrsim 0.3$ GeV^2.

When comparing these lattice data, it is important to note that the various collaborations handle various systematics differently. These systematic effects will become clearer and the analysis more robust as the precision of the data increases. Similarly, recent calculations including $N\pi$ states in a variational basis of interpolating operators [34] is a step forward in providing further insight into the excited states contributions and developing better methods for removing them.

What has become clear is that $N\pi$ states need to be included in the analysis for the three form factors, and satisfying the PCAC relation (17) is an essential and necessary condition. The questions that remain for higher precision are how many multihadron states need to be kept in the spectral decomposition for a given precision and the size of their contributions. The roughly 10% spread in the lattice results compared in Fig. 20 will be reduced with much higher statistics data that will be available over the next few years, and better analyses of excited states contributions.

ACKNOWLEDGMENTS

We thank the MILC collaboration for providing the $2+1+1$-flavor HISQ lattices used in this study. The calculations used the Chroma software suite [35]. This research used resources at (i) the National Energy Research Scientific Computing Center, a DOE Office of Science User Facility supported by the Office of Science of the U.S. Department of Energy under Contract No. DE-AC02-05CH11231; (ii) the Oak Ridge Leadership Computing Facility, which is a DOE Office of Science User Facility supported under Contract No. DE-AC05-00OR22725, through awards under the ASCR Leadership Computing Challenge (ALCC) program Project No. LGT107 and Innovative and Novel Computational Impact on Theory and Experiment (INCITE) Grant No. HEP133; (iii) the USQCD collaboration, which is funded by the Office of Science of the U.S. Department of Energy; and (iv) Institutional Computing at Los Alamos National Laboratory. T. B. and R. G. were partly supported by the U.S. Department of Energy, Office of Science, Office of High Energy Physics under Contract No. DE-AC52-06NA25396. T. B., R. G., and B. Y. were partly supported by the LANL Laboratory Directed Research and Development (LDRD) program.

APPENDIX A: DETERMINING THE NUCLEON SPECTROM FROM $C^{2pt}(t)$

To extract the nucleon spectrum, we make two kinds of fits to the spectral decomposition of $C^{2pt}(t)$. The first is a frequentist (labeled F) multiexponential fit, i.e., without any priors. It is a three-state fit for $a \approx 0.06, 0.09$ fm ensembles, and two-state for $a \approx 0.12, 0.15$ fm ensembles. These frequentist results ($n_s = 2$ or 3) are compared against empirical Bayesian four-state fits ($n_s = 4$) in Table VII, and

TABLE VII. Comparison of the ground state nucleon mass obtained from fits to the dispersion relation, $E_{\boldsymbol{p}}^2 = (M_0^{\text{Disp}})^2 + c^2\boldsymbol{p}^2$ with M_0^{2pt} from zero-momentum two-point correlator. Here n_s is the number of states kept in the fits with $n_s = 2$ or 3 implying a frequentist fit and $n_s = 4$ implying an empirical Bayesian fit. The speed of light c^2, the χ^2/d.o.f. and p-value are for the fits to the dispersion relation, which are shown for the $a09m130W$ and $a06m135$ ensembles in Fig. 22.

ID	n_s	aM_0^{2pt}	aM_0^{Disp}	c^2	$\hat{\chi}^2$/d.o.f.	p
$a15m310$	4	0.8302(21)	0.8304(21)	0.930(12)	1.37	0.195
$a15m310$	2	0.8315(20)	0.8319(19)	0.936(11)	0.96	0.474
$a12m310$	4	0.6660(27)	0.6662(26)	1.001(14)	0.62	0.777
$a12m310$	2	0.6715(13)	0.6716(13)	1.001(09)	0.73	0.685
$a12m220L$	4	0.6125(21)	0.6135(17)	0.995(15)	0.39	0.940
$a12m220L$	2	0.6187(10)	0.6187(10)	1.013(07)	0.67	0.741
$a12m220$	4	0.6080(31)	0.6086(30)	0.989(27)	0.33	0.967
$a12m220$	2	0.6151(14)	0.6152(14)	1.001(10)	0.91	0.515
$a12m220S$	4	0.6039(52)	0.6110(41)	0.970(29)	1.19	0.297
$a12m220S$	2	0.6194(26)	0.6204(24)	0.997(21)	0.69	0.718
$a09m310$	4	0.4951(14)	0.4959(13)	1.027(13)	1.72	0.078
$a09m310$	3	0.4952(15)	0.4961(13)	1.024(14)	0.96	0.473
$a09m220$	4	0.4495(20)	0.4513(15)	1.020(16)	0.36	0.955
$a09m220$	3	0.4514(16)	0.4528(13)	1.021(14)	0.53	0.857
$a09m130W$	4	0.4208(17)	0.4221(16)	0.978(31)	0.77	0.647
$a09m130W$	3	0.4213(18)	0.4225(17)	0.981(31)	1.12	0.342
$a06m310$	4	0.3248(30)	0.3257(28)	0.996(42)	0.97	0.422
$a06m310$	3	0.3305(21)	0.3319(19)	1.059(25)	0.80	0.524
$a06m310W$	4	0.3277(18)	0.3296(16)	1.025(22)	2.11	0.077
$a06m310W$	3	0.3289(16)	0.3303(14)	1.030(19)	2.14	0.073
$a06m220$	4	0.3036(19)	0.3035(19)	0.926(52)	0.26	0.902
$a06m220$	3	0.3065(17)	0.3060(16)	0.987(42)	1.22	0.299
$a06m220W$	4	0.3030(21)	0.3045(17)	1.033(40)	0.51	0.730
$a06m220W$	3	0.3047(14)	0.3053(13)	1.027(25)	0.33	0.858
$a06m135$	4	0.2714(24)	0.2716(22)	0.857(48)	0.48	0.886
$a06m135$	3	0.2735(16)	0.2737(16)	1.008(35)	0.33	0.967

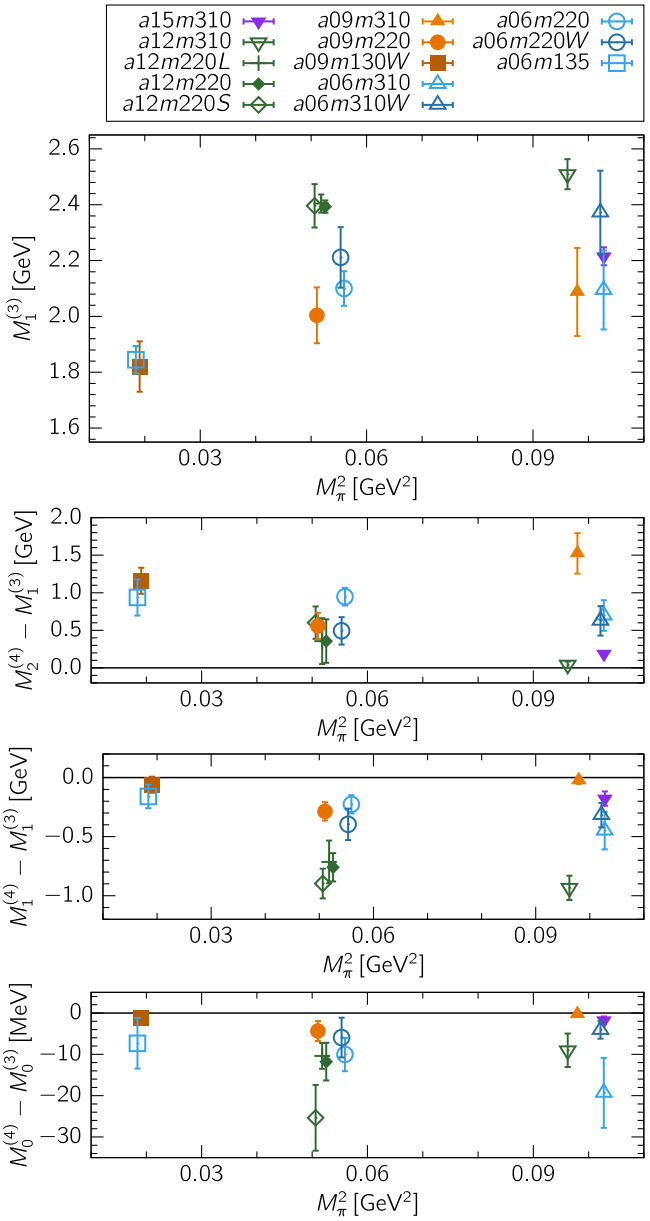

FIG. 21. Top: the first excited state mass, $M_1^{(3)}$, from the frequentist 3-state (or 2-state) fit. The mass differences $M_2^{(4)} - M_1^{(3)}$ and $M_1^{(4)} - M_1^{(3)}$ are shown in the second and third panels. The difference in the ground state mass, $M_0^{(4)} - M_0^{(3)}$, is given in the bottom panel.

their difference is shown in Fig. 21 (bottom panel). We observe that

(i) The ground state masses from the F- and B-fits given in Table VII are consistent within one combined σ. There is, however, a small but systematic shift with $M_0^{(4)} < M_0^{(3)}$, indicating near convergence. The deviations are $\approx$10 MeV on all except $a12m220S$ and $a06m310$ ensembles, where they are 20–30 MeV. Overall, the B-fit values are smaller.

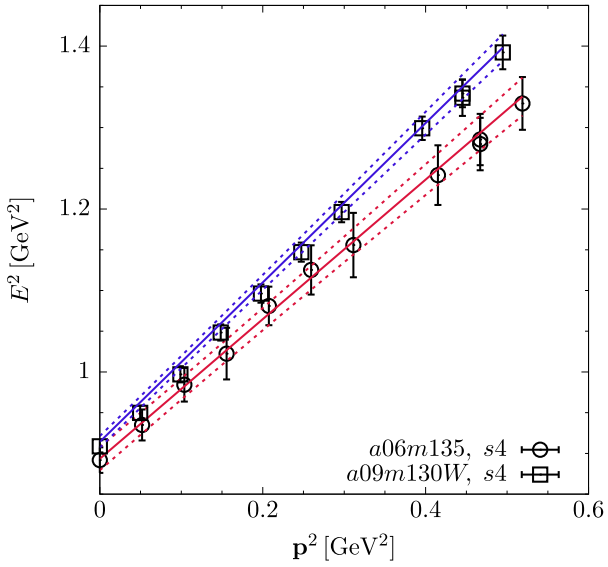

FIG. 22. The plot of E^2 obtained from the Bayesian four-state fit versus $\boldsymbol{p}^2$ for the $a09m130W$ (squares) and $a06m135$ (circles) ensembles. The slope gives the speed of light, c^2 listed in Table VII. It shows significant deviation from unity for the $a06m135$ ensemble. Note that the blue line lying above most square points is a consequence of including the full covariance matrix.

(ii) For all except the $a15m310$ and $a06m135$ ensembles, the E^2 obtained from the four-state Bayesian fit satisfy the relativistic dispersion relation, i.e., the speed of light, c^2, is consistent with unity to within 1σ. The fits for the $a09m130W$ and $a06m135$ ensembles are shown in Fig. 22.

The analysis of the first excited state mass from fits to the three-point correlations functions has been presented in Sec. II D. Here we study its extraction from the spectral decomposition of $C^{\mathrm{2pt}}(t)$:

$$C^{\mathrm{2pt}}(t) = a_0 e^{-E_0 t}\left\{1 + \sum_{k=1}^{\infty} b_k e^{-(E_k - E_0)t}\right\}, \quad \text{(A1)}$$

where the coefficients a_0 and b_k are positive definite since the same interpolating operator is used at the source and the sink. Starting from the definition of the effective mass

$$m_{\mathrm{eff}}(t) = \log \frac{C(t)}{C(t+1)} \quad \text{(A2)}$$

one can derive, using the symmetric lattice derivative $df(t)/dt \to (f(t+1) - f(t-1))/2$, a series of effective masses $m_{\mathrm{eff}}^{(n)}$

$$m_{\mathrm{eff}}^{(0)} \equiv -\frac{d}{dt}\log C^{\mathrm{2pt}}(t) \quad \text{(A3)}$$

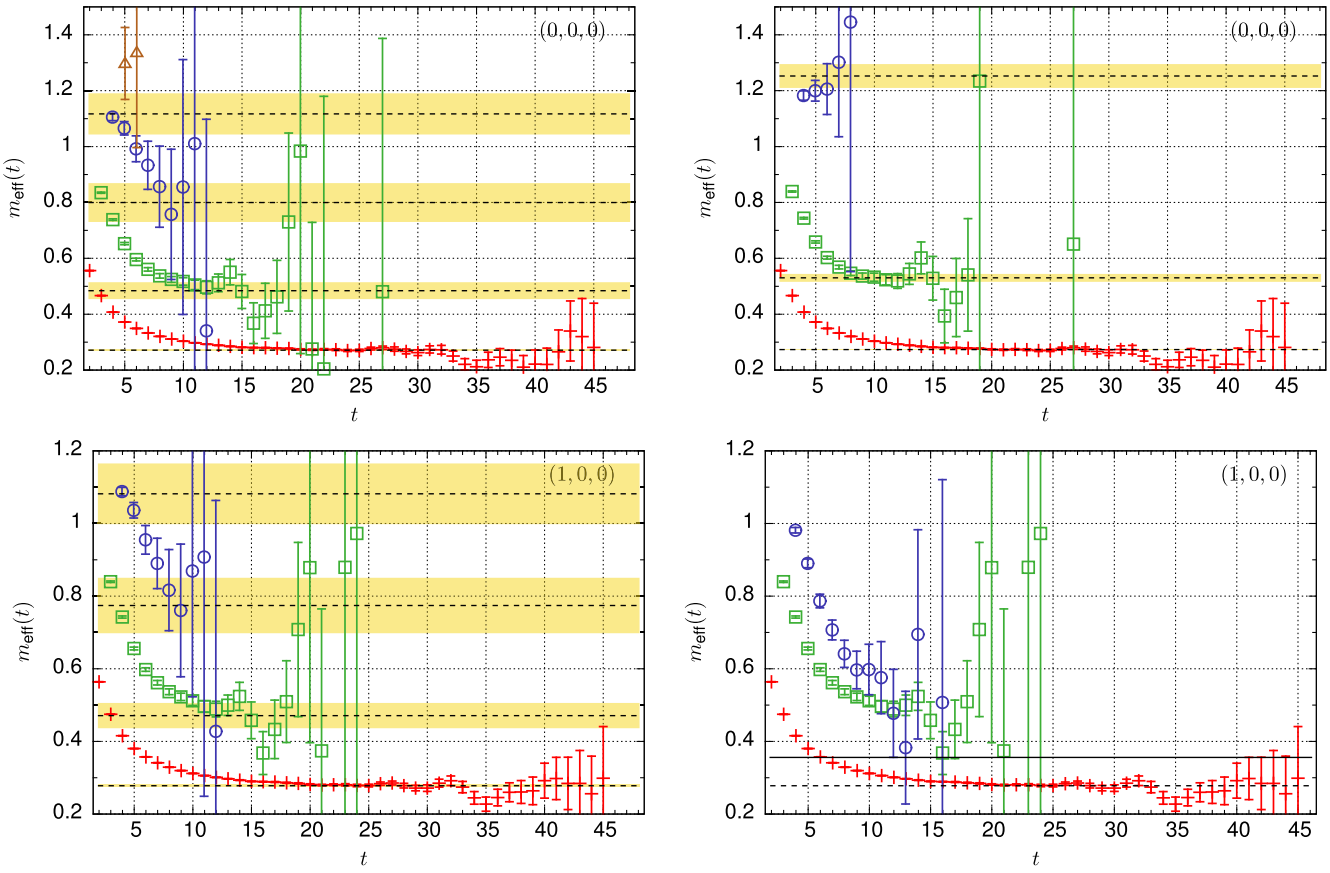

FIG. 23. Data for the effective masses $m_{\rm eff}^{(n)}$, defined in Eq. (A4), from the a06m135 two-point correlators. Top panel shows results for $\boldsymbol{p} = \boldsymbol{0}$ with the E_{n-1} in Eq. (A4) taken from the four-state fit (left) and three-state fit (right). These input energy levels E_n are shown by the dashed lines with yellow error bands. The red plus, green square, and blue circle symbols correspond to $m_{\rm eff}^{(n)}$ with $n = 0$, 1, 2, respectively. The bottom panel shows $m_{\rm eff}^{(n)}$ for $\boldsymbol{p} = 2\pi\boldsymbol{n}/L, \boldsymbol{n} = (1, 0, 0)$. In the bottom right panel, E_0 is taken from the four-state fit and $E_1 = E_0 + 2M_\pi$ (solid black line) is assumed.

$$m_{\rm eff}^{(n)} \equiv m_{\rm eff}^{(n-1)} - \frac{d}{dt}\log(m_{\rm eff}^{(n-1)} - E_{n-1}) \tag{A4}$$

$$= E_n - \frac{d}{dt}\log\left\{1 + \sum_{k=n+1}^{\infty} \frac{b_k}{b_n}\frac{(E_k - E_0)\cdots(E_k - E_{n-1})}{(E_n - E_0)\cdots(E_n - E_{n-1})} e^{-(E_k - E_n)t}\right\}, \qquad (n = 1, 2, \ldots). \tag{A5}$$

that should approach a plateau from above at a sufficiently large time t and give the energy levels E_n. To determine $m_{\rm eff}^{(n)}(t)$, one could take the E_n from a multi-exponential fit, with n limited by the statistical quality of the data. Note that no prior information of the overlap factors a_0 and b_k is required to calculate $m_{\rm eff}^{(n)}(t)$.

These effective masses for the a06m135 ensemble are shown in Fig. 23 for the lowest two momenta and compared with when the E_i are taken from a four- (left panels) versus three-state (right panels) fits with values given by the black dashed lines with yellow error bands. The fit parameters and the first excited state masses, $M_1^{(4)}$ and $M_1^{(3)}$, are given in Table VIII. We note that

(i) The estimate of E_1 is slightly larger from the 3-state fits. Again, this is expected since the fits give "effective" E_i that partly incorporate the contributions of all the higher states neglected in the fits.
(ii) The time t_1 when $m_{\rm eff}^{(1)}(t)$ reaches the estimate E_1 is roughly constant, ≈0.7 fm.
(iii) The signal in $m_{\rm eff}^{(1)}(t)$ becomes noisy for $t \gtrsim t_1$, i.e., before confirmation of it having plateaued.
(iv) Estimates of $M_1^{(4)}$ and $M_1^{(3)}$ for the two physical pion mass ensembles (see Table VIII and $M_1^{(4)} - M_1^{(3)}$ plotted in Fig. 21) are consistent with the $N(1710)$ excited state, or a combination of the $N(1440)$ and $N(1710)$ as they overlap within their widths, $\Gamma \approx$ 300 and 100 MeV.

TABLE VIII. Results for M_1 from the four-state empirical Bayesian fit (4s) and the three-state frequentist fit (3s). For ensembles with $a \approx 0.12, 0.15$ fm, a two-state frequentist fit is performed, nevertheless, we keep the label "3s" for brevity. The second column gives the approximate time t_1 at which the $m_{\text{eff}}^{(1)}$ reaches the first excited state energy E_1 given by the four-state fit. The time interval used in the four- (three-) state fits to $C^{\text{2pt}}(t)$ is given in the third (fourth) column. These fit ranges were chosen individually for each case balancing between keeping the maximum number of points with signal in the effective mass plot and the χ^2/d.o.f.

Ensemble ID	t_1/a	$4s$ $[t_{\text{min}}, t_{\text{max}}]$	$3s$ $[t_{\text{min}}, t_{\text{max}}]$	$M_1^{(4)}$ GeV	$M_1^{(3)}$ GeV
a15m310	4	[1, 10]	[1, 10]	2.04(06)	2.22(03)
a12m310	6	[2, 15]	[2, 10]	1.58(09)	2.51(05)
a12m220S	6	[2, 15]	[2, 10]	1.50(08)	2.40(08)
a12m220	6	[2, 15]	[1, 12]	1.63(12)	2.39(02)
a12m220L	7	[2, 15]	[2, 14]	1.69(18)	2.40(03)
a09m310	7	[2, 18]	[2, 18]	2.06(13)	2.09(16)
a09m220	9	[3, 14]	[2, 20]	1.72(09)	2.00(10)
a09m130W	7	[4, 20]	[2, 20]	1.76(09)	1.82(09)
a06m310	12	[7, 30]	[3, 30]	1.65(11)	2.09(14)
a06m310W	8	[4, 25]	[2, 25]	2.05(15)	2.37(15)
a06m220	13	[7, 30]	[3, 30]	1.87(08)	2.10(06)
a06m220W	11	[4, 20]	[2, 25]	1.82(15)	2.21(11)
a06m135	12	[6, 30]	[2, 25]	1.69(11)	1.85(05)

(v) Estimates of E_2 and $m_{\text{eff}}^{(2)}(t)$ from 3-state fits are not reliable.

(vi) In the bottom right panel of Fig. 23, we input $E_1 = E_0 + 2M_\pi$ (solid black line) to study impact on $m_{\text{eff}}^{(n)}(t)$. Estimates of $m_{\text{eff}}^{(1)}(t)$ are not changed but $m_{\text{eff}}^{(2)}(t)$ shows a much more rapid fall. The signal is, however, poor and dies before any conclusion can be reached.

Overall, this analysis highlights the challenge of determining the excited state energies E_i from fits to $C^{\text{2pt}}(t)$ and making an association with physical states.

APPENDIX B: EXTRAPOLATION OF THE NUCLEON MASS M_N TO THE PHYSICAL POINT

Here we revisit the extrapolation of the nucleon mass $M_N(a, M_\pi^2, M_\pi L)$ given in Table VII to the physical point and extend the discussion in the Appendix B in Ref. [19]. We use the following CCFV ansatz:

$$M_N = c_0 + c_1 a + c_2 a^2 + c_3 M_\pi^2 + c_4 M_\pi^3 + c_5 M_\pi^2 e^{-M_\pi L}. \tag{B1}$$

Results and the fit parameters c_i for various truncations of this ansatz are given in Table IX. The AIC score is defined as $\text{AIC} = 2k - 2\log(L) = 2k + \chi^2 + \text{constant}$ where k is the number of parameters and L is the likelihood function. When quoting AIC scores, we drop the irrelevant constant. The CCFV fits F1 and B1 are shown in Fig. 24. Our analysis indicates

(i) The CCFV fits, F1-F4, to the $M_0^{(3)}$ data give slightly smaller continuum M_N than fits to $M_0^{(4)}$ even though $M_0^{(3)} > M_0^{(4)}$ as shown in Fig. 21 (bottom panel) for each of the thirteen ensembles.

(ii) Only F1 ($M_N = 0.939(12)$ GeV) and B1 ($M_N = 0.945(16)$ GeV) fits give estimates consistent with the physical value of $M_N = 939$ GeV. The other fits give ≈25 MeV higher values.

(iii) The F3 and B3 fits, which include the higher order M_π^3 term give a c_4 that is roughly consistent with the χPT prediction $c_4 = 3g_A^2/(32\pi F_\pi^2) = -5.716$. On including a^2 and/or finite volume correction terms in addition to the M_π^3 term, c_4 remains consistent with the χPT prediction for F1, F2, and F4 fits but becomes smaller for B1, B2, and B4.

(iv) The finite volume coefficient, c_5, is not well determined in any of the fits. Without it, fits F1 and B1 have small p-value but give results consistent with

TABLE IX. Summary of CCFV fits to $M_N(a, M_\pi^2, M_\pi L)$ using Eq. (B1). Fits $F1$-$F4$ are to the frequentist (3-state or 2-state) data labeled $M_0^{(3)}$ in the text, and $B1$-$B4$ are to the 4-state empirical Bayesian fit data and labeled $M_0^{(4)}$. To make the interpretation of coefficients c_i defined in Eq. (B1) easier, we give both the functional dependance within square parentheses and the units. The results for $M_0^{(4)}$ are the same as in Ref. [19], except for a small change in $a06m135$ value due to increased statistics. Fits corresponding to the B2 and B4 were given in Table XV in Ref. [19] (labeled B1 and B2 there) and led to $M_N = 0.976(20)$ GeV and 0.972(6) GeV, respectively. The table also gives the AIC score and the p value of the fits.

Fit	M_N GeV	χ^2/d.o.f.	p	AIC	$c_0[1]$ GeV	$c_1[a]$ GeV fm^{-1}	$c_2[a^2]$ GeV fm^{-2}	$c_3[M_\pi^2]$ GeV^{-1}	$c_4[M_\pi^3]$ GeV^{-2}	c_5[FV] GeV^{-1}
F1	0.939(12)	2.187	0.025	27.5	0.878(013)	0.41(25)	−3.2(1.2)	4.24(38)	−6.5(1.0)	···
F2	0.954(14)	1.758	0.091	24.3	0.895(015)	0.11(28)	−1.6(1.4)	4.07(38)	−5.9(1.0)	−6.0(2.6)
F3	0.968(04)	2.686	0.004	32.2	0.904(008)	−0.23(04)	···	4.53(36)	−7.3(9)	···
F4	0.969(04)	1.686	0.096	23.5	0.908(008)	−0.19(04)	···	4.13(38)	−6.0(1.0)	−7.4(2.3)
B1	0.945(16)	1.109	0.353	18.9	0.896(017)	0.27(32)	−2.6(1.5)	3.18(46)	−3.6(1.2)	···
B2	0.968(20)	0.675	0.693	16.7	0.922(021)	−0.16(38)	−0.2(1.9)	2.86(48)	−2.5(1.3)	−10.4(5.1)
B3	0.972(05)	1.318	0.221	19.9	0.921(009)	−0.28(04)	···	3.35(44)	−4.2(1.2)	···
B4	0.970(05)	0.592	0.785	14.7	0.924(009)	−0.20(05)	···	2.86(48)	−2.5(1.3)	−10.7(4.0)

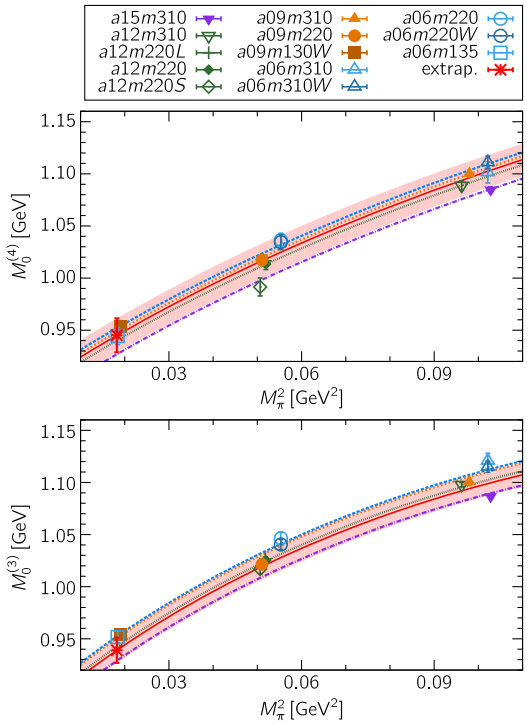

FIG. 24. The result of the chiral-continuum (CC) fit (no finite volume term) to the nucleon mass $M_0^{(4)}$ (B1 fit in Table IX) (top panel) and $M_0^{(3)}$ (F1 fit in Table IX) (bottom panel) is shown by the red line with the error band. The data for B1 and F1 fits given in Table VIII are plotted versus M_π^2 after shifting them in a to $a = 0$ using the CC fits. The CC fit is also shown versus M_π^2 with a set to $a = 0.06$ fm (blue dashed line), 0.09 fm (orange dotted line), 0.12 fm (green dotted line), and 0.15 fm (purple dash-dot line). In a perfect fit, these curves should pass through points with the same color, i.e., with the same lattice spacing a.

the experimental value. Including it, the p-value of F2 and B2 fits improves to an acceptable level, but the coefficients of the lattice spacing dependence, c_1 and c_2, become less well determined. Neglecting the c_2 term (F4 and B4 fits), the c_1 becomes well determined, while the other c_i are essentially unchanged.

In these cases, the ~25 MeV shifts in the M_N from the F1 or B1 fits persist.

Overall, with the current data, we are not able to determine whether $M_0^{(3)}$ or $M_0^{(4)}$ give better estimates of the ground state nucleon mass. Also, we can at best make four-state fits to the two-point function and three-state fits to the three-point functions.

APPENDIX C: DATA FOR THE FORM FACTORS VERSUS Q^2

The unrenormalized values of the form factors G_A, $\tilde{G}_P$, and G_P at the various Q^2 values simulated on the thirteen ensembles and extracted using the three excited-state analysis strategies $\mathcal{S}_{\rm sim}$, $\mathcal{S}_{A4}$, and $\mathcal{S}_{\rm 2pt}$ defined in Sec. II are given in Tables X–XXII. Since the behavior of the data for the four correlation functions varies significantly with Q^2 and the 13 ensembles, we could not develop a simple prescription for making the fits. These $O(1000)$ fits were done individually over a three year period. In addition to the energies E_i and amplitudes A_i, one has to select two additional parameters in each of the fits: (i) the number of points, $t_{\rm skip}$, skipped next to the source and sink at which the ESC are the largest and (ii) the values of source-sink separation τ used in the fit. For these we made the following common choices: (i) $t_{\rm skip}$ was taken to be the same for all values of τ used in a given fit; (ii) in all fits we used data with the largest three values of τ for which the errors were comparable to or smaller than the difference between the central values. In most cases these were the largest three values of τ simulated.

The full covariance matrix was used for all fits to the 3-point functions with the $\mathcal{S}_{\rm 2pt}$ and $\mathcal{S}_{A4}$ strategies and for the 2-point functions. In the simultaneous fits ($\mathcal{S}_{\rm sim}$ strategy), we restricted the covariance matrix to be block diagonal in each correlation function.

A rough estimate of the size of contributions of the $N\pi$ state can be obtained from the difference between results with $\mathcal{S}_{\rm 2pt}$ and $\mathcal{S}_{\rm sim}$ (or $\mathcal{S}_{A4}$) strategies in the following tables. In particular, the smallest Q^2 data for the two

TABLE X. The bare form factors G_A, $\tilde{G}_P$, and G_P versus Q^2 for the 3 strategies $\mathcal{S}_{\rm sim}$, $\mathcal{S}_{A4}$, and $\mathcal{S}_{\rm 2pt}$ on ensemble $a15m310$.

	G_A			$\tilde{G}_P$			G_P		
Q^2[GeV]	$\mathcal{S}_{\rm sim}$	$\mathcal{S}_{A4}$	$\mathcal{S}_{\rm 2pt}$	$\mathcal{S}_{\rm sim}$	$\mathcal{S}_{A4}$	$\mathcal{S}_{\rm 2pt}$	$\mathcal{S}_{\rm sim}$	$\mathcal{S}_{A4}$	$\mathcal{S}_{\rm 2pt}$
0.252(00)	1.007(008)	1.010(009)	0.993(006)	12.53(22)	12.89(23)	11.01(14)	15.12(24)	15.56(23)	13.14(15)
0.483(01)	0.842(007)	0.842(007)	0.822(007)	6.388(126)	6.433(102)	5.827(093)	8.115(143)	8.162(105)	7.386(097)
0.703(02)	0.720(007)	0.720(010)	0.690(008)	3.967(071)	4.046(104)	3.647(072)	5.255(095)	5.357(105)	4.939(081)
0.911(06)	0.648(017)	0.657(020)	0.614(017)	2.890(132)	2.915(148)	2.553(094)	4.080(172)	4.071(160)	3.559(097)
1.102(07)	0.593(011)	0.587(013)	0.561(011)	2.144(082)	2.065(090)	1.978(061)	3.184(133)	3.046(105)	2.856(088)
1.297(09)	0.520(006)	0.524(011)	0.491(013)	1.560(045)	1.613(076)	1.590(078)	2.341(063)	2.418(090)	2.369(117)
1.637(22)	0.450(017)	0.476(025)	0.469(023)	1.018(062)	1.119(087)	1.119(103)	1.662(082)	1.793(118)	1.640(121)
1.803(22)	0.439(029)	0.449(034)	0.452(023)	0.999(106)	1.028(124)	1.050(104)	1.444(133)	1.489(148)	1.290(207)
1.790(29)	0.543(114)	0.458(039)	0.395(056)	1.215(356)	1.002(135)	0.959(204)	1.557(428)	1.121(319)	0.995(972)
1.917(31)	0.428(108)	0.437(024)	0.379(046)	0.911(353)	0.938(085)	1.225(153)	1.455(505)	1.354(166)	1.293(322)

TABLE XI. The bare form factors G_A, $\tilde{G}_P$, and G_P versus Q^2 for the 3 strategies $\mathcal{S}_{\rm sim}$, $\mathcal{S}_{A4}$, and $\mathcal{S}_{\rm 2pt}$ on ensemble $a12m310$.

	G_A			$\tilde{G}_P$			G_P		
Q^2[GeV]	$\mathcal{S}_{\rm sim}$	$\mathcal{S}_{A4}$	$\mathcal{S}_{\rm 2pt}$	$\mathcal{S}_{\rm sim}$	$\mathcal{S}_{A4}$	$\mathcal{S}_{\rm 2pt}$	$\mathcal{S}_{\rm sim}$	$\mathcal{S}_{A4}$	$\mathcal{S}_{\rm 2pt}$
0.176(00)	1.086(011)	1.086(011)	1.050(014)	18.01(29)	17.84(38)	16.51(56)	22.32(36)	22.08(41)	21.15(86)
0.342(01)	0.948(010)	0.937(009)	0.905(013)	9.817(153)	9.501(169)	9.493(281)	12.67(20)	12.27(19)	12.02(33)
0.498(02)	0.844(011)	0.842(012)	0.787(016)	6.505(106)	6.411(155)	5.954(199)	8.635(154)	8.499(206)	8.309(252)
0.646(03)	0.764(013)	0.763(014)	0.686(022)	4.664(087)	4.600(138)	4.124(189)	6.478(133)	6.385(194)	5.863(191)
0.787(04)	0.694(011)	0.691(012)	0.639(016)	3.504(088)	3.454(113)	3.246(123)	4.957(127)	4.891(157)	4.301(162)
0.920(05)	0.649(011)	0.666(013)	0.576(019)	2.882(118)	3.006(076)	2.399(168)	4.015(150)	4.161(106)	3.424(180)
1.178(09)	0.533(010)	0.550(017)	0.506(025)	1.684(068)	1.818(110)	1.651(126)	2.606(074)	2.731(163)	2.433(222)
1.293(10)	0.472(031)	0.463(040)	0.465(025)	1.296(193)	1.295(214)	1.469(150)	2.056(173)	2.048(221)	1.659(259)
1.315(19)	0.462(016)	0.538(047)	0.482(336)	1.175(083)	1.609(253)	1.264(1.241)	2.104(152)	2.446(317)	1.680(546)
1.435(18)	0.471(013)	0.488(032)	0.462(044)	1.224(066)	1.293(138)	1.438(258)	1.908(087)	1.984(223)	0.840(515)

TABLE XII. The bare form factors G_A, $\tilde{G}_P$, and G_P versus Q^2 for the 3 strategies $\mathcal{S}_{\rm sim}$, $\mathcal{S}_{A4}$, and $\mathcal{S}_{\rm 2pt}$ on ensemble $a12m220S$.

	G_A			$\tilde{G}_P$			G_P		
Q^2[GeV]	$\mathcal{S}_{\rm sim}$	$\mathcal{S}_{A4}$	$\mathcal{S}_{\rm 2pt}$	$\mathcal{S}_{\rm sim}$	$\mathcal{S}_{A4}$	$\mathcal{S}_{\rm 2pt}$	$\mathcal{S}_{\rm sim}$	$\mathcal{S}_{A4}$	$\mathcal{S}_{\rm 2pt}$
0.175(01)	1.129(033)	1.123(034)	1.084(020)	19.73(92)	19.75(1.08)	16.14(69)	26.03(1.19)	26.27(1.49)	21.67(96)
0.339(03)	0.918(037)	0.920(033)	0.912(020)	9.517(656)	9.580(552)	8.373(527)	14.44(1.11)	14.83(98)	12.60(91)
0.490(06)	0.814(031)	0.821(044)	0.766(027)	5.271(346)	5.634(304)	5.165(360)	8.344(603)	9.064(487)	8.620(681)
0.636(09)	0.749(120)	0.749(044)	0.705(037)	4.284(877)	4.166(328)	3.744(288)	6.528(1.027)	6.563(449)	6.237(399)
0.773(10)	0.629(039)	0.646(041)	0.640(024)	3.016(409)	3.123(268)	2.743(171)	7.386(2.229)	6.484(705)	5.342(341)
0.909(13)	0.587(069)	0.627(045)	0.593(028)	2.568(343)	2.763(309)	2.276(212)	4.458(804)	4.516(556)	3.919(353)
1.178(23)	0.461(144)	0.514(062)	0.502(041)	1.110(705)	1.689(269)	1.515(176)	2.710(222)	3.422(587)	3.156(390)
1.307(25)	0.467(115)	0.571(059)	0.511(039)	1.116(1.966)	1.810(250)	1.480(193)	2.183(5.142)	2.986(644)	2.890(476)
1.238(33)	0.509(049)	0.551(077)	0.555(068)	1.247(181)	1.605(316)	1.499(288)	2.975(858)	3.966(821)	3.586(682)
1.358(36)	0.415(037)	0.425(135)	0.440(050)	0.771(163)	0.712(764)	0.890(225)	2.597(424)	3.625(1.536)	2.818(614)

physical mass ensembles $a09m130W$ and $a06m135$ in Tables XVII and XXII show ∼5%, ∼45%, and ∼45% differences between the $\mathcal{S}_{\rm 2pt}$ and $\mathcal{S}_{\rm sim}$ values for G_A, $\tilde{G}_P$, and G_P, respectively. A ∼ 5% level of effect in $G_A(Q^2)$ is also consistent with what is observed in the axial charge g_A extracted from the forward matrix element between "3-RD" and "3*" strategies as shown in Table XXXI in Appendix F.

The values of $Q^2 = |\vec{p}|^2 - (E-M)^2$ given in the first column show that for a given gauge coupling β (approximately constant a) and keeping $M_\pi L$ constant, for example, in the three $a \approx 0.09$ fermi ensembles, the values of Q^2 decrease as $M_\pi \to 135$ MeV. This is because $\vec{p} = 2\pi\vec{n}/La$ decreases as L is increased to keep the parameter controlling the finite-volume effects, $M_\pi L$, constant. The same decrease happens if L is increased at

TABLE XIII. The bare form factors G_A, $\tilde{G}_P$, and G_P versus Q^2 for the 3 strategies $\mathcal{S}_{\rm sim}$, $\mathcal{S}_{A4}$, and $\mathcal{S}_{\rm 2pt}$ on ensemble $a12m220$.

	G_A			$\tilde{G}_P$			G_P		
Q^2[GeV]	$\mathcal{S}_{\rm sim}$	$\mathcal{S}_{A4}$	$\mathcal{S}_{\rm 2pt}$	$\mathcal{S}_{\rm sim}$	$\mathcal{S}_{A4}$	$\mathcal{S}_{\rm 2pt}$	$\mathcal{S}_{\rm sim}$	$\mathcal{S}_{A4}$	$\mathcal{S}_{\rm 2pt}$
0.105(00)	1.174(020)	1.169(021)	1.145(017)	28.84(1.16)	28.37(1.27)	24.11(1.40)	38.36(1.42)	37.84(1.55)	32.00(2.09)
0.206(02)	1.033(014)	1.041(017)	1.031(022)	15.55(42)	15.93(52)	14.53(97)	21.95(58)	22.23(66)	20.38(1.43)
0.301(02)	0.954(017)	0.956(017)	0.930(021)	10.75(34)	10.93(34)	9.99(48)	15.17(47)	15.30(49)	13.78(59)
0.391(03)	0.908(017)	0.911(017)	0.900(021)	7.975(219)	8.011(221)	7.498(345)	11.51(34)	11.43(34)	10.44(41)
0.482(04)	0.834(014)	0.836(016)	0.812(021)	6.182(192)	6.168(240)	5.752(262)	9.135(300)	9.236(356)	8.444(356)
0.568(05)	0.784(018)	0.787(021)	0.749(024)	4.988(200)	5.142(246)	4.601(249)	7.746(282)	7.955(344)	6.803(348)
0.732(08)	0.690(015)	0.730(029)	0.671(028)	3.404(152)	3.746(303)	3.246(219)	5.518(262)	6.051(497)	5.145(361)
0.808(10)	0.686(028)	0.705(033)	0.644(031)	3.213(252)	3.323(218)	2.850(237)	5.606(475)	5.833(388)	4.690(377)
0.806(12)	0.676(043)	0.711(035)	0.643(045)	3.147(203)	3.077(357)	2.885(321)	5.421(360)	5.058(541)	4.995(556)
0.884(12)	0.655(023)	0.671(025)	0.622(036)	2.579(184)	2.562(240)	2.693(266)	4.085(261)	4.115(295)	3.753(470)

TABLE XIV. The bare form factors G_A, $\tilde{G}_P$, and G_P versus Q^2 for the 3 strategies $\mathcal{S}_{\rm sim}$, $\mathcal{S}_{A4}$, and $\mathcal{S}_{\rm 2pt}$ on ensemble $a12m220L$.

	G_A			$\tilde{G}_P$			G_P		
Q^2[GeV]	$\mathcal{S}_{\rm sim}$	$\mathcal{S}_{A4}$	$\mathcal{S}_{\rm 2pt}$	$\mathcal{S}_{\rm sim}$	$\mathcal{S}_{A4}$	$\mathcal{S}_{\rm 2pt}$	$\mathcal{S}_{\rm sim}$	$\mathcal{S}_{A4}$	$\mathcal{S}_{\rm 2pt}$
0.067(0)	1.235(20)	1.259(16)	1.199(09)	39.90(1.21)	40.42(1.12)	30.88(2.09)	52.61(1.52)	52.68(1.37)	40.29(3.15)
0.132(0)	1.129(10)	1.150(09)	1.118(08)	24.34(55)	24.51(45)	20.55(1.17)	32.11(63)	32.17(53)	27.08(1.63)
0.195(0)	1.061(09)	1.078(08)	1.052(09)	17.24(36)	17.22(26)	15.09(68)	23.01(42)	23.01(32)	20.17(95)
0.257(1)	0.982(11)	1.008(09)	0.983(13)	12.68(41)	13.01(19)	11.58(44)	17.74(41)	17.98(27)	16.02(68)
0.316(1)	0.944(08)	0.961(09)	0.936(12)	10.34(21)	10.40(18)	9.30(27)	14.34(27)	14.43(22)	12.98(37)
0.374(1)	0.907(10)	0.921(13)	0.890(14)	8.719(155)	8.623(250)	7.765(203)	12.19(24)	12.11(31)	10.99(29)
0.487(2)	0.822(29)	0.839(09)	0.808(14)	6.264(153)	6.239(091)	5.576(124)	9.003(302)	9.046(132)	8.146(154)
0.541(3)	0.782(15)	0.802(12)	0.771(16)	5.503(129)	5.347(173)	4.894(126)	8.083(176)	7.852(241)	7.260(159)
0.541(3)	0.776(15)	0.797(10)	0.770(17)	5.152(168)	5.075(130)	4.883(130)	7.922(237)	7.606(199)	7.429(190)
0.595(3)	0.739(13)	0.766(09)	0.741(16)	4.549(105)	4.477(110)	4.264(120)	6.992(210)	6.920(168)	6.565(145)

TABLE XV. The bare form factors G_A, $\tilde{G}_P$, and G_P versus Q^2 for the 3 strategies $\mathcal{S}_{\rm sim}$, $\mathcal{S}_{A4}$, and $\mathcal{S}_{\rm 2pt}$ on ensemble $a09m310$.

	G_A			$\tilde{G}_P$			G_P		
Q^2[GeV]	$\mathcal{S}_{\rm sim}$	$\mathcal{S}_{A4}$	$\mathcal{S}_{\rm 2pt}$	$\mathcal{S}_{\rm sim}$	$\mathcal{S}_{A4}$	$\mathcal{S}_{\rm 2pt}$	$\mathcal{S}_{\rm sim}$	$\mathcal{S}_{A4}$	$\mathcal{S}_{\rm 2pt}$
0.183(00)	1.043(06)	1.043(06)	1.053(04)	17.38(22)	17.27(20)	14.60(30)	21.90(21)	21.76(18)	18.35(35)
0.356(01)	0.894(06)	0.894(07)	0.907(06)	9.238(099)	9.231(105)	8.316(185)	12.36(14)	12.37(12)	11.24(25)
0.520(04)	0.793(09)	0.794(09)	0.795(12)	6.027(123)	6.047(103)	5.594(178)	8.372(148)	8.399(126)	7.931(253)
0.673(04)	0.714(09)	0.715(09)	0.717(09)	4.325(084)	4.313(082)	4.042(077)	6.225(108)	6.208(103)	5.776(086)
0.819(08)	0.647(07)	0.659(10)	0.652(09)	3.284(067)	3.370(079)	3.115(091)	4.889(103)	4.989(111)	4.620(103)
0.961(13)	0.602(07)	0.609(12)	0.591(13)	2.612(057)	2.710(084)	2.482(079)	3.938(082)	4.059(114)	3.834(106)
1.197(09)	0.531(14)	0.565(25)	0.521(09)	1.906(082)	2.028(121)	1.676(046)	3.116(126)	3.198(114)	2.781(063)
1.323(13)	0.498(10)	0.506(16)	0.489(08)	1.513(076)	1.601(093)	1.455(047)	2.535(120)	2.663(131)	2.455(123)
1.325(17)	0.449(12)	0.529(34)	0.482(24)	1.352(080)	1.687(162)	1.438(104)	2.312(138)	2.783(174)	2.319(131)
1.421(14)	0.481(23)	0.513(30)	0.470(11)	1.430(141)	1.519(146)	1.296(052)	2.435(240)	2.560(197)	2.216(111)

fixed a and M_π to reduce finite-volume effects as is evident from the data on the three ensembles, $a12m220S$, $a12m220$, and $a12m220L$. This is a simple kinematic effect, i.e., the Q^2 for a given $\mathbf{n}$ decreases as the lattice volume is increased. For fixed M_π and $M_\pi L$, the Q^2 remains roughly the same when a is decreased toward the continuum limit as we keep La, the lattice size in physical units (fermi) constant. This can be deduced from the data on the $a12m310$, $a09m310$ and $a06m310$ ensembles. In short, as lattice QCD calculations improve (larger L, $M_\pi \approx 135$ MeV, and $a \to 0$), the Q^2 values (and $Q^2|_{\rm max}$ for fixed $\vec{n}|_{\rm max} = (3,1,0)$ in our case) decrease. Thus, the standard method for calculations of form factors used in this work will increasingly give more precise form factors in the $Q^2 < 0.5$ GeV^2 region. Further algorithmic developments are needed to push calculations with momentum transfer squared up to $Q^2 \sim 5$ GeV^2 to meet the needs of the DUNE experiment.

TABLE XVI. The bare form factors G_A, $\tilde{G}_P$, and G_P versus Q^2 for the 3 strategies $\mathcal{S}_{\rm sim}$, $\mathcal{S}_{A4}$, and $\mathcal{S}_{\rm 2pt}$ on ensemble $a09m220$.

	G_A			$\tilde{G}_P$			G_P		
Q^2[GeV]	$\mathcal{S}_{\rm sim}$	$\mathcal{S}_{A4}$	$\mathcal{S}_{\rm 2pt}$	$\mathcal{S}_{\rm sim}$	$\mathcal{S}_{A4}$	$\mathcal{S}_{\rm 2pt}$	$\mathcal{S}_{\rm sim}$	$\mathcal{S}_{A4}$	$\mathcal{S}_{\rm 2pt}$
0.086(0)	1.185(17)	1.181(17)	1.169(10)	34.73(1.00)	34.12(92)	27.06(88)	47.06(1.16)	46.25(1.03)	36.91(1.17)
0.169(0)	1.063(11)	1.060(11)	1.074(09)	19.29(39)	19.16(38)	17.17(48)	27.19(45)	27.01(45)	23.67(66)
0.248(1)	0.978(10)	0.974(10)	0.986(09)	13.11(25)	13.04(25)	11.99(30)	18.90(31)	18.85(30)	17.25(48)
0.324(1)	0.925(11)	0.922(11)	0.920(11)	9.940(202)	9.784(217)	8.960(227)	14.41(28)	14.19(27)	13.22(33)
0.398(2)	0.862(08)	0.859(09)	0.858(10)	7.665(141)	7.563(146)	7.158(154)	11.59(19)	11.46(19)	10.67(24)
0.470(2)	0.807(09)	0.806(09)	0.802(11)	6.165(119)	6.086(124)	5.736(134)	9.556(168)	9.451(172)	8.847(189)
0.608(4)	0.726(10)	0.725(10)	0.719(12)	4.401(081)	4.379(090)	4.142(101)	7.007(131)	7.020(136)	6.462(159)
0.674(4)	0.687(11)	0.694(11)	0.683(13)	3.807(084)	3.772(088)	3.532(104)	6.187(137)	6.169(135)	5.456(160)
0.671(5)	0.706(09)	0.711(14)	0.690(16)	3.882(070)	3.935(095)	3.538(131)	6.299(162)	6.333(165)	5.616(208)
0.736(5)	0.664(11)	0.677(12)	0.654(13)	3.351(105)	3.362(111)	3.147(102)	5.480(177)	5.473(176)	4.962(178)

TABLE XVII. The bare form factors G_A, $\tilde{G}_P$, and G_P versus Q^2 for the 3 strategies $\mathcal{S}_{\text{sim}}$, $\mathcal{S}_{A4}$, and $\mathcal{S}_{2\text{pt}}$ on ensemble $a09m130W$.

	G_A			$\tilde{G}_P$			G_P		
Q^2[GeV]	$\mathcal{S}_{\text{sim}}$	$\mathcal{S}_{A4}$	$\mathcal{S}_{2\text{pt}}$	$\mathcal{S}_{\text{sim}}$	$\mathcal{S}_{A4}$	$\mathcal{S}_{2\text{pt}}$	$\mathcal{S}_{\text{sim}}$	$\mathcal{S}_{A4}$	$\mathcal{S}_{2\text{pt}}$
0.049(0)	1.284(37)	1.281(35)	1.197(11)	66.90(4.61)	67.10(3.01)	38.95(1.00)	98.55(6.16)	98.65(4.23)	57.55(1.44)
0.097(0)	1.153(19)	1.152(20)	1.141(10)	36.15(1.21)	34.92(94)	25.08(55)	55.27(1.97)	53.17(1.32)	38.23(92)
0.143(0)	1.091(17)	1.092(17)	1.094(10)	24.32(73)	23.94(58)	18.69(42)	36.65(1.08)	36.14(80)	28.41(65)
0.189(1)	1.014(13)	1.022(17)	1.044(10)	17.42(36)	17.56(41)	14.58(32)	26.35(65)	26.32(59)	22.00(50)
0.234(1)	0.971(12)	0.976(13)	0.997(09)	13.80(31)	13.76(28)	11.88(26)	21.34(49)	21.09(38)	18.08(34)
0.277(1)	0.942(13)	0.945(13)	0.957(10)	11.57(29)	11.55(24)	10.00(23)	17.75(37)	17.70(33)	15.51(32)
0.361(2)	0.877(11)	0.867(13)	0.881(12)	8.244(191)	8.044(197)	7.399(168)	12.84(24)	12.85(28)	11.71(26)
0.403(3)	0.839(13)	0.839(13)	0.847(13)	7.165(179)	7.100(180)	6.517(170)	11.25(28)	11.22(26)	10.30(25)
0.404(4)	0.824(18)	0.822(17)	0.827(19)	6.833(225)	6.806(241)	6.315(216)	11.02(41)	10.97(41)	10.21(35)
0.443(4)	0.804(14)	0.800(13)	0.804(15)	6.399(169)	6.150(203)	5.797(148)	10.24(25)	9.999(276)	9.110(269)

TABLE XVIII. The bare form factors G_A, $\tilde{G}_P$, and G_P versus Q^2 for the 3 strategies $\mathcal{S}_{\text{sim}}$, $\mathcal{S}_{A4}$, and $\mathcal{S}_{2\text{pt}}$ on ensemble $a06m310W$. Data for G_P were, by accident, not saved.

	G_A			$\tilde{G}_P$			G_P		
Q^2[GeV]	$\mathcal{S}_{\text{sim}}$	$\mathcal{S}_{A4}$	$\mathcal{S}_{2\text{pt}}$	$\mathcal{S}_{\text{sim}}$	$\mathcal{S}_{A4}$	$\mathcal{S}_{2\text{pt}}$	$\mathcal{S}_{\text{sim}}$	$\mathcal{S}_{A4}$	$\mathcal{S}_{2\text{pt}}$
0.190(1)	1.022(21)	1.010(23)	1.033(17)	16.99(64)	17.19(68)	14.40(49)	⋯	⋯	⋯
0.365(2)	0.868(15)	0.857(18)	0.870(15)	8.793(230)	8.997(256)	7.911(221)	⋯	⋯	⋯
0.528(3)	0.780(22)	0.774(22)	0.770(20)	6.151(188)	6.149(210)	5.048(228)	⋯	⋯	⋯
0.690(5)	0.669(36)	0.696(34)	0.670(25)	3.913(403)	4.303(242)	3.543(257)	⋯	⋯	⋯
0.840(6)	0.599(29)	0.614(26)	0.614(19)	3.080(168)	3.243(205)	2.932(192)	⋯	⋯	⋯

TABLE XIX. The bare form factors G_A, $\tilde{G}_P$, and G_P versus Q^2 for the 3 strategies $\mathcal{S}_{\text{sim}}$, $\mathcal{S}_{A4}$, and $\mathcal{S}_{2\text{pt}}$ on ensemble $a06m310$. Data for G_P were, by accident, not saved.

	G_A			$\tilde{G}_P$			G_P		
Q^2[GeV]	$\mathcal{S}_{\text{sim}}$	$\mathcal{S}_{A4}$	$\mathcal{S}_{2\text{pt}}$	$\mathcal{S}_{\text{sim}}$	$\mathcal{S}_{A4}$	$\mathcal{S}_{2\text{pt}}$	$\mathcal{S}_{\text{sim}}$	$\mathcal{S}_{A4}$	$\mathcal{S}_{2\text{pt}}$
0.189(01)	1.001(15)	1.007(23)	1.020(17)	15.67(72)	16.28(84)	15.11(64)	⋯	⋯	⋯
0.365(03)	0.853(10)	0.856(14)	0.880(17)	8.451(313)	8.635(228)	8.236(291)	⋯	⋯	⋯
0.532(07)	0.743(12)	0.745(17)	0.723(29)	5.441(168)	5.546(188)	4.964(297)	⋯	⋯	⋯
0.683(10)	0.677(12)	0.718(28)	0.663(32)	3.926(125)	4.409(216)	3.967(368)	⋯	⋯	⋯
0.846(12)	0.599(14)	0.618(21)	0.554(42)	2.929(088)	3.120(105)	2.762(240)	⋯	⋯	⋯

TABLE XX. The bare form factors G_A, $\tilde{G}_P$, and G_P versus Q^2 for the 3 strategies $\mathcal{S}_{\text{sim}}$, $\mathcal{S}_{A4}$, and $\mathcal{S}_{2\text{pt}}$ on ensemble $a06m220W$. Data for G_P were, by accident, not saved.

	G_A			$\tilde{G}_P$			G_P		
Q^2[GeV]	$\mathcal{S}_{\text{sim}}$	$\mathcal{S}_{A4}$	$\mathcal{S}_{2\text{pt}}$	$\mathcal{S}_{\text{sim}}$	$\mathcal{S}_{A4}$	$\mathcal{S}_{2\text{pt}}$	$\mathcal{S}_{\text{sim}}$	$\mathcal{S}_{A4}$	$\mathcal{S}_{2\text{pt}}$
0.109(0)	1.161(48)	1.152(37)	1.124(21)	29.89(1.99)	30.67(1.62)	22.81(89)	⋯	⋯	⋯
0.213(1)	1.022(29)	0.999(23)	1.008(20)	15.51(71)	15.35(56)	13.64(40)	⋯	⋯	⋯
0.313(2)	0.909(24)	0.898(25)	0.901(27)	9.762(387)	10.030(490)	8.987(396)	⋯	⋯	⋯
0.412(6)	0.860(34)	0.860(31)	0.801(52)	7.669(431)	7.993(393)	6.817(437)	⋯	⋯	⋯
0.504(6)	0.777(27)	0.774(27)	0.762(35)	5.701(264)	5.694(253)	5.539(305)	⋯	⋯	⋯

TABLE XXI. The bare form factors G_A, $\tilde{G}_P$, and G_P versus Q^2 for the strategies $\mathcal{S}_{\rm sim}$, $\mathcal{S}_{A4}$, and $\mathcal{S}_{\rm 2pt}$ on ensemble $a06m220$.

	G_A			$\tilde{G}_P$			G_P		
Q^2[GeV]	$\mathcal{S}_{\rm sim}$	$\mathcal{S}_{A4}$	$\mathcal{S}_{\rm 2pt}$	$\mathcal{S}_{\rm sim}$	$\mathcal{S}_{A4}$	$\mathcal{S}_{\rm 2pt}$	$\mathcal{S}_{\rm sim}$	$\mathcal{S}_{A4}$	$\mathcal{S}_{\rm 2pt}$
0.110(0)	1.186(36)	1.149(34)	1.124(16)	30.75(1.54)	30.47(1.37)	21.36(66)	43.30(2.01)	42.85(1.66)	29.59(67)
0.216(1)	1.005(15)	0.973(20)	1.007(15)	16.04(47)	15.59(46)	13.08(36)	22.74(66)	22.14(54)	18.43(36)
0.318(2)	0.910(24)	0.862(20)	0.918(18)	10.53(42)	10.08(31)	9.228(312)	14.83(52)	14.93(41)	13.39(32)
0.414(5)	0.823(23)	0.807(22)	0.850(22)	7.449(289)	7.439(259)	6.917(272)	11.14(33)	10.98(35)	10.37(32)
0.509(6)	0.757(18)	0.754(19)	0.777(20)	5.807(188)	5.781(186)	5.295(199)	8.463(317)	8.621(274)	8.081(259)

TABLE XXII. The bare form factors G_A, $\tilde{G}_P$, and G_P versus Q^2 for the 3 strategies $\mathcal{S}_{\rm sim}$, $\mathcal{S}_{A4}$, and $\mathcal{S}_{\rm 2pt}$ on ensemble $a06m135$.

	G_A			$\tilde{G}_P$			G_P		
Q^2[GeV]	$\mathcal{S}_{\rm sim}$	$\mathcal{S}_{A4}$	$\mathcal{S}_{\rm 2pt}$	$\mathcal{S}_{\rm sim}$	$\mathcal{S}_{A4}$	$\mathcal{S}_{\rm 2pt}$	$\mathcal{S}_{\rm sim}$	$\mathcal{S}_{A4}$	$\mathcal{S}_{\rm 2pt}$
0.051(0)	1.201(51)	1.211(56)	1.179(20)	59.23(4.34)	61.92(4.15)	35.54(1.42)	94.52(6.52)	99.18(6.04)	56.03(2.10)
0.102(1)	1.075(33)	1.075(34)	1.109(16)	32.30(1.88)	32.17(1.48)	22.04(64)	54.37(2.91)	54.56(2.25)	37.84(1.41)
0.151(2)	0.966(31)	0.966(34)	1.041(17)	20.25(1.02)	20.52(97)	16.21(55)	36.14(1.68)	36.60(1.55)	28.47(1.20)
0.198(2)	0.940(24)	0.948(25)	1.008(18)	15.71(74)	15.95(57)	13.47(48)	26.73(1.01)	26.96(85)	22.41(73)
0.246(3)	0.876(20)	0.877(22)	0.940(20)	11.82(47)	11.75(41)	10.33(31)	21.32(60)	21.32(66)	18.53(59)
0.294(4)	0.836(17)	0.838(21)	0.876(32)	9.153(297)	9.397(327)	8.750(352)	16.88(49)	17.34(54)	15.85(55)
0.386(6)	0.778(19)	0.782(18)	0.788(37)	6.977(212)	6.977(182)	6.705(320)	12.84(37)	12.83(37)	11.73(44)
0.431(5)	0.755(19)	0.755(18)	0.740(34)	5.883(182)	5.862(188)	5.665(321)	11.17(34)	11.25(35)	10.39(46)
0.432(5)	0.739(22)	0.750(21)	0.753(37)	6.129(219)	6.163(202)	5.909(331)	11.38(41)	11.33(39)	10.79(56)
0.475(6)	0.718(21)	0.736(19)	0.707(28)	5.386(184)	5.369(168)	4.757(193)	9.941(344)	9.931(313)	9.117(407)

APPENDIX D: RESULTS FOR g_A, $\langle r_A^2\rangle$, g_P^*, AND $g_{\pi NN}$

The results for g_A, $\langle r_A^2\rangle$, g_P^*, $g_{\pi NN}F_\pi$, and $\frac{g_{\pi NN}F_\pi}{M_N}$ from the thirteen ensembles are given in Tables XXIII–XXV.

TABLE XXIII. Results for g_A and $\langle r_A^2\rangle$ given by z^2 fits to the axial form factor, $G_A(Q^2)$, obtained with the $\mathcal{S}_{\rm sim}$ strategy. The χ^2/d.o.f. and p-value of the fits are also given.

ID	g_A	$\langle r_A^2\rangle$	χ^2/d.o.f.	p
a15m310	1.211(30)	0.229(11)	1.07	0.38
a12m310	1.209(40)	0.221(17)	0.29	0.94
a12m220L	1.246(43)	0.300(25)	2.39	0.01
a12m220	1.234(46)	0.292(28)	0.87	0.56
a12m220S	1.331(80)	0.331(59)	0.25	0.96
a09m310	1.188(49)	0.250(11)	0.81	0.56
a09m220	1.233(54)	0.297(21)	1.33	0.21
a09m130W	1.272(65)	0.446(72)	1.30	0.22
a06m310	1.158(44)	0.239(18)	0.56	0.74
a06m310W	1.165(48)	0.221(24)	0.59	0.71
a06m220	1.300(59)	0.368(45)	0.69	0.63
a06m220W	1.261(70)	0.311(50)	0.42	0.83
a06m135	1.349(85)	0.74(13)	0.63	0.71

TABLE XXIV. Results for g_P^*, $g_{\pi NN}F_\pi$, and $g_{\pi NN}F_\pi/M_N$ given by the "PD" fits [defined in Eq. (42)] to $\tilde{G}_P$ obtained using $\mathcal{S}_{\rm sim}$ strategy. The χ^2/d.o.f. and p-value of the fits are also given, and F_π and M_N are in units of GeV.

ID	g_P^*	$g_{\pi NN}F_\pi$	$\frac{g_{\pi NN}F_\pi}{M_N}$	χ^2/d.o.f.	p
a15m310	2.16(07)	1.24(05)	1.15(04)	0.92	0.43
a12m310	2.44(09)	1.33(06)	1.22(05)	0.61	0.61
a12m220L	4.02(16)	1.23(05)	1.21(05)	1.34	0.23
a12m220	3.73(18)	1.14(06)	1.13(06)	0.68	0.69
a12m220S	4.71(36)	1.47(13)	1.48(13)	0.46	0.71
a09m310	2.37(10)	1.32(06)	1.20(05)	0.86	0.46
a09m220	3.98(18)	1.21(06)	1.19(06)	1.15	0.33
a09m130W	8.38(46)	1.19(07)	1.25(07)	1.05	0.39
a06m310	2.20(13)	1.28(09)	1.16(07)	0.01	0.99
a06m310W	2.31(16)	1.34(12)	1.20(11)	3.48	0.03
a06m220	4.38(29)	1.48(12)	1.43(12)	0.27	0.77
a06m220W	4.16(38)	1.41(16)	1.37(15)	1.36	0.26
a06m135	8.35(70)	1.16(11)	1.23(11)	1.44	0.23

TABLE XXV. The values of g_P^*, $g_{\pi NN}F_\pi$, and $g_{\pi NN}F_\pi/M_N$ given by z^2 fits to $\mathcal{S}_{\rm sim}$ strategy data for $\tilde{F}_P$ defined in Eq. (41). The χ^2/d.o.f. and p-value of the fits are also given, and F_π and M_N are in units of GeV.

ID	g_P^*	$g_{\pi NN}F_\pi$	$\frac{g_{\pi NN}F_\pi}{M_N}$	χ^2/d.o.f.	p
a15m310	2.22(08)	1.30(06)	1.20(05)	0.46	0.84
a12m310	2.46(09)	1.36(06)	1.25(06)	0.45	0.85
a12m220L	4.06(16)	1.26(06)	1.24(05)	0.92	0.52
a12m220	3.81(20)	1.18(08)	1.16(07)	0.47	0.91
a12m220S	4.62(32)	1.47(12)	1.48(12)	0.79	0.58
a09m310	2.42(10)	1.38(06)	1.25(06)	0.43	0.86
a09m220	4.11(20)	1.28(07)	1.26(07)	0.66	0.76
a09m130W	8.78(58)	1.28(10)	1.34(10)	0.73	0.70
a06m310	2.20(13)	1.29(09)	1.17(07)	0.23	0.95
a06m310W	2.29(11)	1.34(08)	1.20(07)	1.49	0.19
a06m220	4.28(23)	1.45(09)	1.40(09)	0.42	0.84
a06m220W	3.95(26)	1.33(10)	1.29(09)	0.91	0.48
a06m135	8.39(73)	1.18(13)	1.25(13)	0.83	0.55

APPENDIX E: SUMMARY OF CCFV FITS

This appendix presents results after chiral-continuum-finite-volume extrapolation for g_A and $\langle r_A^2\rangle$ in Table XXVI; g_P^* in Tables XXVII and XXVIII; and $g_{\pi NN}$ in Table XXIX. All the data for $G_A(Q^2)$ and $\tilde{G}_P(Q^2)$ used were obtained with the $\mathcal{S}_{\rm sim}$ strategy to remove ESC, and the Q^2 behavior was fit using either the z^2 truncation [$G_A(Q^2)$] or the PD fit ($\tilde{G}_P(Q^2)$) given in Eq. (42). The four parameters, $b_{0,1,2,3}$, define the CCFV ansatz given in Eq. (29). The tables also give the χ^2/d.o.f., the p-value, and the Akaika information criteria (AIC and AICc) [20] scores for the CCFV fit. The definition of AIC is given in Appendix B, and including correction for small sample sizes, AICc is defined as $rmAICc = AIC + (2k^2+2k)/(n-k-1)$ where n is the number of data points and k is the number of parameters.

TABLE XXVI. Summary of the parameters in the 13-point CCFV fit [Eq. (29)] to g_A and $\langle r_A^2\rangle$. The data used are given in Table XXIII. These were obtained by fitting the Q^2 behavior of G_A, obtained with the $\mathcal{S}_{\rm sim}$ strategy, using the z^2 truncation. Details are given in Sec. III A.

	χ^2/d.o.f.	p	AIC	AICc	b_0[1]	$b_1[a]$ fm^{-1}	$b_2[M_\pi^2]$ GeV^{-2}	b_3[FV] GeV^{-2}
g_A (obtained from G_A with $\mathcal{S}_{\rm sim}$ and z^2 fit) extrapolated using the 13-point CCFV fit								
1.296(050)	0.254	0.986	10.3	15.3	1.332(058)	0.002(477)	−1.967(719)	41.370(37.926)
1.277(047)	0.348	0.968	9.5	12.1	1.303(052)	0.284(402)	−1.402(498)	···
1.219(042)	1.037	0.410	15.4	16.6	1.219(042)	0.039(392)	···	···
1.302(032)	0.361	0.971	8.0	9.2	1.326(040)	···	−1.325(486)	···
1.248(027)	0.940	0.500	14.3	15.5	1.248(027)	···	···	−23.153(22.360)
1.223(013)	0.951	0.494	13.4	13.8	1.223(013)	···	···	···
$\langle r_A^2\rangle$ (obtained from G_A with $\mathcal{S}_{\rm sim}$ and z^2 fit) extrapolated using the 13-point CCFV fit								
0.418(033)	1.310	0.225	19.8	24.8	0.457(040)	−0.489(260)	−2.169(449)	34.126(20.944)
0.384(025)	1.445	0.154	20.4	23.1	0.413(029)	−0.168(170)	−1.596(280)	···
0.287(019)	4.267	0.000	50.9	52.1	0.287(019)	−0.332(167)	···	···
0.369(021)	1.403	0.164	19.4	20.6	0.399(025)	···	−1.643(276)	···
0.298(013)	3.241	0.000	39.6	40.8	0.298(013)	···	···	−38.490(9.863)
0.251(006)	4.240	0.000	52.9	53.2	0.251(006)	···	···	···

TABLE XXVII. Summary of parameters values in the 13-point CCFV fit [see Eq. (29)] for obtaining g_P^*. The data used are given in Tables XXIV and XXV. In the top half, the quantity $(Q^{*2}+M_\pi^2)g_P^* = 2m_\mu M_N \tilde{F}_P(Q^{*2})$, with $\tilde{F}_P$ is defined in Eq. (41) and fit using z^2, is extrapolated, while in the bottom half $(Q^{*2}+M_\pi^2)g_P^* = (Q^{*2}+M_\pi^2)(m_\mu/2M_N)\tilde{G}_P(Q^{*2})$ is used. The extrapolated results are then converted to g_P^* by dividing by the physical value of $(Q^{*2}+M_\pi^2)$. Details are given in Sec. IV.

g_P^*	χ^2/d.o.f.	p	AIC	AICc	b_0[1]	$b_1[a]$ fm^{-1}	$b_2[M_\pi^2]$ GeV^{-2}	b_3[FV] GeV^{-2}
g_P^* (obtained from $\tilde{F}_P$ with $\mathcal{S}_{\rm sim}$ and fit using z^2) extrapolated using the 13-point CCFV fit								
9.300(459)	0.897	0.527	16.1	21.1	0.261(015)	−0.117(124)	−0.018(180)	6.359(9.373)
9.213(441)	0.853	0.577	14.5	17.2	0.257(013)	−0.079(110)	0.067(129)	···
9.301(408)	0.800	0.640	12.8	14.0	0.261(011)	−0.066(107)	···	···
8.969(281)	0.822	0.618	13.0	14.2	0.251(010)	···	0.047(126)	···

(Table continued)

TABLE XXVII. *(Continued)*

g_P^*	χ^2/d.o.f.	p	AIC	AICc	$b_0[1]$	$b_1[a]$ fm^{-1}	$b_2[M_\pi^2]$ GeV^{-2}	b_3[FV] GeV^{-2}
g_P^* (obtained from $\tilde{F}_P$ with $\mathcal{S}_{\rm sim}$ and fit using z^2) extrapolated using the 13-point CCFV fit								
8.968(240)	0.815	0.625	13.0	14.2	0.251(007)	⋯	⋯	2.739(5.929)
9.062(124)	0.765	0.687	11.2	11.5	0.254(003)	⋯	⋯	⋯
g_P^* (obtained from $\tilde{G}_P$ with $\mathcal{S}_{\rm sim}$ and PD fit, Eq. (42) extrapolated using the 13-point CCFV fit								
9.248(484)	1.182	0.301	18.6	23.6	0.258(015)	−0.178(135)	0.075(181)	4.550(9.448)
9.167(454)	1.087	0.368	16.9	19.5	0.255(013)	−0.148(119)	0.138(127)	⋯
9.274(443)	1.096	0.360	16.1	17.3	0.260(012)	−0.105(112)	⋯	⋯
8.708(264)	1.129	0.333	16.4	17.6	0.243(009)	⋯	0.086(119)	⋯
8.793(228)	1.159	0.310	16.7	17.9	0.247(006)	⋯	⋯	2.360(5.527)
8.876(123)	1.078	0.374	14.9	15.3	0.249(003)	⋯	⋯	⋯

TABLE XXVIII. Summary of parameters values in the 13-point CCFV fit [Eq. (29)] plus an additional "pole" term $b_4/(Q^{*2}+M_\pi^2)$) for obtaining g_P^*. The data used are given in Tables XXIV and XXV. In the top half, the quantity $g_P^* = (m_\mu/2M_N)\tilde{F}_P(Q^{*2})/(Q^{*2}+M_\pi^2)$, is extrapolated, while in the bottom half $g_P^* = (m_\mu/2M_N)\tilde{G}_P(Q^{*2})$ is used. Details are given in Sec. IV.

g_P^*	χ^2/d.o.f.	p	AIC	AICc	$b_0[1]$	$b_1[a]$ fm^{-1}	$b_2[M_\pi^2]$ GeV^{-2}	b_3[FV] GeV^{-2}	b_4[pole] GeV^2
g_P^* (obtained from $\tilde{F}_P(Q^{*2})$ using $\mathcal{S}_{\rm sim}$ data and fit using z^2) extrapolated using the 13-point CCFV plus pole fit									
8.763(479)	0.978	0.451	17.8	26.4	0.917(944)	−1.327(1.523)	−6.027(6.740)	83.890(129.644)	0.223(035)
8.770(479)	0.916	0.510	16.2	21.2	0.692(878)	−0.655(1.114)	−3.825(5.817)	⋯	0.228(034)
9.019(292)	0.867	0.563	14.7	17.3	0.127(182)	−0.679(1.113)	⋯	⋯	0.249(011)
8.714(469)	0.859	0.572	14.6	17.3	0.631(872)	⋯	−3.935(5.814)	⋯	0.229(034)
8.950(294)	0.900	0.532	15.0	17.7	0.086(226)	⋯	⋯	−18.315(86.479)	0.249(014)
8.969(281)	0.822	0.618	13.0	14.2	0.047(126)	⋯	⋯	⋯	0.250(011)
g_P^* [obtained from $\tilde{G}_P$ with $\mathcal{S}_{\rm sim}$ and "PD" fit, Eq. (42)] extrapolated using the 13-point CCFV plus pole fit									
8.590(418)	1.273	0.252	20.2	28.8	1.075(905)	−2.081(1.715)	−6.246(6.684)	83.651(136.326)	0.214(031)
8.585(418)	1.174	0.307	18.6	23.6	0.813(798)	−1.322(1.186)	−3.821(5.390)	⋯	0.220(030)
8.806(277)	1.107	0.352	17.1	19.7	0.265(195)	−1.376(1.184)	⋯	⋯	0.240(011)
8.468(404)	1.180	0.298	17.8	20.5	0.698(791)	⋯	−4.209(5.378)	⋯	0.220(030)
8.645(279)	1.191	0.291	17.9	20.6	0.219(222)	⋯	⋯	−58.710(82.451)	0.236(013)
8.708(264)	1.129	0.333	16.4	17.6	0.086(119)	⋯	⋯	⋯	0.242(010)

TABLE XXIX. Summary of the 13-point CCFV fit parameters for the extraction of $g_{\pi NN}$ as described in Sec. IV B 2. The data used are given in Tables XXIV and XXV. In the top table, the product $g_{\pi NN}F_\pi = M_N\tilde{F}_P(-M_\pi^2)$ is extrapolated, and the result, in the continuum, is divided by $F_\pi = 92.9$ MeV. In the bottom table, $\tilde{F}_P(-M_\pi^2)$ is extrapolated and the result in the continuum multiplied by M_N/F_π.

$g_{\pi NN}$	χ^2/d.o.f.	p	AIC	AICc	$b_0[1]$	$b_1[a]$ fm^{-1}	$b_2[M_\pi^2]$ GeV^{-2}	b_3[FV] GeV^{-2}
$g_{\pi NN}$ (obtained with $\mathcal{S}_{\rm sim}$ and fit using z^2) extrapolated using the 13-point CCFV fit								
14.491(857)	0.878	0.544	15.9	20.9	1.330(090)	−0.942(752)	0.339(1.093)	55.002(56.824)
14.273(827)	0.884	0.547	14.8	17.5	1.296(083)	−0.637(683)	1.080(779)	⋯
14.713(764)	0.979	0.463	14.8	16.0	1.357(070)	−0.448(669)	⋯	⋯
13.666(511)	0.883	0.556	13.7	14.9	1.243(060)	⋯	0.935(763)	⋯
13.777(435)	0.886	0.553	13.7	14.9	1.270(040)	⋯	⋯	44.246(36.550)
14.225(228)	0.934	0.511	13.2	13.6	1.312(021)	⋯	⋯	⋯
$g_{\pi NN}$ [obtained from $\tilde{G}_P$ with $\mathcal{S}_{\rm sim}$ and PD fit, Eq. (42)] extrapolated using the 13-point CCFV fit								
14.135(852)	1.202	0.288	18.8	23.8	1.283(087)	−1.230(786)	1.098(1.026)	28.874(53.442)
13.975(799)	1.111	0.349	17.1	19.8	1.261(077)	−1.036(699)	1.497(711)	⋯
14.240(788)	1.412	0.159	19.5	20.7	1.313(073)	−0.519(655)	⋯	⋯
12.986(438)	1.209	0.274	17.3	18.5	1.177(051)	⋯	1.127(666)	⋯
13.271(381)	1.349	0.190	18.8	20.0	1.224(035)	⋯	⋯	35.810(31.073)
13.637(210)	1.347	0.184	18.2	18.5	1.257(019)	⋯	⋯	⋯

APPENDIX F: DATA AND FITS FOR THE EXTRACTION OF ISOVECTOR CHARGES $g_{A,S,T}$ FROM FORWARD MATRIX ELEMENTS

This appendix gives the mass gaps of excited state for the 3-RD-$N\pi$ fit in units of the lattice pion mass for each ensemble. The M_1 is fixed to the noninteracting energy of the $N(\boldsymbol{n})+\pi(-\boldsymbol{n})$ state with $\boldsymbol{n}=(1,0,0)$. The M_2 is constrained to be near the first excited state mass given by the two-point correlator by using the narrow prior shown in the last column in Table XXX. The results for the bare isovector charges $g_{A,S,T,V}$ from the forward matrix elements and the p-value of the fit are given in Table XXXI for the three strategies 3-RD, 3*, and 3-RD-$N\pi$.

The parameters of the fits defined in Eq. (48) and the mass gaps for the 3-RD strategy are given in Table XXXII. Summary of the various CCFV fits to the 3-RD data for the renormalized isovector charges $g_{A,S,T}$ are given in Tables XXXIII, XXXIV, and XXXV. The extraction of the final values at the physical point from these data are discussed in the main text.

TABLE XXX. Mass gaps of excited state for the 3-RD-$N\pi$ fit in units of the lattice pion mass for each ensemble. The M_1 is fixed to the noninteracting energy of the $N(\boldsymbol{n})+\pi(-\boldsymbol{n})$ state with $\boldsymbol{n}=(1,0,0)$. The M_2 is constrained to be near the first excited state mass given by the two-point correlator by using the narrow prior shown in the last column. These mass gaps can be compared with the 3-RD fit results given in the Table XXXII.

		M_2-M_0				
ID	M_1-M_0	Axial	Scalar	Tensor	Vector	Prior
a15m310	2.2	3.50(01)	3.52(01)	3.52(03)	3.50(02)	3.52(12)
a12m310	2.0	4.32(11)	4.51(07)	3.78(14)	4.46(08)	4.55(26)
a12m220L	1.7	5.19(30)	6.26(11)	6.01(17)	6.01(08)	6.05(44)
a12m220	2.0	5.93(12)	6.02(08)	5.55(23)	5.88(12)	6.00(44)
a12m220S	2.5	6.09(04)	6.12(03)	5.97(12)	6.10(05)	6.13(36)
a09m310	2.0	2.91(16)	3.24(11)	3.29(08)	3.43(10)	3.15(21)
a09m220	1.8	3.90(66)	4.43(20)	4.49(14)	2.07(07)	4.35(40)
a09m130W	2.1	5.83(39)	7.27(29)	6.48(23)	2.37(05)	5.84(66)
a06m310	2.0	3.01(02)	3.03(02)	3.11(03)	3.05(01)	3.04(11)
a06m310W	2.0	3.95(04)	3.94(03)	3.89(06)	3.95(02)	3.94(21)
a06m220	2.0	4.20(13)	4.40(06)	4.50(11)	4.47(06)	4.49(29)
a06m220W	2.0	4.91(06)	4.96(04)	5.04(10)	4.95(03)	4.98(29)
a06m135	2.2	6.43(07)	6.84(16)	6.93(27)	6.71(08)	6.60(51)

TABLE XXXI. Summary of bare charges g_A, g_S, g_T, and g_V obtained from forward matrix elements along with the p-value of the three fits used to remove ESC: 3-RD (first row), 3* (or 2-state for g_S) (second row), and 3-RD-$N\pi$ (third row) described in the text. The mass gap M_2-M_0 output by the 3-RD-$N\pi$ fits is summarized in Table XXX.

ID	g_A	p	g_S	p	g_T	p	g_V	p
a15m310	1.266(017)	0.780	0.834(018)	0.040	1.133(006)	0.819	1.073(004)	0.528
	1.250(007)	0.591	0.868(028)	0.002	1.121(006)	0.641	1.069(004)	0.000
	1.243(005)	0.607	0.838(019)	0.031	1.132(004)	0.811	1.070(003)	0.394
a12m310	1.256(006)	0.247	0.929(031)	0.180	1.068(009)	0.089	1.055(005)	0.097
	1.283(018)	0.436	1.091(083)	0.007	1.034(020)	0.060	1.061(008)	0.106
	1.241(005)	0.047	0.910(015)	0.215	1.083(005)	0.000	1.053(002)	0.069
a12m220L	1.275(005)	0.175	0.829(025)	0.038	1.090(007)	0.679	1.068(003)	0.053
	1.289(013)	0.410	0.873(042)	0.000	1.069(011)	0.194	1.067(004)	0.165
	1.266(007)	0.005	0.865(016)	0.089	1.092(003)	0.690	1.064(002)	0.035
a12m220	1.253(010)	0.252	0.987(056)	0.561	1.080(011)	0.363	1.063(004)	0.892
	1.265(021)	0.173	1.113(095)	0.401	1.048(018)	0.243	1.071(009)	0.622
	1.239(007)	0.157	0.929(029)	0.445	1.084(006)	0.266	1.061(003)	0.846
a12m220S	1.257(017)	0.715	0.908(213)	0.113	1.103(027)	0.982	1.065(006)	0.775
	1.266(044)	0.631	1.003(260)	0.015	1.065(039)	0.754	1.081(018)	1.000
	1.245(012)	0.627	0.967(097)	0.100	1.110(011)	0.861	1.061(004)	0.713

(Table continued)

TABLE XXXI. *(Continued)*

ID	g_A	p	g_S	p	g_T	p	g_V	p
a09m310	1.275(017)	0.593	1.000(019)	0.305	1.029(004)	0.620	1.047(002)	0.034
	1.238(008)	0.426	1.016(027)	0.170	1.027(007)	0.375	1.036(004)	0.080
	1.212(004)	0.000	1.006(011)	0.291	1.025(004)	0.463	1.067(008)	0.000
a09m220	1.282(016)	0.173	0.987(025)	0.570	1.018(004)	0.809	1.051(002)	0.449
	1.279(013)	0.440	1.056(046)	0.222	1.001(011)	0.634	1.049(004)	0.325
	1.216(006)	0.000	0.989(015)	0.531	1.007(005)	0.379	1.040(007)	0.000
a09m130W	1.320(034)	0.132	1.049(023)	0.542	1.010(006)	0.869	1.054(002)	0.045
	1.271(015)	0.021	1.049(061)	0.069	1.000(011)	0.648	1.052(006)	0.090
	1.231(006)	0.006	1.135(024)	0.068	0.990(007)	0.250	1.011(008)	0.000
a06m310	1.271(057)	0.439	1.172(082)	0.873	0.992(007)	0.217	1.041(005)	0.823
	1.243(027)	0.840	1.239(108)	0.352	0.982(020)	0.738	1.033(010)	0.773
	1.181(008)	0.098	1.121(003)	0.829	0.980(006)	0.058	1.054(011)	0.586
a06m310W	1.264(089)	0.397	1.115(065)	0.288	0.979(016)	0.438	1.036(005)	0.886
	1.216(021)	0.669	1.122(073)	0.501	0.975(016)	0.094	1.035(011)	0.413
	1.208(012)	0.358	1.144(049)	0.280	0.985(009)	0.407	1.036(005)	0.883
a06m220	1.336(065)	0.009	1.183(157)	0.625	0.975(011)	0.668	1.048(005)	0.373
	1.235(018)	0.012	1.109(066)	0.275	0.975(012)	0.372	1.050(007)	0.328
	1.190(011)	0.000	1.026(028)	0.484	0.975(007)	0.664	1.059(007)	0.359
a06m220W	1.383(079)	0.751	0.818(065)	0.539	0.977(012)	0.078	1.039(006)	0.908
	1.257(024)	0.643	0.769(089)	0.770	0.962(022)	0.084	1.039(009)	0.724
	1.212(012)	0.303	0.866(055)	0.454	0.971(008)	0.104	1.037(004)	0.882
a06m135	1.281(061)	0.518	1.025(050)	0.460	0.966(010)	0.277	1.039(005)	0.354
	1.242(021)	0.641	1.108(110)	0.382	0.950(014)	0.208	1.039(006)	0.303
	1.198(010)	0.272	1.154(073)	0.312	0.942(009)	0.072	1.075(007)	0.003

TABLE XXXII. Outputs $r_2 b_{02}$, $r_1 r_2 b_{12}$, and the excited state mass gap $a\Delta M_2$ of the 3-RD fit for the axial (A), scalar (S), tensor (T) and vector (V) charges. The mass gaps in columns 6–8 are in units of M_π for that ensemble. The mass gap $M(N\pi) - M_0 \equiv M_N(\boldsymbol{n}) + M_\pi(-\boldsymbol{n}) - M_0$ with $\boldsymbol{n} = (1,0,0)$ is close to $M_2 - M_0$ for the axial channel and much smaller for the other charges. Note that $M_1 - M_0$ and $M(N\pi) - M_0$ are the same for the four charges.

Ensemble ID	Charge	$r_2 b_{02}$	$r_1 r_2 b_{12}$	$a\Delta M_2$	$\frac{M_1 - M_0}{M_\pi}$	$\frac{M_2 - M_0}{M_\pi}$	$\frac{M(N\pi) - M_0}{M_\pi}$
a15m310	A	−0.063(008)	−0.00(00)	−0.37(11)	3.5(1)	2.0(4)	2.2
a12m310	A	−0.047(008)	−4.0(2.9)	−0.15(10)	4.6(2)	3.7(5)	2.0
a12m220L	A	−0.051(011)	−3.4(1.7)	−0.16(08)	6.1(1)	4.9(6)	1.7
a12m220	A	−0.055(011)	−2.9(3.4)	−0.07(19)	6.0(1)	5.5(1.4)	2.0
a12m220S	A	−0.041(021)	−2.7(4.8)	−0.18(23)	6.1(3)	4.8(1.7)	2.5
a09m310	A	−0.076(013)	0.12(03)	−0.26(06)	3.2(5)	1.3(1)	2.0
a09m220	A	−0.091(012)	0.18(03)	−0.23(04)	4.3(4)	2.0(1)	1.8
a09m130W	A	−0.111(024)	0.20(04)	−0.19(03)	5.8(6)	2.8(3)	2.1
a06m310	A	−0.127(038)	0.12(14)	−0.17(06)	3.0(4)	1.2(3)	2.0
a06m310W	A	−0.070(073)	0.19(29)	−0.27(06)	3.9(5)	1.1(5)	2.0
a06m220	A	−0.191(041)	0.17(15)	−0.19(03)	4.5(2)	1.7(2)	2.0
a06m220W	A	−0.183(058)	0.42(30)	−0.24(03)	5.0(4)	1.5(2)	2.0
a06m135	A	−0.149(052)	0.32(09)	−0.13(03)	6.6(3)	3.3(5)	2.2

(Table continued)

TABLE XXXII. *(Continued)*

Ensemble ID	Charge	$r_2 b_{02}$	$r_1 r_2 b_{12}$	$a\Delta M_2$	$\frac{M_1-M_0}{M_\pi}$	$\frac{M_2-M_0}{M_\pi}$	$\frac{M(N\pi)-M_0}{M_\pi}$
a15m310	S	−0.190(026)	1.13(66)	0.04(08)	3.5(1)	3.7(3)	2.2
a12m310	S	−0.273(045)	−5.6(5.7)	−0.14(16)	4.6(2)	3.8(8)	2.0
a12m220L	S	−0.224(050)	10(13)	0.07(03)	6.1(1)	6.5(2)	1.7
a12m220	S	−0.242(034)	−27(18)	0.04(07)	6.0(1)	6.3(5)	2.0
a12m220S	S	−0.256(086)	18(56)	−0.12(34)	6.1(3)	5.3(2.5)	2.5
a09m310	S	−0.325(007)	−0.04(11)	0.03(09)	3.2(5)	3.4(3)	2.0
a09m220	S	−0.324(009)	0.43(18)	−0.00(00)	4.3(4)	4.3(4)	1.8
a09m130W	S	−0.316(037)	−0.35(55)	0.36(10)	5.8(6)	11.8(1.5)	2.1
a06m310	S	−0.402(026)	−0.9(1.3)	−0.06(08)	3.0(4)	2.4(7)	2.0
a06m310W	S	−0.401(086)	7(17)	−0.02(06)	3.9(5)	3.8(7)	2.0
a06m220	S	−0.482(079)	0.2(1.3)	−0.12(06)	4.5(2)	2.7(9)	2.0
a06m220W	S	−0.424(351)	57(64)	0.09(13)	5.0(4)	6.3(1.8)	2.0
a06m135	S	−0.130(267)	−14.0(8.7)	0.33(10)	6.6(3)	15.0(2.5)	2.2
a15m310	T	0.136(007)	0.10(13)	0.03(07)	3.5(1)	3.6(3)	2.2
a12m310	T	0.172(007)	−1.17(69)	−0.30(05)	4.6(2)	3.0(2)	2.0
a12m220L	T	0.190(020)	−2.06(92)	−0.12(10)	6.1(1)	5.2(7)	1.7
a12m220	T	0.187(008)	−2.3(1.2)	−0.18(08)	6.0(1)	4.7(6)	2.0
a12m220S	T	0.189(033)	−4.4(2.7)	−0.25(12)	6.1(3)	4.3(9)	2.5
a09m310	T	0.200(002)	0.33(07)	0.04(07)	3.2(5)	3.4(1)	2.0
a09m220	T	0.206(003)	0.62(08)	0.07(04)	4.3(4)	5.0(2)	1.8
a09m130W	T	0.214(006)	0.61(07)	0.11(03)	5.8(6)	7.6(3)	2.1
a06m310	T	0.215(029)	1.25(71)	0.11(05)	3.0(4)	4.2(6)	2.0
a06m310W	T	0.227(026)	0.15(43)	−0.05(07)	3.9(5)	3.4(7)	2.0
a06m220	T	0.191(014)	0.17(54)	0.01(04)	4.5(2)	4.7(6)	2.0
a06m220W	T	0.230(028)	−0.15(78)	−0.01(06)	5.0(4)	4.8(9)	2.0
a06m135	T	0.226(016)	1.91(67)	0.12(04)	6.6(3)	9.7(1.1)	2.2
a15m310	V	−0.012(001)	0.16(08)	−0.23(07)	3.5(1)	2.6(3)	2.2
a12m310	V	−0.008(001)	−0.2(2.1)	−0.17(22)	4.6(2)	3.7(1.1)	2.0
a12m220L	V	−0.009(001)	0.04(07)	−0.45(13)	6.1(1)	2.7(9)	1.7
a12m220	V	−0.009(001)	0.06(18)	−0.26(12)	6.0(1)	4.1(9)	2.0
a12m220S	V	−0.009(002)	0.04(18)	−0.36(25)	6.1(3)	3.5(1.9)	2.5
a09m310	V	−0.006(000)	0.36(08)	0.02(01)	3.2(5)	3.3(5)	2.0
a09m220	V	−0.006(000)	0.53(08)	0.01(00)	4.3(4)	4.5(4)	1.8
a09m130W	V	−0.006(000)	0.48(03)	0.01(00)	5.8(6)	6.0(7)	2.1
a06m310	V	−0.005(001)	0.66(28)	0.01(04)	3.0(4)	3.2(7)	2.0
a06m310W	V	−0.006(004)	−0.4(1.3)	0.13(14)	3.9(5)	5.3(1.5)	2.0
a06m220	V	−0.009(002)	1.29(42)	0.07(02)	4.5(2)	5.5(5)	2.0
a06m220W	V	−0.004(001)	0.03(17)	−0.17(16)	5.0(4)	2.6(2.3)	2.0
a06m135	V	−0.003(001)	0.78(16)	0.01(02)	6.6(3)	6.8(6)	2.2

TABLE XXXIII. Summary of CCFV fits to g_A using Eq. (29). We show results for (i) four different trunctions of the four-parameter CCFV ansatz; (ii) fits with three different cuts on the 13 points labeled "13-pt," "11-pt," and "10-pt"; and (iii) fits to data obtained with three different renormalization procedures defined in the text.

g_A	χ^2/d.o.f.	p-value	AIC	AICc	c_0[1]	$c_1[a]$ fm^{-1}	$c_2[M_\pi^2]$ GeV^{-2}	c[FV] GeV^{-2}
				$Z_A g_A^{(\mathrm{bare})}$, 13-pt				
1.281(052)	0.296	0.987	7.3	8.5	1.281(052)	−0.59(45)	⋯	⋯
1.228(029)	0.430	0.943	8.7	9.9	1.232(036)	⋯	−0.22(48)	⋯
1.281(052)	0.325	0.975	9.3	11.9	1.280(054)	−0.60(49)	0.03(52)	⋯
1.285(054)	0.348	0.959	11.1	16.1	1.287(057)	−0.69(55)	−0.08(60)	10.0(28.7)

(Table continued)

TABLE XXXIII. *(Continued)*

g_A	χ^2/d.o.f.	p-value	AIC	AICc	$c_0[1]$	$c_1[a]$ fm^{-1}	$c_2[M_\pi^2]$ GeV^{-2}	c[FV] GeV^{-2}
				$Z_A g_A^{(\mathrm{bare})}$, 11-pt				
1.264(057)	0.214	0.993	5.9	7.4	1.264(057)	−0.45(49)	⋯	⋯
1.222(029)	0.295	0.976	6.7	8.2	1.225(037)	⋯	−0.18(49)	⋯
1.264(057)	0.241	0.983	7.9	11.4	1.263(058)	−0.47(55)	0.04(55)	⋯
1.268(059)	0.265	0.967	9.9	16.5	1.269(062)	−0.54(62)	−0.04(62)	7.7(28.8)
				$Z_A g_A^{(\mathrm{bare})}$, 10-pt				
1.308(072)	0.112	0.999	4.9	6.6	1.308(072)	−0.93(68)	⋯	⋯
1.226(031)	0.313	0.961	6.5	8.2	1.232(040)	⋯	−0.32(60)	⋯
1.316(074)	0.105	0.998	6.7	10.7	1.320(078)	−0.90(68)	−0.25(61)	⋯
1.317(075)	0.115	0.995	8.7	16.7	1.321(078)	−0.88(69)	−0.20(64)	−6.7(31.8)
				$Z_A/Z_V \times g_A^{(\mathrm{bare})}/g_V^{(\mathrm{bare})}$, 13-pt				
1.317(037)	0.334	0.979	7.7	8.9	1.317(037)	−0.62(33)	⋯	⋯
1.252(014)	0.651	0.786	11.2	12.4	1.253(018)	⋯	−0.09(26)	⋯
1.317(038)	0.367	0.961	9.7	12.3	1.317(039)	−0.62(33)	0.00(26)	⋯
1.316(038)	0.403	0.934	11.6	16.6	1.315(040)	−0.61(34)	0.03(31)	−3.0(13.8)
				$Z_A/Z_V \times g_A^{(\mathrm{bare})}/g_V^{(\mathrm{bare})}$, 11-pt				
1.310(039)	0.268	0.983	6.4	7.9	1.310(039)	−0.56(34)	⋯	⋯
1.250(014)	0.555	0.835	9.0	10.5	1.252(018)	⋯	−0.07(26)	⋯
1.309(039)	0.302	0.966	8.4	11.8	1.309(040)	−0.56(35)	0.01(27)	⋯
1.308(040)	0.335	0.939	10.3	17.0	1.307(041)	−0.54(36)	0.05(31)	−3.7(13.8)
				$Z_A/Z_V \times g_A^{(\mathrm{bare})}/g_V^{(\mathrm{bare})}$, 10-pt				
1.320(044)	0.266	0.977	6.1	7.8	1.320(044)	−0.66(39)	⋯	⋯
1.250(014)	0.617	0.764	8.9	10.7	1.251(019)	⋯	−0.05(28)	⋯
1.321(045)	0.302	0.953	8.1	12.1	1.322(047)	−0.66(39)	−0.03(28)	⋯
1.323(045)	0.312	0.931	9.9	17.9	1.322(047)	−0.65(39)	0.03(31)	−7.3(14.8)
				$(Z_A g_A^{(\mathrm{bare})} + Z_A/Z_V \times g_A^{(\mathrm{bare})}/g_V^{(\mathrm{bare})})/2$, 13-pt				
1.292(041)	0.354	0.973	7.9	9.1	1.292(041)	−0.56(36)	⋯	⋯
1.238(019)	0.551	0.869	10.1	11.3	1.241(024)	⋯	−0.18(33)	⋯
1.292(041)	0.389	0.952	9.9	12.6	1.292(042)	−0.56(38)	0.00(35)	⋯
1.294(042)	0.429	0.920	11.9	16.9	1.294(044)	−0.59(41)	−0.03(39)	3.0(17.6)
				$(Z_A g_A^{(\mathrm{bare})} + Z_A/Z_V \times g_A^{(\mathrm{bare})}/g_V^{(\mathrm{bare})})/2$, 11-pt				
1.280(044)	0.268	0.983	6.4	7.9	1.280(044)	−0.46(38)	⋯	⋯
1.235(019)	0.411	0.930	7.7	9.2	1.238(024)	⋯	−0.15(33)	⋯
1.280(044)	0.301	0.966	8.4	11.8	1.280(044)	−0.46(41)	−0.00(36)	⋯
1.281(045)	0.343	0.934	10.4	17.1	1.282(047)	−0.48(44)	−0.02(40)	1.5(17.7)
				$(Z_A g_A^{(\mathrm{bare})} + Z_A/Z_V \times g_A^{(\mathrm{bare})}/g_V^{(\mathrm{bare})})/2$, 10-pt				
1.311(054)	0.183	0.993	5.5	7.2	1.311(054)	−0.77(49)	⋯	⋯
1.237(020)	0.456	0.888	7.6	9.4	1.240(026)	⋯	−0.20(38)	⋯
1.316(056)	0.187	0.988	7.3	11.3	1.319(058)	−0.75(49)	−0.15(39)	⋯
1.317(056)	0.195	0.978	9.2	17.2	1.319(058)	−0.73(50)	−0.10(41)	−7.1(19.3)

TABLE XXXIV. Summary of CCFV fits to g_T using Eq. (29). The rest is same as in Table XXXIII.

g_T	χ^2/d.o.f.	p-value	AIC	AICc	$c_0[1]$	$c_1[a]$ fm^{-1}	$c_2[M_\pi^2]$ GeV^{-2}	c[FV] GeV^{-2}
				$Z_T g_T^{(\mathrm{bare})}$, 13-pt				
0.990(029)	0.281	0.989	7.1	8.3	0.990(029)	0.35(32)	⋯	⋯
1.001(019)	0.270	0.991	7.0	8.2	0.994(024)	⋯	0.38(33)	⋯
0.980(031)	0.222	0.994	8.2	10.9	0.974(033)	0.29(33)	0.32(34)	⋯
0.982(031)	0.145	0.998	9.3	14.3	0.982(034)	0.11(38)	0.02(46)	30.4(31.8)
				$Z_T g_T^{(\mathrm{bare})}$, 11-pt				
0.983(034)	0.329	0.966	7.0	8.5	0.983(034)	0.40(35)	⋯	⋯
0.999(020)	0.303	0.974	6.7	8.2	0.991(026)	⋯	0.45(36)	⋯
0.978(034)	0.266	0.977	8.1	11.6	0.971(036)	0.29(37)	0.35(38)	⋯
0.981(034)	0.176	0.990	9.2	15.9	0.980(037)	0.10(42)	0.05(49)	30.1(31.9)
				$Z_T g_T^{(\mathrm{bare})}$, 10-pt				
1.012(040)	0.156	0.996	5.2	7.0	1.012(040)	0.00(46)	⋯	⋯
1.004(020)	0.117	0.999	4.9	6.6	1.000(026)	⋯	0.22(39)	⋯
1.005(042)	0.133	0.996	6.9	10.9	1.001(045)	−0.02(47)	0.22(40)	⋯
1.000(044)	0.124	0.993	8.7	16.7	0.998(046)	−0.04(47)	0.09(50)	16.3(37.5)
				$Z_T/Z_V \times g_T^{(\mathrm{bare})}/g_V^{(\mathrm{bare})}$, 13-pt				
1.008(025)	0.172	0.999	5.9	7.1	1.008(025)	0.38(28)	⋯	⋯
1.024(015)	0.208	0.997	6.3	7.5	1.018(019)	⋯	0.33(27)	⋯
0.999(026)	0.089	1.000	6.9	9.6	0.994(028)	0.33(28)	0.27(27)	⋯
1.000(026)	0.072	1.000	8.7	13.7	0.997(029)	0.27(31)	0.14(38)	13.1(26.7)
				$Z_T/Z_V \times g_T^{(\mathrm{bare})}/g_V^{(\mathrm{bare})}$, 11-pt				
1.002(029)	0.192	0.995	5.7	7.2	1.002(029)	0.43(30)	⋯	⋯
1.024(016)	0.227	0.991	6.0	7.5	1.017(020)	⋯	0.37(29)	⋯
0.997(029)	0.105	0.999	6.8	10.3	0.992(031)	0.35(32)	0.28(30)	⋯
0.998(029)	0.088	0.999	8.6	15.3	0.995(031)	0.28(35)	0.15(40)	12.8(26.8)
				$Z_T/Z_V \times g_T^{(\mathrm{bare})}/g_V^{(\mathrm{bare})}$, 10-pt				
1.009(033)	0.198	0.991	5.6	7.3	1.009(033)	0.34(38)	⋯	⋯
1.026(016)	0.188	0.993	5.5	7.2	1.020(021)	⋯	0.29(31)	⋯
1.000(035)	0.118	0.997	6.8	10.8	0.995(037)	0.32(39)	0.27(31)	⋯
0.995(037)	0.099	0.997	8.6	16.6	0.992(038)	0.30(39)	0.14(41)	15.3(31.7)
				$(Z_T g_T^{(\mathrm{bare})} + Z_T/Z_V \times g_T^{(\mathrm{bare})}/g_V^{(\mathrm{bare})})/2$, 13-pt				
0.998(020)	0.383	0.963	8.2	9.4	0.998(020)	0.37(22)	⋯	⋯
1.012(013)	0.387	0.962	8.3	9.5	1.005(016)	⋯	0.36(22)	⋯
0.989(021)	0.249	0.991	8.5	11.2	0.984(023)	0.30(23)	0.30(23)	⋯
0.991(021)	0.167	0.997	9.5	14.5	0.990(024)	0.19(25)	0.08(32)	21.8(22.0)
				$(Z_T g_T^{(\mathrm{bare})} + Z_T/Z_V \times g_T^{(\mathrm{bare})}/g_V^{(\mathrm{bare})})/2$, 11-pt				
0.993(023)	0.440	0.914	8.0	9.5	0.993(023)	0.41(24)	⋯	⋯
1.011(013)	0.432	0.919	7.9	9.4	1.004(017)	⋯	0.41(24)	⋯
0.987(023)	0.296	0.967	8.4	11.8	0.982(025)	0.31(25)	0.32(25)	⋯
0.990(024)	0.202	0.985	9.4	16.1	0.988(026)	0.19(28)	0.10(34)	21.5(22.1)
				$(Z_T g_T^{(\mathrm{bare})} + Z_T/Z_V \times g_T^{(\mathrm{bare})}/g_V^{(\mathrm{bare})})/2$, 10-pt				
1.012(028)	0.303	0.965	6.4	8.1	1.012(028)	0.16(32)	⋯	⋯
1.014(013)	0.214	0.989	5.7	7.4	1.009(018)	⋯	0.26(26)	⋯
1.003(029)	0.217	0.982	7.5	11.5	0.999(031)	0.14(32)	0.25(26)	⋯
0.998(030)	0.205	0.975	9.2	17.2	0.996(031)	0.13(32)	0.13(34)	14.7(27.1)

TABLE XXXV. Summary of CCFV fits to g_S using Eq. (29). The rest is same as in Table XXXIII.

g_S	χ^2/d.o.f.	p-value	AIC	AICc	$c_0[1]$	$c_1[a]$ fm^{-1}	$c_2[M_\pi^2]$ GeV^{-2}	c[FV] GeV^{-2}
				$Z_S g_S^{(\mathrm{bare})}$, 13-pt				
0.991(046)	2.073	0.019	26.8	28.0	0.991(046)	−1.37(46)	⋯	⋯
0.876(021)	2.809	0.001	34.9	36.1	0.882(027)	⋯	−0.32(37)	⋯
0.991(046)	2.278	0.012	28.8	31.4	0.990(047)	−1.40(49)	0.07(40)	⋯
1.001(047)	2.435	0.009	29.9	34.9	1.008(050)	−1.61(54)	−0.37(62)	38.7(41.6)
				$Z_S g_S^{(\mathrm{bare})}$, 11-pt				
1.044(051)	1.055	0.393	13.5	15.0	1.044(051)	−1.83(50)	⋯	⋯
0.888(022)	2.317	0.013	24.9	26.4	0.897(028)	⋯	−0.52(38)	⋯
1.045(051)	1.180	0.307	15.4	18.9	1.043(051)	−1.88(56)	0.10(42)	⋯
1.066(053)	1.056	0.389	15.4	22.1	1.076(056)	−2.27(62)	−0.56(63)	60.4(42.2)
				$Z_S g_S^{(\mathrm{bare})}$, 10-pt				
1.077(070)	1.130	0.339	13.0	14.8	1.077(070)	−2.20(75)	⋯	⋯
0.882(022)	2.179	0.026	21.4	23.1	0.886(028)	⋯	−0.21(42)	⋯
1.076(070)	1.288	0.251	15.0	19.0	1.075(071)	−2.23(77)	0.06(43)	⋯
0.993(086)	1.043	0.395	14.3	22.3	1.016(080)	−1.67(84)	−1.23(89)	132.3(79.7)
				$Z_S/Z_V \times g_S^{(\mathrm{bare})}/g_V^{(\mathrm{bare})}$, 13-pt				
0.999(053)	2.456	0.005	31.0	32.2	0.999(053)	−1.43(49)	⋯	⋯
0.832(027)	3.202	0.000	39.2	40.4	0.826(034)	⋯	0.31(47)	⋯
0.988(054)	2.396	0.008	30.0	32.6	0.973(055)	−1.73(52)	0.87(50)	⋯
0.994(054)	2.513	0.007	30.6	35.6	0.990(057)	−1.78(52)	0.21(76)	44.6(38.6)
				$Z_S/Z_V \times g_S^{(\mathrm{bare})}/g_V^{(\mathrm{bare})}$, 11-pt				
1.072(064)	1.696	0.084	19.3	20.8	1.072(064)	−2.03(56)	⋯	⋯
0.846(027)	3.132	0.001	32.2	33.7	0.846(035)	⋯	0.04(48)	⋯
1.083(064)	1.443	0.173	17.5	21.0	1.064(064)	−2.59(63)	1.05(54)	⋯
1.093(064)	1.312	0.240	17.2	23.8	1.090(066)	−2.68(64)	0.16(79)	59.8(38.9)
				$Z_S/Z_V \times g_S^{(\mathrm{bare})}/g_V^{(\mathrm{bare})}$, 10-pt				
1.103(074)	1.825	0.067	18.6	20.3	1.103(074)	−2.35(69)	⋯	⋯
0.837(028)	3.211	0.001	29.7	31.4	0.829(037)	⋯	0.40(54)	⋯
1.097(074)	1.630	0.122	17.4	21.4	1.079(075)	−2.71(72)	1.00(56)	⋯
0.981(089)	0.987	0.432	13.9	21.9	1.001(082)	−1.69(84)	−1.10(1.05)	174.6(74.5)
				$(Z_S g_S^{(\mathrm{bare})} + Z_S/Z_V \times g_S^{(\mathrm{bare})}/g_V^{(\mathrm{bare})})/2$, 13-pt				
1.004(043)	2.563	0.003	32.2	33.4	1.004(043)	−1.46(40)	⋯	⋯
0.867(022)	3.727	0.000	45.0	46.2	0.871(028)	⋯	−0.24(37)	⋯
1.003(043)	2.737	0.002	33.4	36.0	0.996(044)	−1.62(44)	0.37(41)	⋯
1.014(044)	2.883	0.002	33.9	38.9	1.017(047)	−1.81(47)	−0.17(60)	40.7(34.1)
				$(Z_S g_S^{(\mathrm{bare})} + Z_S/Z_V \times g_S^{(\mathrm{bare})}/g_V^{(\mathrm{bare})})/2$, 11-pt				
1.057(048)	1.547	0.125	17.9	19.4	1.057(048)	−1.90(44)	⋯	⋯
0.880(022)	3.408	0.000	34.7	36.2	0.888(028)	⋯	−0.47(38)	⋯
1.064(049)	1.600	0.119	18.8	22.2	1.055(049)	−2.18(51)	0.47(44)	⋯
1.085(050)	1.420	0.192	17.9	24.6	1.090(053)	−2.49(55)	−0.28(62)	58.2(34.4)
				$(Z_S g_S^{(\mathrm{bare})} + Z_S/Z_V \times g_S^{(\mathrm{bare})}/g_V^{(\mathrm{bare})})/2$, 10-pt				
1.095(063)	1.636	0.109	17.1	18.8	1.095(063)	−2.32(64)	⋯	⋯
0.870(023)	3.294	0.001	30.4	32.1	0.871(029)	⋯	−0.04(43)	⋯
1.093(063)	1.755	0.092	18.3	22.3	1.085(064)	−2.47(66)	0.40(45)	⋯
0.983(080)	1.212	0.296	15.3	23.3	1.007(073)	−1.63(76)	−1.32(89)	163.2(72.9)

[1] L. A. Ruso *et al.*, arXiv:2203.09030.
[2] A. S. Kronfeld, D. G. Richards, W. Detmold, R. Gupta, H.-W. Lin, K.-F. Liu, A. S. Meyer, R. Sufian, and S. Syritsyn (USQCD Collaboration), Eur. Phys. J. A **55**, 196 (2019).
[3] A. S. Meyer, A. Walker-Loud, and C. Wilkinson, Annu. Rev. Nucl. Part. Sci. **72**, 205 (2022).
[4] T. Cai *et al.* (MINERνA Collaboration), Nature (London) **614**, 48 (2023).
[5] Y. Aoki *et al.* (Flavour Lattice Averaging Group (FLAG)), Eur. Phys. J. C **82**, 869 (2022).
[6] S. Aoki *et al.* (Flavour Lattice Averaging Group), Eur. Phys. J. C **80**, 113 (2020).
[7] S. Park, R. Gupta, B. Yoon, S. Mondal, T. Bhattacharya, Y.-C. Jang, B. Joó, and F. Winter (Nucleon Matrix Elements (NME) Collaboration), Phys. Rev. D **105**, 054505 (2022).
[8] A. Bazavov *et al.*, Phys. Rev. D **87**, 054505 (2013).
[9] R. Gupta, Y.-C. Jang, H.-W. Lin, B. Yoon, and T. Bhattacharya, Phys. Rev. D **96**, 114503 (2017).
[10] Y.-C. Jang, R. Gupta, B. Yoon, and T. Bhattacharya, Phys. Rev. Lett. **124**, 072002 (2020).
[11] O. Bar, in *Proceedings of the 36th International Symposium on Lattice Field Theory (Lattice 2018) East Lansing, MI, United States, 2018* (Proceedings of Science, 2018), arXiv:1808.08738.
[12] O. Bar, Phys. Rev. D **99**, 054506 (2019).
[13] R. Gupta, Y.-C. Jang, B. Yoon, H.-W. Lin, V. Cirigliano, and T. Bhattacharya, Phys. Rev. D **98**, 034503 (2018).
[14] B. Yoon *et al.*, Phys. Rev. D **93**, 114506 (2016).
[15] G. Parisi, Phys. Rep. **103**, 203 (1984).
[16] G. P. Lepage, in Boulder ASI 1989:97-120 (1989), pp. 97–120, http://alice.cern.ch/format/showfull?sysnb=0117836.
[17] V. Bernard, L. Elouadrhiri, and U.-G. Meissner, J. Phys. G **28**, R1 (2002).
[18] B. Bhattacharya, R. J. Hill, and G. Paz, Phys. Rev. D **84**, 073006 (2011).
[19] Y.-C. Jang, R. Gupta, H.-W. Lin, B. Yoon, and T. Bhattacharya, Phys. Rev. D **101**, 014507 (2020).
[20] H. Akaike, IEEE Trans. Autom. Control **19**, 716 (1974).
[21] T. Bhattacharya, V. Cirigliano, S. Cohen, R. Gupta, A. Joseph, H.-W. Lin, and B. Yoon (PNDME Collaboration), Phys. Rev. D **92**, 094511 (2015).
[22] A. S. Meyer, M. Betancourt, R. Gran, and R. J. Hill, Phys. Rev. D **93**, 113015 (2016).
[23] G. S. Bali, B. Lang, B. U. Musch, and A. Schäfer, Phys. Rev. D **93**, 094515 (2016).
[24] G. S. Bali, L. Barca, S. Collins, M. Gruber, M. Löffler, A. Schäfer, W. Söldner, P. Wein, S. Weishäupl, and T. Wurm (RQCD Collaboration), J. High Energy Phys. 05 (2020) 126.
[25] G. S. Bali, S. Collins, S. Heybrock, M. Löffler, R. Rödl, W. Söldner, and S. Weishäupl, Phys. Rev. D **108**, 034512 (2023).
[26] C. Alexandrou *et al.*, Phys. Rev. D **103**, 034509 (2021).
[27] C. Alexandrou *et al.*, Phys. Rev. D **107**, 054504 (2023).
[28] D. Djukanovic, G. von Hippel, J. Koponen, H. B. Meyer, K. Ottnad, T. Schulz, and H. Wittig, Phys. Rev. D **106**, 074503 (2022).
[29] R. Tsuji, N. Tsukamoto, Y. Aoki, K.-I. Ishikawa, Y. Kuramashi, S. Sasaki, E. Shintani, and T. Yamazaki (PACS Collaboration), Phys. Rev. D **106**, 094505 (2022).
[30] T. Harris, G. von Hippel, P. Junnarkar, H. B. Meyer, K. Ottnad, J. Wilhelm, H. Wittig, and L. Wrang, Phys. Rev. D **100**, 034513 (2019).
[31] C. Alexandrou, S. Bacchio, M. Constantinou, J. Finkenrath, K. Hadjiyiannakou, K. Jansen, G. Koutsou, and A. Aviles-Casco, Phys. Rev. D **102**, 054517 (2020).
[32] C. Alexandrou, S. Bacchio, M. Constantinou, K. Hadjiyiannakou, K. Jansen, and G. Koutsou, Phys. Rev. D **104**, 074503 (2021).
[33] C. Alexandrou, SciPost Phys. Proc. **6**, 006 (2022).
[34] L. Barca, G. Bali, and S. Collins, Phys. Rev. D **107**, L051505 (2023).
[35] R. G. Edwards and B. Joo (SciDAC, LHPC, and UKQCD Collaborations), Nucl. Phys. B, Proc. Suppl. **140**, 832 (2005).